Protein Engineering of a Cytochrome P450 Decarboxylase from *Jeotgalicoccus sp. ATCC 8456:* Structural, Spectroscopic and Kinetic Studies

By

Harry W. Lang

A thesis submitted for the degree of MSc Biochemistry

University of Essex

School of Biological Sciences

Supervisor: Jonathan A. R. Worrall

Date: September 2025

ABSTRACT

The bacterial cytochrome P450 peroxygenase family (CYP152) represents a unique class of heme-containing monooxygenases that utilise hydrogen peroxide as an oxidant, bypassing the canonical P450 redox partner system. Members of this family, particularly $OleT_{JE}$, originally isolated from *Jeotgalicoccus* sp. ATCC 8456, are capable of catalysing oxidative decarboxylation of fatty acids to produce terminal alkenes (olefins). These olefins are of growing industrial interest as potential drop-in biofuels. The key reactive intermediate in this catalytic cycle is the ferryl-oxo porphyrin π-cation radical, commonly referred to as Compound I. However, due to its high reactivity and transient nature, direct characterisation of Compound I remains a significant challenge.

This study focuses on engineering the hydrogen-bonding network surrounding the heme-b prosthetic group in $OleT_{JE}$ through site-directed mutagenesis, with the aim of extending the lifetime of Compound I. A combination of structural, kinetic, and spectroscopic techniques was employed to characterise the impact of these mutations. Fatty acid binding titrations revealed altered binding affinities through dissociation constants, stopped-flow UV/Vis spectrophotometry indicated a significant reduction in Compound I decay rate, and high-resolution macromolecular crystallography provided structural insights into the modified active site architecture.

Future studies will incorporate techniques such as electron paramagnetic resonance (EPR) spectroscopy to investigate changes in the heme iron spin state equilibrium, offering deeper mechanistic insight into how these mutations influence the electronic environment of the active site as well as GC-MS analysis to confirm product formation and fatty acid presence post-purification. Collectively, these results demonstrate the potential of rational protein engineering to stabilise reactive intermediates and enhance enzymatic performance for biotechnological applications.

ACKNOWLEDGEMENTS

This MSc project would not have been possible without the support from colleagues, family and friends alike.

I would like to express my deepest gratitude to my supervisor, Jonathan A.R. Worrall, for their invaluable guidance, patience, and encouragement throughout this research journey. Your insights and support have been instrumental in shaping this work, and I am truly grateful for your mentorship.

I would also like to thank the members of Lab 5.08 for creating a collaborative and inspiring environment. Your feedback, discussions, and camaraderie made the research process both productive and exceptionally enjoyable.

I would like to thank my colleagues and friends Marina, Mike, Lewis, Josh, Mert, and Aidan for their guidance within the lab and throughout writing. I would not be the scientist I am today without their support, advice and encouragement

To my friends, thank you for your unwavering support, understanding, and for reminding me to take breaks and celebrate the small victories along the way.

Finally, I owe my heartfelt appreciation to my family for their love, encouragement, and belief in me. Your support has been the foundation that made this achievement possible.

TABLE OF CONTENTS

Abbreviations

- CYP – Cytochrome P450
- CYP152 – Cytochrome P450 peroxygenase family
- OleTJE – Cytochrome P450 decarboxylase from *Jeotgalicoccus* sp.
- WT – Wild-type
- H_2O_2 – Hydrogen peroxide
- Compound I/Cpd I – Ferryl-oxo porphyrin π-cation radical
- Compound II/Cpd II – Ferryl-hydroxo species
- UV/Vis – Ultraviolet-visible spectroscopy
- SDS-PAGE – Sodium dodecyl sulfate polyacrylamide gel electrophoresis
- EPR – Electron paramagnetic resonance
- GC-MS – Gas chromatography–mass spectrometry
- k_1/k_{obs} – Observed rate constant (s^{-1})
- K_d – Dissociation constant
- SVD – Singular value decomposition

Chapter 1

Introduction

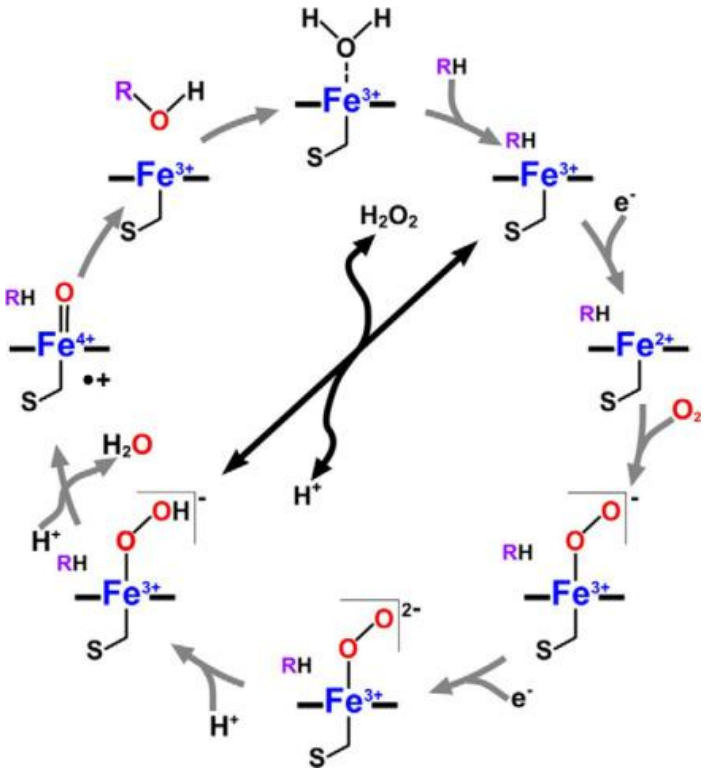

1.1 Introduction

Cytochrome P450 Enzymes

Cytochrome P450 enzymes (CYPs) are heme-containing enzymes that facilitate a broad range of oxidative reactions, including the detoxification of xenobiotics, regulation of metabolism and homeostasis, and the synthesis of steroids (Manikandan & Nagini, 2018). These enzymes play pivotal roles in drug metabolism, steroidogenesis, and even bacterial biosynthesis of antibiotics, such as erythromycin in *Saccharopolyspora erythraea* (Cupp-Vickery & Poulos, 1997). Additionally, aromatase P450 (CYP19A1) in vertebrates' catalyses reactions that convert androgen substrates, like androstenedione, into oestrogens, such as oestrone (Ghosh et al., 2009).

In mammals, P450 enzymes are integral to the metabolism of various substances, particularly within organs such as the liver, intestinal wall, lungs, kidneys, and plasma, where drug metabolism primarily occurs. The liver serves as the central organ for detoxifying xenobiotics by transforming lipid-soluble compounds into more hydrophilic and excretable forms (McDonnell & Dang, 2013). Drug metabolism occurs in two phases: Phase I, involving the modification or formation of functional groups via oxidation, reduction, or hydrolysis, and Phase II, where these metabolites are conjugated to increase water solubility for easier excretion (Gibson & Skett, 2013). Oxidation, the most common Phase I reaction, is typically cytochrome P450-dependent (Gibson & Skett, 2013).

The cytochrome P450 superfamily is a diverse group of heme-b containing monooxygenases that catalyse the reductive cleavage of molecular oxygen by utilising redox partners. These redox partners typically supply two electrons from coenzymes, most commonly NAD(P)H (Munro et al., 2007).

The reaction cycle (Fig. 1.1) begins (top) with the enzyme in its "resting" state, where the heme iron is in a low-spin ferric (Fe^{3+}) state and is coordinated with a cysteine thiolate (S) and a weakly bound water molecule. The substrate (RH) enters the active site, displacing the water molecule and leaving a five-coordinate high-spin ferric iron. This iron is subsequently reduced by an electron provided by redox partners (such as NAD(P)H), converting the iron to a ferrous (Fe^{2+}) state. The enzyme forms a ferric-superoxo complex as dioxygen binds to the ferrous iron. This complex is further reduced by redox partners, resulting in the formation of a ferric-peroxo intermediate. Protonation of this intermediate generates Compound 0, a ferric-hydroperoxo species. Compound 0 is further protonated and dehydrated, resulting in Compound I, a ferryl-oxo porphyrin radical cation. As a radical, Compound I abstracts a hydrogen atom from the substrate, generating a substrate radical. This substrate radical undergoes hydroxylation, producing the enzyme's product (ROH) and returning the enzyme to its original resting state (Belcher et al., 2014).

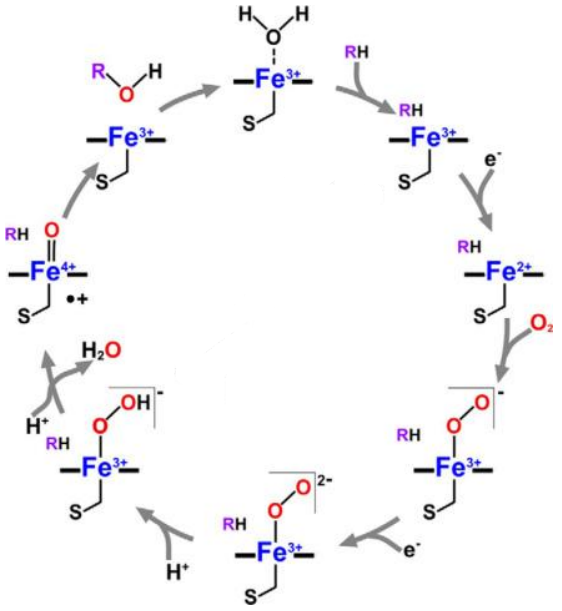

FIGURE 1.1. The catalytic cycle of a cytochrome P450 enzyme. (Figure adopted from Belcher et al., 2014)

The iron(IV)–oxo porphyrin π-cation radical (Compound I) is the key oxidising intermediate in heme enzymes, driving oxygen-transfer and C–H bond activation reactions. Its transient and high reactivity, however, make direct observation and isolation extremely challenging. Synthetic analogues were first reported by Groves and co-workers (1981), and subsequent kinetic and spectroscopic studies confirmed its transient existence in both model complexes

(Pan et al., 2006; Han et al., 2008; Garcia-Bosch et al., 2013) and enzymes (Newcomb et al., 2006). Despite this progress, the transient nature of Compound I prevents it from accumulating under standard turnover conditions, which historically complicated the identification of its role in the catalytic cycle (Sligar, 2010). A range of techniques, including cryogenic trapping, stopped-flow and laser flash photolysis, EPR, resonance Raman, and X-ray absorption spectroscopy, have been employed to capture indirect evidence of its structure and reactivity. Nonetheless, spectral overlap with related ferryl intermediates such as Compound II often obscures definitive assignments. Thorough reviews underscore how protein environment, axial ligation, and porphyrin substitution strongly influence both the stability and reactivity of Compound I, explaining why this species remains one of the most challenging yet crucial intermediates to study in heme enzyme chemistry (Jung, 2011; Hohenberger et al., 2012). However, in 2010, Rittle and Green successfully isolated Compound I by rapidly freezing the enzyme as it interacted with a substrate. Using Mössbauer and electron paramagnetic resonance (EPR) spectroscopy, along with UV/Vis absorption spectroscopy, they were able to confirm the existence of Compound I (Rittle & Green, 2010), representing a significant breakthrough in understanding the P450 enzyme catalytic mechanism.

Most cytochrome P450 enzymes require redox partners, which supply electrons and protons, as well as coenzymes, for catalytic activity. A notable example is the membrane-bound microsomal NADPH-cytochrome P450 reductase (CPR), which contains both FAD and FMN flavins and is essential for transferring electrons to P450 enzymes during catalysis (Wang et al., 1997). Recent research has uncovered evolved P450 enzymes that do not rely on external electron sources but instead utilise hydrogen peroxide as a source of O_2, $2e^-$, and $2H^+$ for catalysis (Lee et al., 2003). CYP152 enzymes are a prime example of this, using hydrogen peroxide to oxidise substrates by directly forming Compound 0, which is then protonated and dehydrated to produce Compound I (as shown in Figure 1.1) (Belcher et al., 2014). This

"peroxide shunt" pathway enables oxidative decarboxylation of fatty acids, leading to the formation of terminal alkenes through the creation of a radical substrate species followed by CO_2 elimination (Munro et al., 2018).

CYP152s

A variant of CYP152s known as $OleT_{JE}$ derived from Jeotgalicoccus sp. (ATCC 8456) has been well-documented to decarboxylate fatty acids ranging from ~C10-C20, to produce terminal alkenes and hydroxy-fatty acids, showing selectivity of the product, it forms (Matthews, S et al., 2017). Rude et al. was able to identify $OleT_{JE}$ as a predominant producer of terminal alkenes; only producing small amounts of hydroxy-fatty acids (Rude, M.A et al., 2011). Results obtained by Rude et al. suggested that CYP152 family will either decarboxylate or hydroxylate yielding α- or β- hydroxy-fatty acids due to structural differences, believing a histidine at position 85 in the substrate binding channel to be significant, although the role of the His85 is still undefined (Rude, M.A et al., 2011). In 2021, Jiang et al. concluded that $OleT_{JE}$ decarboxylation or hydroxylation selectivity can be linked to the presence of a C=C double bond, thus suggesting that short chain fatty acids are more likely to be hydroxylated and long chain fatty acids are more likely to be decarboxylated (Jiang, Y et al., 2021).

Analytical studies using eicosanoic acid as a substrate demonstrate that $OleT_{JE}$ primarily produces nonadecene, with carbon dioxide serving as the coproduct. When hydrogen peroxide is added to a deuterated enzyme–substrate (E–S) complex, a transient iron(IV)-oxo π-cation radical (Compound I) intermediate is formed. A kinetic isotope effect observed during Compound I decay indicates that it abstracts a substrate hydrogen atom, initiating the fatty acid decarboxylation process (Grant et al., 2015). Collectively, these findings suggest that terminal alkene formation proceeds through an initial mechanism resembling the classical P450 monooxygenation pathway, but notably without the oxygen rebound step (Grant et al., 2015).

A study by Makris and coworkers (2016) proposed that alkene formation may arise from the initial abstraction of a hydrogen atom from the Cβ position during conversion of a C_n fatty acid to a C_{n-1} alkene, based on the known mechanism for aliphatic hydroxylation by P450-I (Makris, T.M. et al., 2016)

The terminal alkene or hydroxylated fatty acid producing CYP152s has garnered increased attention over the last decade due to their industrial and medical applications. For example, terminal alkenes can be used in industry to produce plastics, feedstocks, lubricants and even the production of drop-in biofuels (Wang, W et al., 2013), alongside hydroxylated fatty acids being key areas of interest in anti-viral, anti-cancer and other pharmaceutical areas (Jiang, Y et al., 2021). The CYP152 cycle (Fig 1.2) incorporates a double-headed arrow to illustrate the peroxide shunt pathway utilised by peroxygenases such as $OleT_{JE}$. In this pathway, hydrogen peroxide (H_2O_2) bypasses the need for electrons from redox partners and directly converts the substrate-bound 5-coordinate high-spin heme iron to the ferric-hyperoxo species (Compound 0). Compound 0 then undergoes protonation and dehydration to form the ferryl-oxo porphyrin radical cation (Compound I). Compound I abstracts a Cβ hydrogen atom from the substrate, creating a substrate radical and a ferryl-hydroxo species (Compound II). The substrate radical

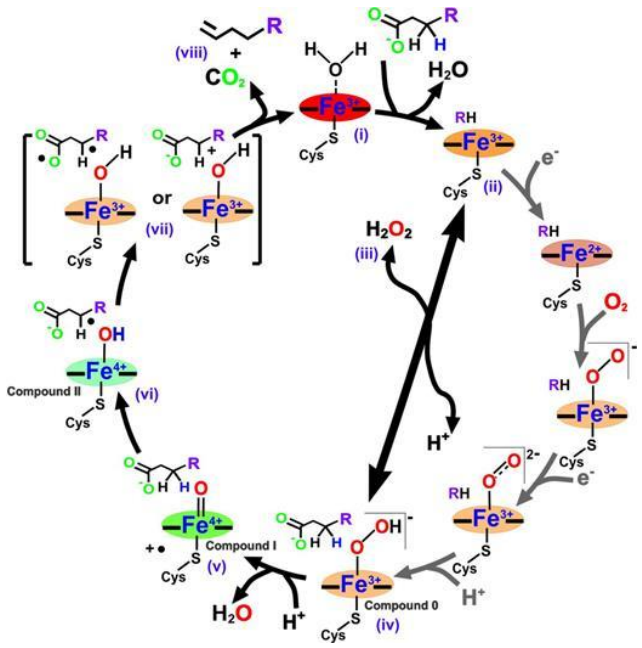

FIGURE 1.2. Proposed catalytic cycle of peroxygenase enzymes incorporating the peroxide shunt pathway and the formation of terminal alkenes within the P450 catalytic cycle. The grey arrows represent the standard P450 catalytic cycle, as depicted in Figure 1.1. (Figure adopted from Munro et al., 2018)

undergoes oxidative decarboxylation with the aid of Compound II, using an electron to generate a substrate diradical or a secondary carbocation. This intermediate ultimately leads to the formation of a terminal alkene through CO_2 elimination, returning the enzyme to its "resting" state (Munro et al., 2018).

Heme spin-states

A key area of interest within the reactive cycle is the change in spin state of the heme iron and how this allows $OleT_{JE}$ to conduct chemistry on its substrates. Ferric iron complexes such as heme-b can exist in different spin states. Upon displacements of the weakly bound water molecule, the heme iron undergoes a low to high spin state transition (Belcher et al., 2014), due to the movement of electrons within the $3d^5$ orbitals of the ferric iron (Larionov, S.V., 2008). This is best described by a crystal field theory approach (Bethe, H. 1929)

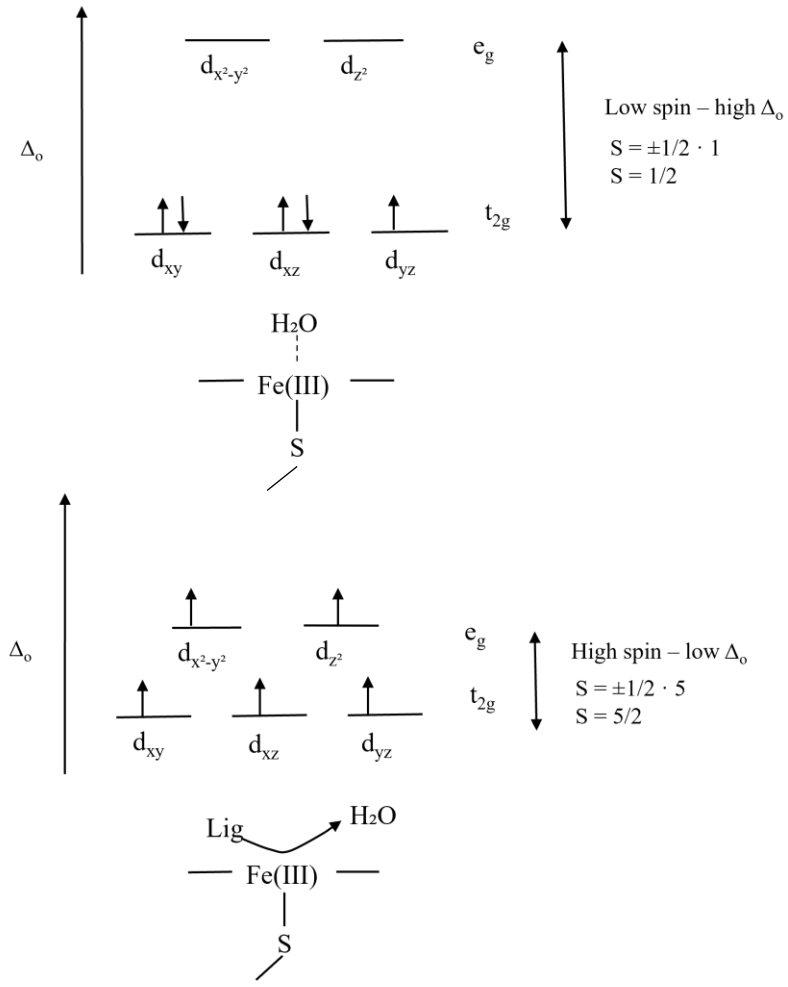

FIGURE 1.3. Octahedral crystal field splitting of the low-spin and high-spin states of the heme iron in cytochrome P450.

Figure 1.3 illustrates two states of the heme iron: (top) the hexacoordinated, low-spin (resting) state. In this configuration, a weakly bound axial water molecule and the axial thiolate ligand generate a large ligand field splitting (Δ_o, the energy gap between the e_g and t_{2g} orbitals). This large splitting causes electrons to preferentially occupy the lower-energy t_{2g} orbitals, resulting in a low-spin configuration. With only one unpaired electron, the spin quantum number is S = 1/2. The high-spin, ligand-bound state (bottom). When the weakly bound water is displaced, often through steric or hydrophobic interactions with a substrate, the heme iron becomes pentacoordinate, reducing the ligand field strength and favouring a high-spin configuration. While the thiolate ligand is believed to play a central role in determining the spin state, the coordinated water may also act as a redox switch, though this possibility remains debated (Green, M.T. 1998).

In its resting state, ferric hexa-coordinated heme-b exists in a low-spin (LS) configuration with S = 1/2 and a characteristic electron absorption at ~417 nm (Pochapsky, T.C. 2020; Munro et al., 2018). When water is displaced by a ligand, the system transitions to a high-spin (HS) state with S = 5/2 and a λmax near 396 nm (Pochapsky, T.C. 2020; Munro et al., 2018). In CYP450s and CYP152s alike, this occurs when a hydrophobic substrate occupies the binding pocket and displaces the coordinated water molecule.

The redox potential of the LS state is typically ~130 mV lower than that of the HS state. Conversion to the more oxidising HS form enables efficient interaction with electron donors such as NAD(P)H reductase, promoting electron transfer within the canonical P450 catalytic cycle. This mechanism is crucial because it minimises wasteful electron uncoupling during catalysis. Without substrate present, the heme remains in the electrochemically negative LS state. Consequently, the system functions as a substrate-controlled redox switch. An important

question is what specific role the heme thiolate ligand plays in governing this redox switching behaviour (Suzuki, H. et al., 2017).

Cysteine axial ligand

A defining spectroscopic feature of cytochromes P450 is the so-called hyper-porphyrin spectrum, which displays a strong absorption band at approximately 450 nm upon reduction of the heme iron and subsequent coordination with carbon monoxide (CO) (Gabel et al., 2022). The designation P450 originates from this diagnostic absorption band. Unlike other heme proteins, which typically employ a neutral histidine ligand, cytochromes P450 are distinguished by coordination of the heme iron to a cysteine thiolate ligand.

Protonation of the axial cysteine heme ligand to a thiol, which disrupts thiolate coordination, converts the enzyme to the P420 form. This form is characterised spectroscopically by a blue shifted reduced absorption band near 420 nm (Gabel et al., 2022) and is generally associated with irreversible catalytic inactivity. Several mechanistic explanations have been proposed for this transition, including protonation of the cysteine thiolate ligand or dissociation of the cysteine from the heme iron (Sun et al., 2013).

Beyond serving as a spectroscopic marker, the cysteine thiolate ligand is central to the catalytic mechanism of cytochrome P450. As in nitric oxide (NO) synthase, cysteine functions as the proximal axial ligand to the heme iron, where it must remain deprotonated (thiolate) throughout the catalytic cycle as the iron alternates among ferric, ferrous, and high-valent ferryl oxidation states (Perera et al., 2003). The resulting thiolate exerts a strong electron-donating effect that lowers the redox potential of the metal centre and stabilises reactive iron–oxo intermediates. This property is essential for enabling the diverse oxidative transformations catalysed by P450 enzymes (Sun et al., 2003; Zhong et al., 2014).

1.2 Aims and Hypotheses

Given the critical role of the axial cysteine residue in enzyme catalysis, a previously published crystal structure was examined to identify potential axial residues capable of forming hydrogen bonds with this cysteine. Disruption of such proton-donating interactions could influence enzyme function in different ways, ranging from stabilising reactive iron–oxo intermediates (Compound I) or alteration to substrate binding affinities and catalysis.

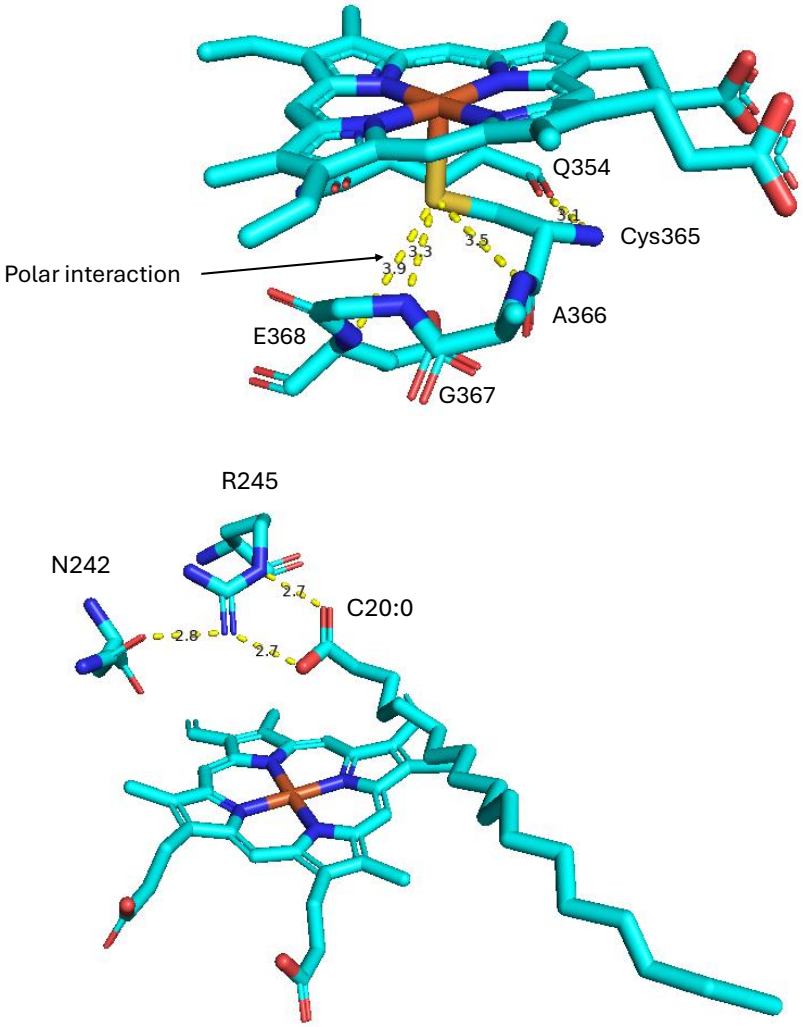

FIGURE 1.4. axial (top) and proximal (bottom) hydrogen bond interactions between respective residues found in wild-type OleT$_{JE}$ from structure 4L40. Possible interactions are represented by yellow dashed lines with those lengths measured in Angstroms.

Residues A366, Q354, G367, and E368, found on the proximal heme side, have been identified to hold hydrogen bond interactions with the axially coordinated cysteine thiolate residue. Given cysteines importance, breaking these hydrogen bond interactions by introducing non-polarity (alanine substitution), or increasing steric bulk (proline substitution) at these positions could have the same meaningful consequences or due to the lack of electron density and protonation around the cysteine ligand, influence the longevity of reactive iron-oxo intermediates.

On the distal side of the heme, residue N242 was identified to hold a hydrogen bond interaction with residue R245 (Fig. 1.4), which interacts with the carboxylate head group of the bound fatty acid substrate to position it close to the heme iron centre for hydrogen abstraction from the C_β position, ultimately leading to alkene formation (Grant et al., 2015). Breaking this interaction is hypothesised to have mechanistically and catalytically drastic consequences as substrate positioning could collapse as a result, potentially making the enzyme inactive.

This study aims to create the $OleT_{JE}$ variants N242A, A366P, Q354A, G367P, and E368P at the identified residue position (Fig. 1.4) to evaluate their effects using spectroscopic, thermodynamic, kinetic, and structural approaches. Through this multidisciplinary analysis, the work seeks to clarify the contribution of the axial cysteine environment to catalytic activity, enzyme stability, as well as proximal and distal residue importance in substrate positioning and catalysis. This study aims to provide deeper insight into the mechanistic important of these residues and informing strategies for future biocatalytic applications.

Chapter 2

Microbiological, Protein Expression, and Purification of $OleT_{JE}$ wild-type and Variants

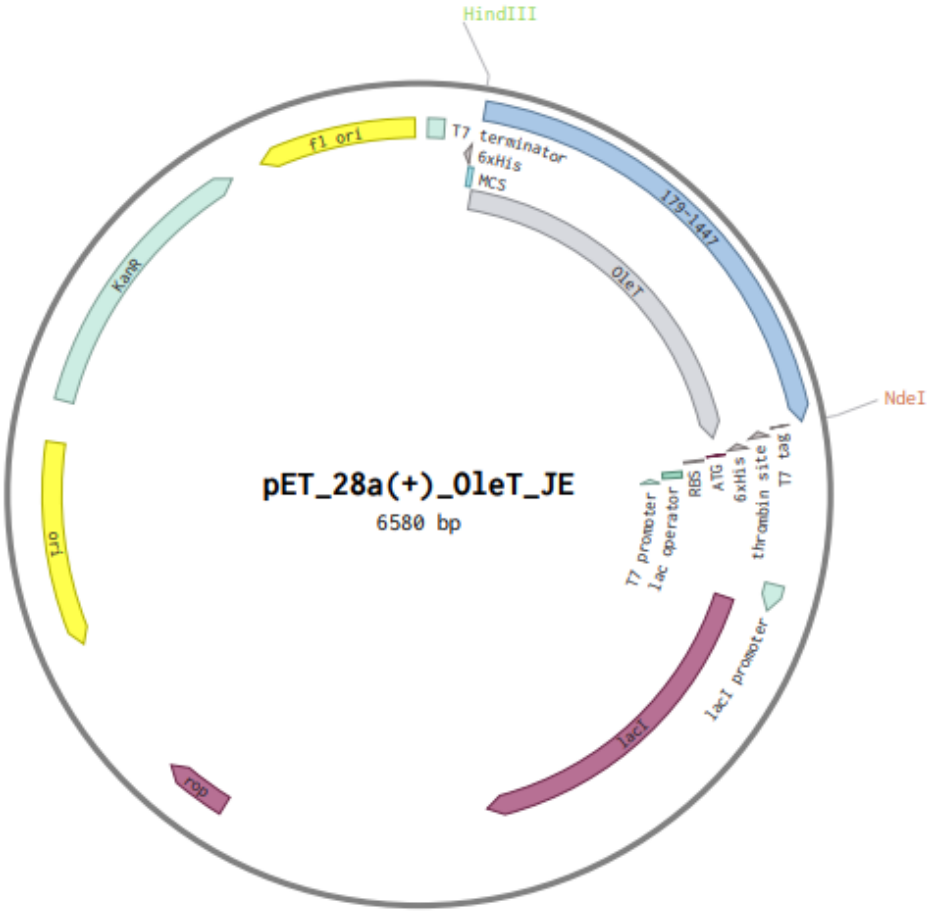

2.1 Introduction

This chapter details the methodologies employed for molecular biology work, recombinant bacterial protein over-expression, and purification, with a specific focus on the rationally designed $OleT_{JE}$ variants N242A, Q354A, A366P, G376P, and E368P. These variants were introduced based on insights gained from the wild-type structure, as discussed in the Introduction chapter. Variants Q354, A366P, G367P, and E368P were designed with the intent of disrupting hydrogen bond interactions to the proximal thiolate ligand, Cys365, with the aim of probing their role in stabilising ferryl heme intermediates. The N242A variant was designed after examination of the active site where Arg245, a residue implicated in substrate positioning, forms a hydrogen bond with the side chain O of the Asn242 in the substrate bound state. Disruption of this hydrogen bond could have meaningful mechanistic, catalytic and structural effects. The experimental work described here includes the design and validation of primers for site-directed mutagenesis, the over-expression and purification of variant proteins, and the analytical techniques used to confirm successful DNA amplification and protein production. Verification methods such as agarose gel electrophoresis and SDS-PAGE are presented alongside detailed protocols for each stage of protein expression and purification. Where appropriate, illustrative figures are provided to depict the experimental setup, equipment, and workflow, ensuring clarity in the methodological approach.

2.2 Experimental Procedure

Primer design for creation of site-directed variants of $OleT_{JE}$

The provided expression construct used in this study is a pET-28a(+) plasmid (Novogene), a T7-based *Escherichia coli* expression vector. This plasmid contains a T7 promoter upstream of the multiple cloning site (MCS), which enables strong transcription by T7 RNA polymerase in suitable *E. coli* host strains (e.g., C43(DE3)). Transcription is further regulated by the lac operator and the lacI gene, which ensure tight gene repression until induction using the synthetic inducer isopropyl beta-D-thiogalactopyranoside. A ribosome binding site (RBS) downstream of the promoter facilitates efficient translation initiation. The MCS enables directional cloning with multiple restriction sites, flanked by sequences encoding affinity and detection tags. In this study, cloning via NdeI and HindIII restriction sites positioned the $OleT_{JE}$ gene in-frame with an N-terminal His_6-tag followed by a thrombin cleavage site, allowing subsequent removal of the affinity tag if required. The plasmid also contains a ColE1 origin of replication (ORI) for maintenance in E. coli, the ROP gene for copy-number regulation, and a kanamycin resistance cassette for selection.

The following site-directed mismatches to create the, N242A, Q354A, A366P, G367P and E368P $OleT_{JE}$ variants were designed and constructed using Benchling software (Benchling, 2025). The design strategy positioned the intended mismatch at the centre of each primer to promote stable hybridisation and ensure balanced thermodynamic stability on both sides of the mismatch, thereby enhancing PCR efficiency. To avoid potential complications arising from primer–primer interactions, non-overlapping primer pairs were designed, with the intended mismatch encoded on the forward primer in each case. All primers were synthesised on the 0.025 μmol scale by Sigma-Aldrich and resuspended in sterile Milli-Q water to a final concentration of 100 μM before use.

Q5 PCR

The choice of Q5 High-Fidelity DNA Polymerase (New England Biolabs) over other polymerases was made due to its combination of ultra-high fidelity (error rate 280-fold lower than Taq polymerase), and suitability for complex cloning and mutagenesis workflows (3'->5' exonuclease for strong proofreading). All PCR reactions were carried out using a Phusion Pfu master mix (New England Biolabs) containing $MgCl_2$, dNTPs, and Phusion polymerase. In a 250 µL PCR tube, 23.5 µL of sterile Milli-Q water, 25 µL of Phusion Pfu master mix, 0.5 µL of plasmid DNA (i.e. from a stock of 100 ng/µL pET-28a($OleT_{JE}$)), and 0.5 µL of the respective forward and reverse primers were mixed to a final volume of 50 µL per reaction. PCR amplification was performed using a T100 thermocycler (Bio-Rad) under the following conditions: an initial denaturation at 98 °C for 30 seconds, followed by 30 cycles of denaturation at 98 °C, annealing at a temperature between 65–75 °C, and extension at 72 °C. Following completion of the cycle, reactions were held at 4 °C. Immediately after the PCR, 1 µL of the restriction enzyme DpnI (Thermo Fisher Scientific) was added to the PCR reaction tubes and incubated at 37 °C for 2 hours.

Agarose gel electrophoresis and DNA purification

A 1% (w/v) agarose gel was prepared (200 mL 10 x TBE + 2 g agarose) with 10 µL of SafeView DNA stain added to the solution following heating. Additionally, the running buffer contained SafeView stain for maximum visibility (5 µL per 100 mL of of TBE running buffer). 10 µL of 6x TriTrack DNA loading dye (Thermo scientific) was added to the PCR tubes, before loading the samples into wells in the gel (30 µL each). 5 µL of a 1 kb DNA ladder (Thermo Scientific) was added to the first well to assist with determining PCR product size. Electrophoresis was conducted at 100–200 V for 45–60 minutes followed by imaging under UV light. Bands of interest (~6.6 kb) were excised, and the DNA was purified using a gel extraction and PCR cleanup protocol (Macherey-Nagel NucleoSpin Gel & PCR Cleanup Kit).

Ligation and Transformation of purified PCR products

Post-cleanup, linearised DNA was treated with a ligation-kinase (lig-kin) master mix containing T4 polynucleotide kinase (PNK), 10x T4 PNK buffer, T4 DNA ligase, and 10x T4 ligase buffer to allow for simultaneous phosphorylation and ligation. 8 µL of the master mix was added per reaction and then incubated for 3 hours at 18 °C. The ligated plasmid concentration and purity were verified using a Nanodrop spectrophotometer (Thermo Scientific), targeting a concentration between 80–100 ng/µl. 10 µL of each ligation product were then transformed into chemically competent E. coli TOP10 cells (Invitrogen) via a standard heat shock protocol. Following heat shock, 950 µL of LB broth (Melford Chemicals) consisting of 10 g/L peptone, 5 g/L yeast extract, 5 g/L NaCl) was added to the cells, which were then incubated for 1 hour at 37 °C with shaking at 180 RPM for cell recovery. Cells were spread onto 1% (w/v) agar, 50 µg/mL kanamycin (200 mL of LB-agar and 100 µL of 100 mg/mL kanamycin) plates and incubated overnight at 37 °C.

DNA Sequencing

Colonies from the kanamycin plates were inoculated into 10 mL LB broth supplemented with 50 µg/mL kanamycin and cultured overnight at 37 °C. Cells were pelleted, and plasmids isolated using a Macherey-Nagel NucleoSpin miniprep kit. The presence of the desired mismatches was corroborated by DNA Sanger sequencing (Eurofins) using T7 forward and T7 reverse sequencing primers and the resulting sequencing data was inputted into to pBlast for alignments with the wild-type (WT) $OleT_{JE}$ sequence. Once the intended mutations were confirmed, purified plasmids were subsequently transformed into E. coli C43 (DE3) cells (Invitrogen). Following heat shock, cells were recovered in LB medium (as previously), centrifuged to pellet the cells and remove media (~800 µL) to concentrate, and re-suspended before plating on 1% (w/v) LB-kanamycin agar. Cells from the plates were inoculated into 10 ml LB-kanamycin overnight pre-cultures (as previously) for use in over-expression.

Glycerol stock preparation

Glycerol stocks of the WT $OleT_{JE}$ and all variant clones were prepared to negate the need for fresh transformations before each over-expression and purification. The glycerol stocks have an extensive 'shelf life' before they begin to show any growth or over-expression inefficiencies, so they were employed. 1 ml of cells from overnight pre-cultures were thoroughly mixed with 1 mL autoclaved 50% glycerol (Fisher) and frozen at -80 °C in 2 ml Eppendorf tubes for future inoculations.

Overexpression and harvesting

For overexpression, between eight and twelve 2 L flasks containing 1 L of 2xYT media (31 g/L) (Melford Chemicals) were prepared and autoclaved. Glycerol stocks of C43 (DE3) cells containing the desired recombinant plasmid (WT or variants) were used to inoculate 10 mL LB-kanamycin overnight pre-cultures. These starter cultures were used to inoculate the 2 L expression flasks. Media was supplemented with additives to promote protein over-expression incorporating a b-type heme, including 32 mg/ml aminolevulinic acid hydrochloride (total volume added per flask, 2 ml) (Biosynth), 100 mM iron (III) citrate (1 ml) (Sigma), and 50 μg/ml kanamycin (500 μl of 100 mg/ml stock) (Fisher Scientific). Cultures were incubated at 37 °C with shaking at 180 RPM until the OD_{600} reached 0.8–1.0. Induction of the $OleT_{JE}$ protein was through the addition of isopropyl beta-D-thiogalactopyranoside (IPTG; Melford Chemicals) (500 μl of 0.5 M) to a final concentration of 250 μM. Following IPTG addition, the cultures were incubated overnight at 25 °C with shaking at 180 RPM. This was followed by harvesting if cells by centrifugation at 10,000 g for 20 minutes at 4 °C.

Protein Purification

The resulting cell pellets were generally red in colour and resuspended in ~5 ml of buffer A (750 mM NaCl (Fisher), 50 mM Tris/HCl (Fisher), 20 mM imidazole (ACROS Organics), pH 7.5) and lysed using a high-pressure homogeniser (Emulsiflex-C5, Avestin. Inc). Cell debris and membranes were removed via centrifugation at 22,000 g for 45 minutes at 4 °C. The clarified supernatant containing soluble protein was loaded onto a 5 mL volume Ni-NTA affinity column (Cytiva) pre-equilibrated with buffer A. As the target protein was N-terminally His6-tagged, it bound to the resin while unbound proteins were washed away using 5–10 column volumes (CV) of buffer A. The bound protein was eluted using a linear 45-minute imidazole gradient (0–500 mM) at 2 ml/min over 18 CV on an AKTA system using buffer B (buffer A with 500 mM imidazole, pH 7.5). Only red-coloured fractions, indicative of heme incorporation, were collected for centrifugal concentration (Vivaspin 10 kKDda cut-off) and further purification. For structural studies, the His6-tag was cleaved by adding 1 KU of bovine thrombin (Merck) and incubating the sample overnight at 16 °C with rocking. The sample was then centrifuged to remove aggregates and passed through a second Ni-NTA column to remove cleaved His6-tag and uncleaved protein. For kinetic experiments, this cleavage step was omitted. Final polishing was performed using size exclusion chromatography on a prepacked HiPrep 16/600 Superdex 200 prep grade column (Cytiva). The column was equilibrated, and 2 ml of concentrated protein was loaded in buffer C (750 mM NaCl, 100 mM sodium phosphate monobasic and dibasic, pH 7.5). The major elution peak at ~ 75 ml is consistent with monomeric species with fractions of this peak being assessed for purity by SDS-PAGE.

Preparation and running of SDS-PAGE

Proteins were resolved on 12.5% Tris–glycine SDS–PAGE gels. This acrylamide concentration was chosen to optimize separation in the ~40–70 kDa range, which includes the target protein (~50.4 kDa). For the resolving gel, 4.2 mL of 30% Acrylamide/Bis solution (29:1), 2.5 mL of

1.5 M Tris-HCl pH 8.8, 100 µL of 10% SDS, 3.1 mL of H 2O, 100 µL of 10% ammonium persulfate (APS), and 4 µL of N,N,N',N'-tetramethylethylenediamine (TEMED) were combined and pipetted into glass moulds. Once settled, a layer 100% butanol were pipetted onto the gel to level out the gel and allow for bands to run smoothly. For the stacking gel, 0.67 mL of 30% Acrylamide/Bis solution (29:1), 1.25 mL of 0.5 M Tris-HCl pH 6.8, 50 µL of 10% SDS, 3.05 mL of H_2O, 50 µL of 10% APS, and 5 µL of TEMED were combined and pipetted on top of the resolving gel once set and after removing the butanol. Combs were added into the stacking gel before it set to create the wells. Once set, the gels were loaded into the SDS-PAGE running apparatus (Bio-Rad) and the appropriate volume (dependent on number of gels being run) of 1x running buffer (25 mM Tris/HCl, 192 mM Glycine, 0.10% w/v SDS, 1 L H_2O, pH 8.3) was added into the gel holder. 10 µL of protein samples that had been treated with 10 µL of 2x 'cracking buffer' (125 mM Tris/HCl, 4% w/v SDS, 20% v/v glycerol, 0.02% w/v bromophenol blue, 100 mM DTT, pH 6.8) and heated at 90 °C for 15 minutes were loaded to each well of the gel. For protein size determination (~50.4 kDa), 5 µL of 10x TriTrack protein ladder (Thermo Scientific) was added to the first well. Once samples and ladder were loaded, the gel was run at 100 V for 45 minutes. Once the gel had finished running, it was removed from the glass plates and stained with an ample volume of Coomassie brilliant blue R-250 staining solution (0.1% w/v or 1 g of Coomassie Brilliant Blue R-250, 40% w/v or 400 mL of Methanol, 10% v/v or 100 mL of Glacial acetic acid, 500 mL of H_2O) and microwaved for 1 minute and left to stain for 1 hour with rocking. Finally, the gel was removed from the stain and microwaved for 1 minute in water for destaining before visualising on an A4 LED light box.

2.3 Results

Primer design, PCR and DNA sequencing

Figure 1 shows Benchling design of the pET28a(+) $OleT_{JE}$ construct, with the salient components illustrated and described in the figure legends.

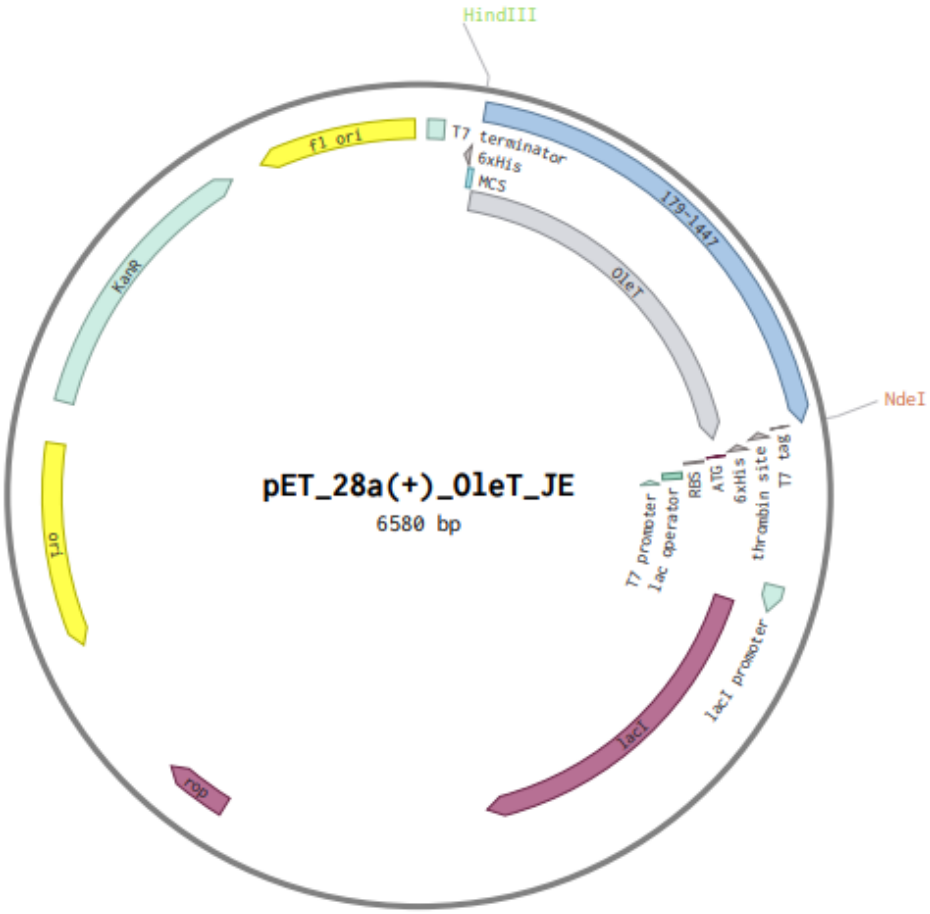

FIGURE 2.1 Map of pET28a(+) containing the $OleT_{JE}$ insert. The plasmid shows the HindIII and NdeI restriction sites used for insertion. Key features include the T7 promoter for high-level expression, Lac operator and LacI for IPTG inducible expression, an N-terminal His6-tag and thrombin cleavage site for protein purification, and kanamycin resistance.

Table 2.1 shows the primers designed in Benchling using the plasmid in Figure 2.1 as the template.

TABLE 2.1 The designed forward and reverse primers for each mutation. The table includes information such as the intended mutation and position within the OleT$_{JE}$ insert, residue abbreviation and codon for said residue, designed primers both forward and reverse, primer melting temperatures (T_m), codons changes, and GC content of each primer by percentage.

Mutation	*Substitution*	*Primer Type*	*Primer Sequence (5'→3')*	*Codon Changes*	*T_m (°C)*	*GC Content (%)*
A366P	Pro = CCG	Forward	5'-CATCGTTGT**cCg**GGTGAATGGATT-3'	GCC -> CCG	60.2	50.00
		Reverse	3'-ATTGGTCCAATAATCACCACCACCTTG-5'		59.2	44.44
G367P	Pro = CCG	Forward	5'-CATCGTTGTGCC**ccg**GAATGGATT-3'	GGT -> CCG	60.2	50.00
		Reverse	3'-ATTGGTCCAATAATCACCACCACCTTG-5'		59.2	44.44
E368P	Pro = CCG	Forward	5'-TGTGCCGGT**ccg**TGGATTACCGTG-3'	GAA -> CCG	61.4	54.17
		Reverse	3'-ACGATGATTGGTCCAATAATCACCACC-5'		59.1	44.44
Q354A	Ala = GCG	Forward	5'-CTGATTCCG**gcg**GGTGGTGGTGATTAT-3'	CAA -> GCG	60.9	48.15
		Reverse	3'-ATCGAACGGGCTACCATCCCAG-5'		60.2	59.09
N242A	Ala = GCG	Forward	5'-ATTGATCTGATG**gcg**ACCTTTCGTCCGCTG-3'	AAT -> GCG	60.7	43.33
		Reverse	3'-TGCACAGGTACGGCTATCCATCG-5'		60.5	56.52

As mentioned previously, the design strategy positioned the intended mismatch's shown in Table 2.1 at the centre of each forward primer (in lowercase and bold) to promote stable hybridization, ensure that the intended mismatch is not at the 3' end, and ensure balanced thermodynamic stability on both sides of the mismatch, thereby enhancing PCR efficiency and

chance of successful amplification. In the forward primers, bases that differ from the template sequence are shown in lowercase and bold. Bases that remain unchanged within a codon are written in uppercase and not bold.

Once PCR amplification was performed using the Q5 method with Phusion Pfu polymerase, agarose gel electrophoresis was conducted to identify amplified DNA and excise the target DNA band at ~6.6 kbps.

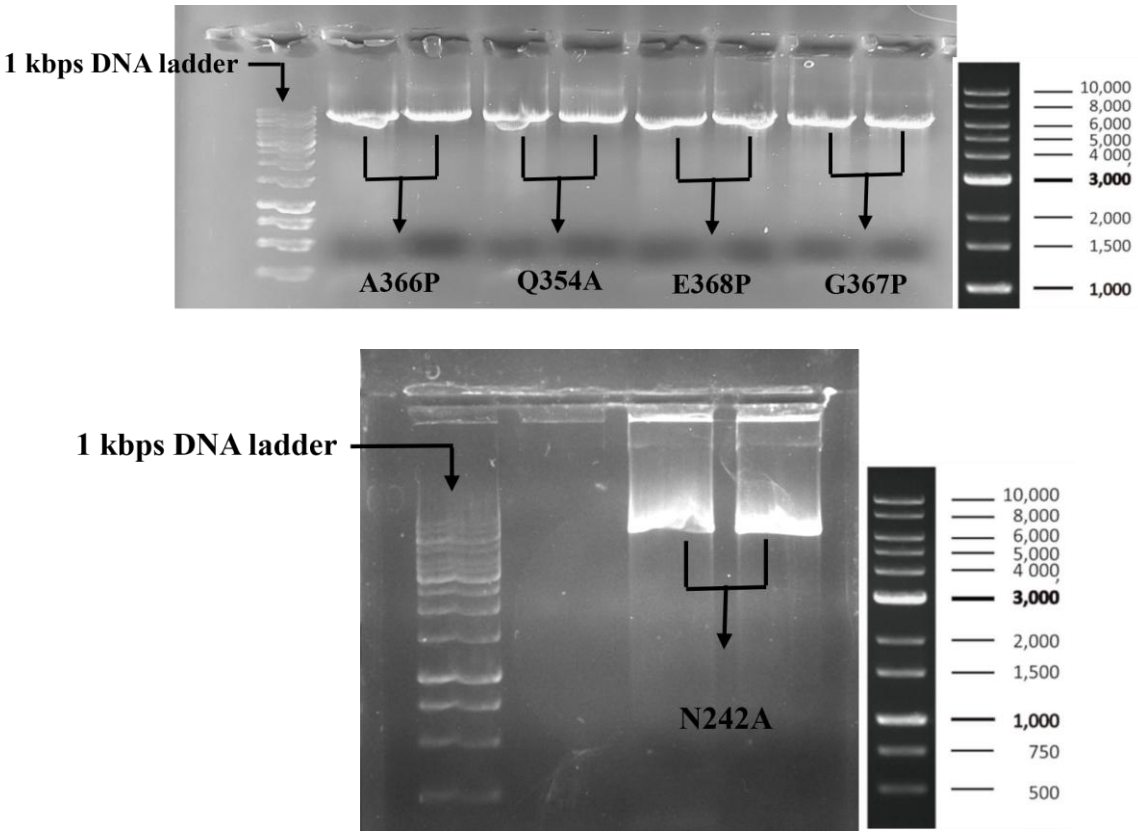

FIGURE 2.2 Images of agarose gel electrophoresis runs of Q5 PCR products. Agarose gel electrophoresis confirmed successful amplification of all $OleT_{JE}$ variants. Clear bands at ~6.6 kb, corresponding to the expected size of the pET28a(+) plasmid with insert, were observed for each mutant.

Following gel extraction, PCR clean-up, phosphorylation, ligation, transformation into TOP10 E. coli, and a DNA miniprep for selected colonies, clones were sent for DNA sequencing to

identify the presence of the intended mutations. Figure 3 shows an example of sequencing data for the A366P and wild-type sequence alignment using PDB pBLAST to corroborate the presence of the variant. Similar analysis for the other variants was conducted and data shown in Appendix1, revealing that clones containing the desired nucleotide changes for all five variants had been successfully obtained.

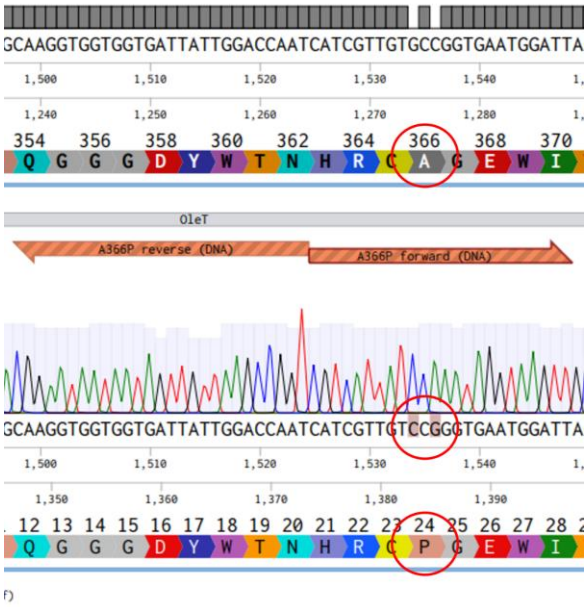

Score	Expect	Method	Identities	Positives	Gaps
719 bits(1857)	0.0	Compositional matrix adjust.	347/348(99%)	347/348(99%)	0/348(0%)

```
Query  1    NTLFGKGAIHTVDGKKHVDRKALFMSLMTEGNLNYVRELTRTLWHANTQRMESMDEVNIY  60
Sbjct  1    ............................................................  60

Query  61   RESIVLLTKVGTRWAGVQAPPEDIERIATDMDIMIDSFRALGGAFKGYKASKEARRRVED  120
Sbjct  61   ............................................................  120

Query  121  WLEEQIIETRKGNIHPPEGTALYEFAHWEDYLGNPMDSRTCAIDLMNTFRPLIAINRFVS  180
Sbjct  121  ............................................................  180

Query  181  FGLHAMNENPITREKIKSEPDYAYKFAQEVRRYYPFVPFLPGKAKVDIDFQGVTIPAGVG  240
Sbjct  181  ............................................................  240

Query  241  LALDVYGTTHDESLWDDPNEFRPERFETWDGSPFDLIPQGGGDYWTMHRCAGEWITVIIM  300
Sbjct  241  ...........................................P....P.....  300

Query  301  EETMKYFAEKITYDVPEQDLEVDLNSIPGYVKSGFVIKNVREVVDRT*  348
Sbjct  301  ..............................................*  348
```

FIGURE 2.3 Sequencing alignments between A366P and the wild-type sequence. Sequencing alignments between the A366P mutant and the wild-type sequence. The top alignment shows the wild-type $OleT_{JE}$ sequence and the A366P T7 terminator sequence, along with the chromatogram for A366P, demonstrating strong signal intensity (sharp peaks) with no crossovers. Codon and amino acid differences are circled in red. The bottom alignment, generated using pBLAST, confirms the presence of the intended mutation at the correct position (circled in red).

Over-expression and purification

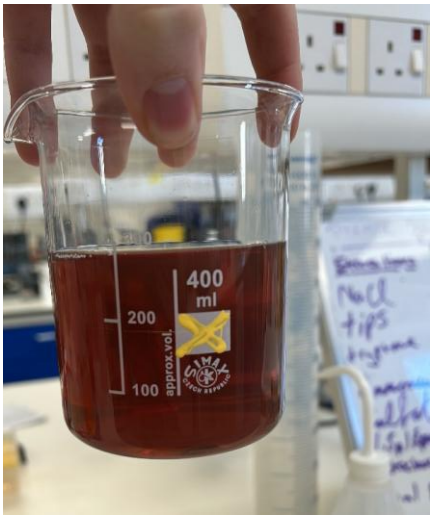

FIGURE 2.4 Images of clarified lysate. The left image was taken after cells were grown overnight, harvested and lysed using an Emulsiflex-C5, and then centrifuged to separate $OleT_{JE}$ from lysed cells before binding to a Ni-NTA column, as described in the experimental section

Following confirmation of the desired variant clone's glycerol stocks in E. coli C43(DE3) cells for protein expression were prepared. Protein expression for WT and all variants was carried out using the method described in the Experimental section. Some of the following figures illustrate the equipment used and additional images captured during the expression and purification process.

The clarified lysate shown in Figure 2.4 was loaded to a Ni-NTA column attached to an AKTA system, and the UV elution profile is shown in Figure 2.5. On increasing the % of buffer B a broad peak forms with the fractions eluted under this peak red in colour.

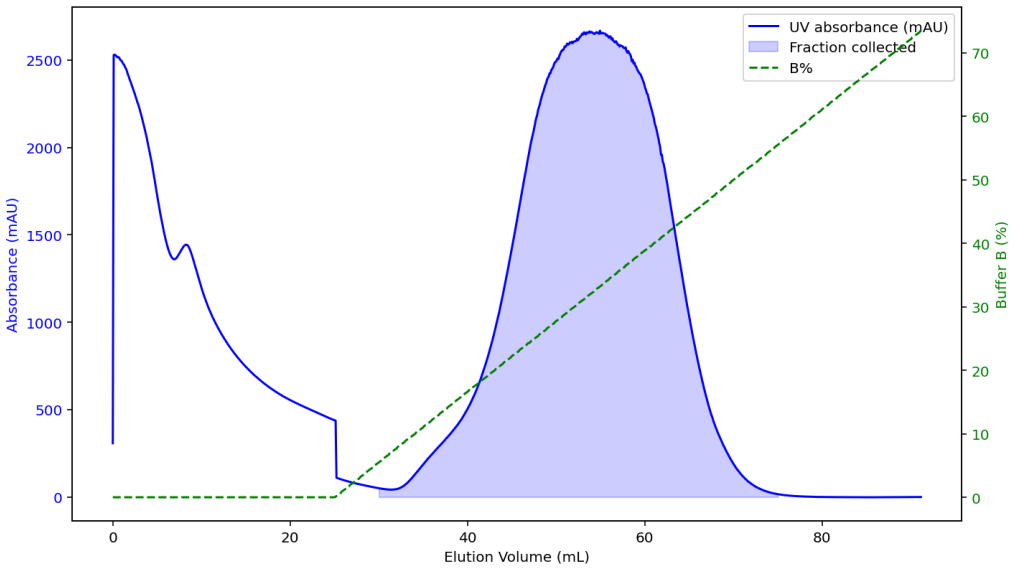

FIGURE 2.5 Elution profile of A366P from a Ni-NTA column. Absorbance spectra measured at 280 nm (blue) with eluted protein fractions collected in the blue shaded region. Concentration of buffer B increased linearly shown by the green dotted line.

Nickel affinity purification yielded a strong elution peak (~2500 mAU at 280 nm), consistent with high levels of protein bound to and released from the Ni-NTA column. Fractions under this peak were red in colour and pooled for further purification.

These fractions were collected and run on an SDS-PAGE. An illustrative example of the make-up of these fractions on an SDS-PAGE is shown for the A366P variant in Figure 2.6. It is clear from gel that the broad peak, seen in Figure 2.5, contains a band at the expected molecular weight for $OleT_{JE}$ (~50.4 kDa) that grows in intensity as the gradient increases.

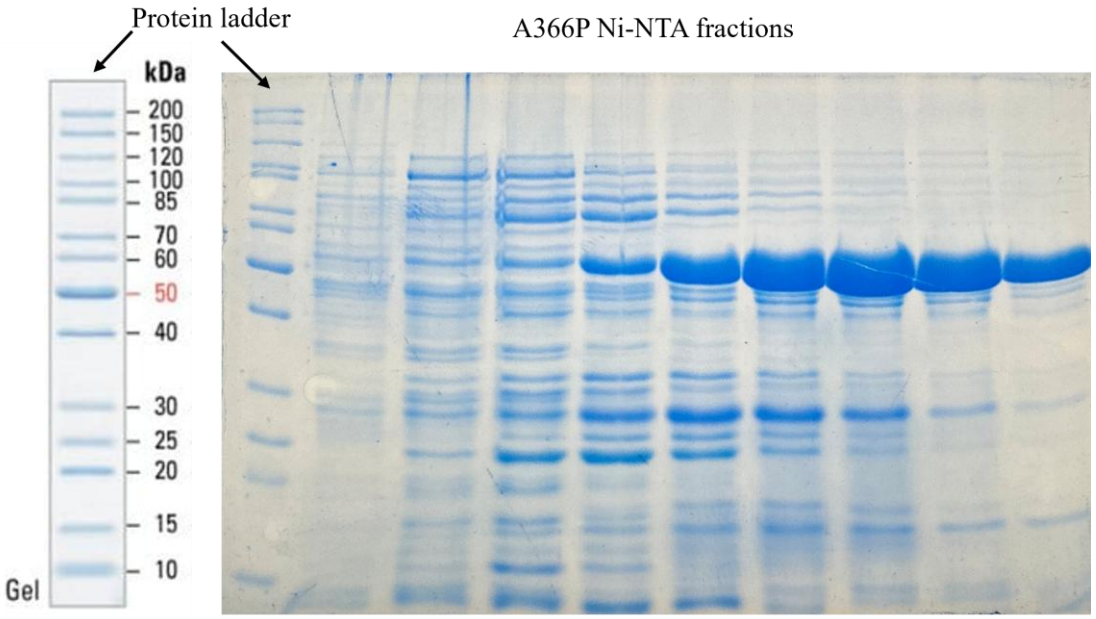

FIGURE 2.6 SDS-PAGE gel example of A366P elution's from Ni-NTA column. Each lane contains aliquots of 3 mL elution fractions from nickel column elution's where 280 nm absorbance was highest.

These fractions were pooled and concentrated (Fig. 2.7) to load to a S200 size exclusion column (Fig. 2.8). A single major peak eluted, with all fraction's red in colour. These were pooled, concentrated and used for experiments.

FIGURE 2.7. A366P fractions from Ni-NTA column pooled and concentrated. The image shows $OleT_{JE}$ in a 10 kDa molecular weight cut-off concentrator before being loaded to an S200 size exclusion column, as described in the experimental section.

FIGURE 2.8 Image of the S200 size exclusion column running with loaded $OleT_{JE}$. The major elution peak is at ~ 75 ml and is consistent with monomeric species with fractions of this peak being pooled and concentrated for experimentation.

During purification of each protein, some issues arose. The G367P and E368P variants showed negligible expression, which was corroborated by SDS-PAGE analysis seen in Figure 2.9. When comparing the gel in Figure 2.9 to the gel of A366P in Figure 2.6, a clear difference in band strength can be observed between proteins that expressed successfully (A366P) and those that did not (G367P and E368P). Another key observation for these variants showing no expression was no protein binding to the nickel when running the clarified lysate through the column. To further confirm this hypothesis, 12.5% SDS-PAGE run on the cell pellet, lysate, and flow through of each protein (if any) was conducted.

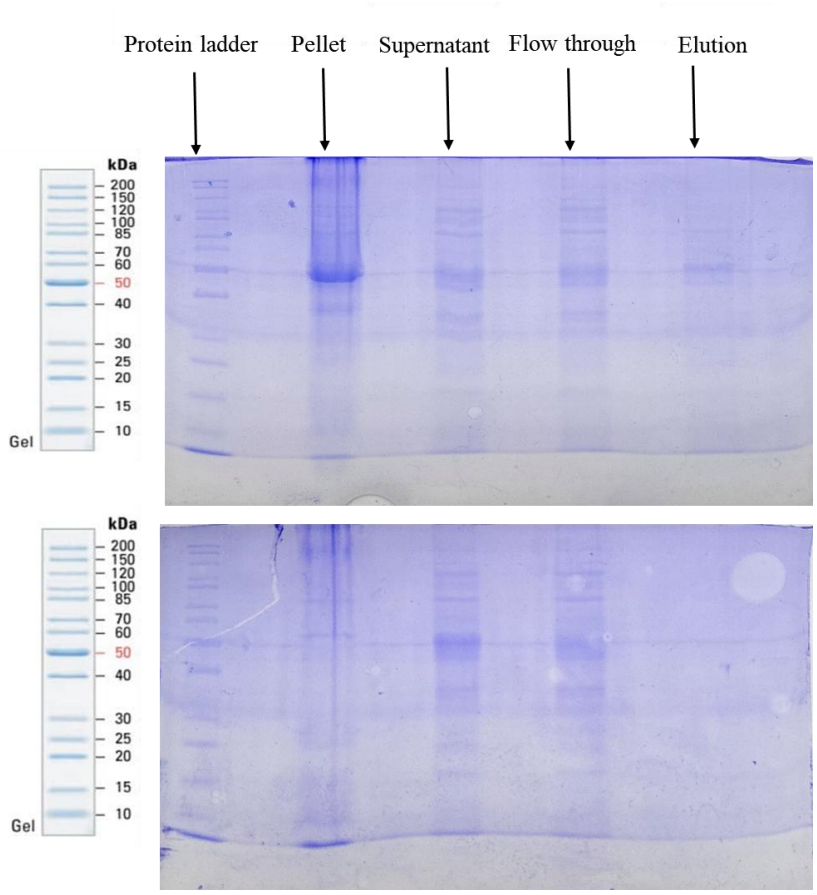

FIGURE 2.9 SDS-PAGE gels of mutants G367P (top) and E368P (bottom) post -expression. SDS-PAGE analysis revealed negligible expression of the G367P and E368P variants. No clear band at ~50.4 kDa was detected in the supernatant or elution fractions, in contrast to wild-type and other variants, indicating these proline substitutions abolished soluble expression

2.4 Discussion

All PCR reactions conducted in this study were successful, as confirmed by agarose gel electrophoresis and subsequent Sanger sequencing alignment (Figures 2.2 and 2.3). The sequencing results verified that the intended variants were correctly introduced into the pET28a(+) expression system without unwanted mutations, providing confidence in the molecular cloning strategy.

Despite the successful construction of all plasmids, not all variants expressed detectable protein. In particular, the G367P and E368P variants did not yield expression under the tested conditions. A likely explanation is the introduction of proline at these positions. Proline is well known as a structurally rigid residue that can disrupt α-helices or other secondary structural motifs due to its conformational constraints and inability to participate in backbone hydrogen bonding. This rigidity may have a destabilising effect at the introduced sites on the local secondary structure of $OleT_{JE}$, causing protein misfolding, inclusion bodies within the cell pellet, or affected interactions critical for stability that would lead to a well over-expressed protein. The lack of expression thus underscores the potential structural importance of residues G367 and E368 in maintaining a fold compatible with soluble expression.

Due to time constraints, no optimisation attempts were undertaken to rescue expression of these two proline variants. However, several strategies could be explored in future work. For example, supplying carbon monoxide (CO) during over-expression might improve heme incorporation and promote correct folding, as CO can bind to heme and stabilise the active site environment. This same technique is used for expressing DtpAa and DtpA peroxidases, where CO is bubbled into the growth media following induction by IPTG (Lučić, M et al., 2020). Similarly, supplementation with additives such as chaperones, cofactors (e.g., varying concentrations of δ-aminolevulinic acid addition for enhanced heme biosynthesis), or compatible solutes (e.g., sorbitol) may enhance folding efficiency and solubility (Xie, G et al.,

1997). Alternative host expression systems or lower induction temperatures could also be considered to promote correct protein folding.

2.5 Conclusion

With the successful overexpression of three target variants (N242A, A366P and Q354A) as well as the WT enzyme for use as a comparison, in-depth functional and structural characterisation of the variants can be undertaken. The subsequent chapters will present the results of fatty acid binding titrations, rapid kinetic measurements using stopped-flow spectroscopy, and high-resolution X-ray crystallographic studies. Together, these approaches aim to elucidate the molecular consequences of the introduced mutations and start to provide mechanistic insights into their functional roles.

Chapter 3

Spectroscopic, Thermodynamic, and Kinetic studies

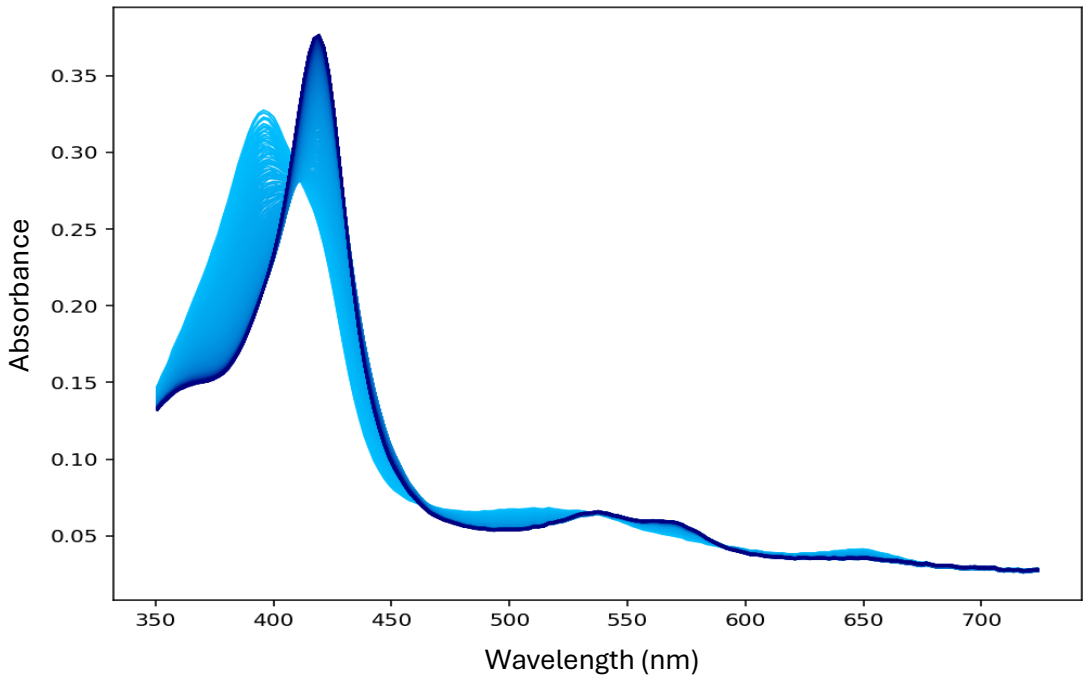

3.1 Introduction

With the variants A366P, Q354A and N242A of $OleT_{JE}$ successfully over-expressed and purified, understanding their effects on mechanisms of $OleT_{JE}$ fatty acid binding and the kinetics of the "peroxide shunt" pathway requires precise experimentation and analysis. In this chapter, the methodologies employed to investigate these processes are described in detail. Fatty acid binding titrations were carried out using three different length saturated alkyl chain fatty acids; icosanoic (C20:0), stearic (C18:0), and lauric (C12:0) acid. Kinetic measurements were performed using UV/Vis stopped-flow spectroscopy, with data collected using both a photodiode array and a photomultiplier tube to capture fast and slow kinetic phases enabling for the identification of ferryl heme intermediates.

3.2 Experimental Procedure

Electronic absorbance spectroscopy

All electronic absorbance spectra of $OleT_{JE}$ and variants were recorded on a Cary 60 UV–visible spectrophotometer (Agilent). Protein concentrations were determined using an extinction coefficient at 280 nm of $\varepsilon_{(280)} = 69.455\ mM^{-1}\ cm^{-1}$, while heme concentrations were measured from the low-spin Soret band at 417 nm using $\varepsilon_{(417)} = 109\ mM^{-1}\ cm^{-1}$ (Hsieh, C.-H et al., 2017) for fitting fatty acid binding titrations. To generate spectra of the ferrous carbon monoxide (CO) forms of $OleT_{JE}$, solid sodium dithionite (Fisher) was added directly to the cuvette, which was then sealed with parafilm. Reduction to the ferrous state was verified by acquiring a spectrum prior to addition of CO into the cuvette via a needle attached to a gas-tight glass syringe (Hamilton).

Fatty acid titrations

Prior to each titration, protein samples were treated with a 5-10-fold molar excess of hydrogen peroxide (H_2O_2, 30% w/w, Merck) to initiate a turnover of co-purified substrate. Excess H_2O_2

and reaction by-products were removed by passage through a PD-10 desalting column (Cytiva). Protein concentrations were adjusted to 4–5 μM in 1 mL quartz cuvettes containing buffer C (see Chapter 2). Fatty acid stocks (1 mM) of icosanoic acid (C20:0, Fisher), stearic acid (C18:0, Fisher), and lauric acid (C12:0, Fisher) were prepared by dissolving the fatty acids in either 70% ethanol with 30% Triton X-100 detergent, or in the case of lauric acid (C12:0), 100% ethanol to avoid detergent interference. Fatty acids were titrated to protein samples in 1 μL increments until full saturation was observed based on there being no further electronic absorbance changes in the Soret band region. Binding data was analysed using a Python-based fitting script implementing the Morrison quadratic equation for tight-binding ligands:

$$Y = \frac{([E]_t + [L]_t + K_d) - \sqrt{([E]_t + [L]_t + K_d)^2 - 4[E]_t[L]_t}}{2[E]_t}$$

(Eq.1)

where Y is the fractional saturation, $[E]_t$ is the total protein concentration, $[L]_t$ is the total ligand concentration, and K_d is the apparent dissociation constant.

Stopped-Flow Kinetics

Rapid kinetic measurements of the reaction between H_2O_2 and $OleT_{JE}$ (wild-type (WT) and variants) were performed using an SX20 stopped-flow spectrophotometer (Applied Photophysics, UK) equipped with either a photodiode-array (PDA) multi-wavelength detection unit or a photomultiplier tube (PMT), and operated at 10 °C. All the as-purified (fatty acid bound) WT and variant samples were prepared in buffer D (100 mM sodium phosphate, 500 mM NaCl, pH 7.5) to a final protein concentration of approximately 5 μM after mixing with H_2O_2. Final H_2O_2 concentrations after mixing ranged from 1000 μM to 16 μM, serially halved between shots. Data obtained from the PDA were analysed globally following singular value

decomposition (SVD) using Pro-KIV Kinetic Global Analysis software (Applied Photophysics, UK) and fitted to a sequential model (A → B → C). Data from the PMT was averaged over 5-10 individual time courses and fitted to a single exponential, yielding both rate constants and associated absorbance changes which were plotted.

Temperature dependent UV-visible spectroscopy

Electronic absorbance spectra of WT $OleT_{JE}$ were recorded at various temperatures using an SX20 stopped-flow spectrophotometer (Applied Photophysics, UK) connected to a water circulator. Spectra were collected using the PDA multi-wavelength detector on the internal trigger. The relative amounts of high-spin and low-spin heme species at each temperature were determined using the extinction coefficients of their respective Soret peaks (ε_{396} = 91 mM^{-1} cm^{-1} for high-spin; ε_{417} = 117 mM^{-1} cm^{-1} for low-spin) (Hsieh, C.-H et al., 2017). No published molar extinction coefficient was available for the high-spin ferric Soret band at 396 nm. Because molar extinction coefficients for P450 Soret bands are typically of the same order of magnitude (≈90–110 $mM^{-1}\cdot cm^{-1}$, depending on spin state and measurement method), a value of 91 mM^{-1} cm^{-1} was adopted here as an apparent extinction coefficient for the high-spin 396 nm band. This approximation was chosen to enable relative quantitation, with the caveat that the true extinction coefficient at 396 nm may differ. From these values, the spin equilibrium constant (K_{spin}) was calculated as the ratio of [high-spin]:[low-spin]. The equilibrium constants obtained across the temperature range were then used to generate van't Hoff plots, from which the enthalpy change (ΔH) and entropy change (ΔS) were extracted according to equation (2):

$$\ln K = -\frac{\Delta H}{RT} + \frac{\Delta S}{R} \qquad \text{(Eq.2)}$$

where R is the gas constant (8.314 $J\cdot K^{-1}\cdot mol^{-1}$) and T is the absolute temperature (K). The Gibbs free energy (ΔG) of $OleT_{JE}$ at 293.15 K was determined using equation (3):

$$\Delta G = \Delta H - T\Delta S$$

(Eq.3)

and the equilibrium constant for the spin-shift equilibrium (K_{spin}) at the same temperature was determined using equation (4).

$$K_{\text{spin}} = e^{-\Delta G/RT}$$

(Eq.4)

3.3 Results

Electronic absorption spectra of as-purified and H_2O_2 treated $OleT_{JE}$ and variants

The electronic absorption spectrum of as-purified $OleT_{JE}$ is presented in Figure 3.1, alongside the spectrum recorded after treatment with H_2O_2. In the as-purified state, the spectrum displays a broad, Soret feature with maxima at 396 and 417 nm, together with a Q-band absorption features at approximately 650 nm, consistent with a charge-transfer transition characteristic of a thiolate-ligated high-spin Fe(III) heme (Fig. 3.1). Following the addition of H_2O_2, the Soret band sharpens, increases in intensity, and undergoes a red shift to a single maximum at 417 nm (Fig. 3.1). In parallel, distinct changes occur in the Q-band region: two new peaks appear at 537 and 568 nm, while the 650 nm Cys–Fe(III) charge-transfer band decreases in intensity (Fig. 3.1). Collectively, these spectral shifts indicate a transition from an as-purified species comprising a mixture of high- and low-spin Fe(III) heme states to one predominantly in the low-spin Fe(III) state. This observation supports the proposal that $OleT_{JE}$ co-purifies with a bound substrate that stabilises the high-spin configuration. Such a transition has been attributed to displacement of an axially coordinated water ligand to generate a five-coordinate heme iron (Belcher, J et al., 2014). It is well established in the CYP152 literature that members of this P450 family tend to co-purify with a fatty acid (Girvan, H. M et al., 2018). For example, CYP152K6 from *Bacillus methanolicus* was crystallised with tetradecanoic acid (C14:0) bound in its active site. Notably, the fatty acid was incorporated during the enzyme's expression in *E. coli*, as no fatty acids were present in the crystallisation conditions (Girvan, H. M et al., 2018).

For the as-purified $OleT_{JE}$ variants, the equilibrium between the high-spin species at 396 nm and the low-spin species at 417 nm within the Soret region shows differences compared to the WT protein. Specifically, the A366P and Q354A variants show a greater relative contribution from the 396 nm high-spin state (Fig. 3.1 and Fig. 3.2), whereas N242A retains a broad Soret

pattern nearly identical to the WT, suggesting that this variant has little to no alteration in its spin-state distribution (Fig. 3.1).

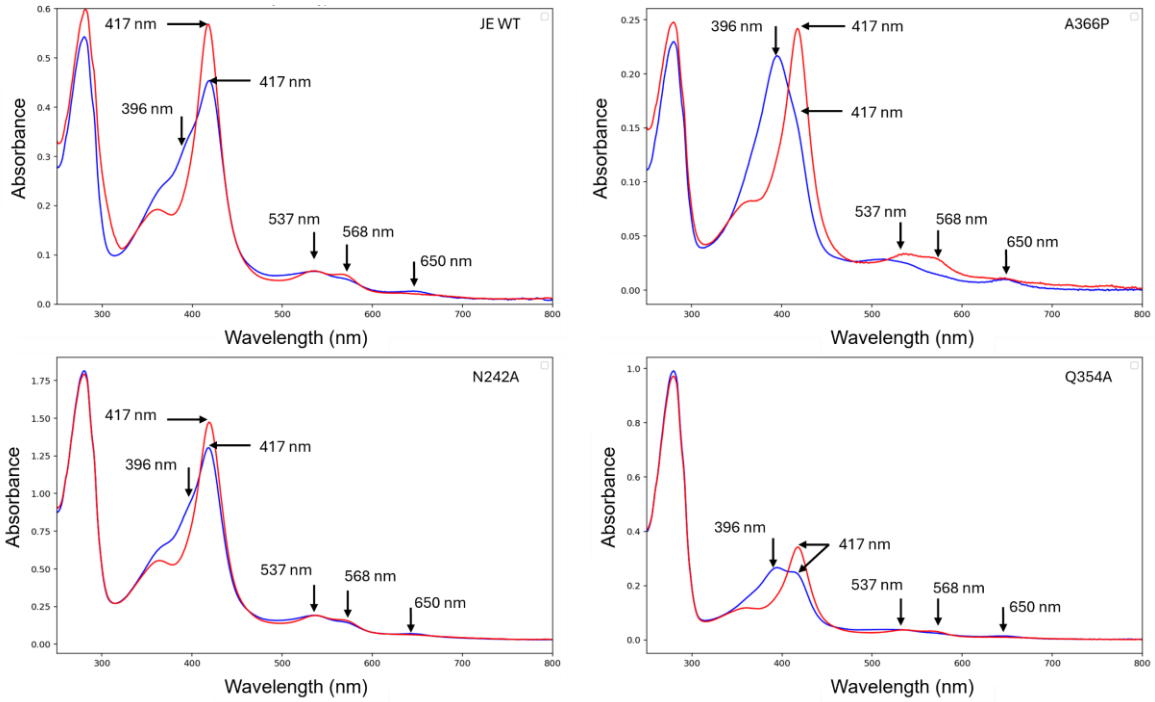

FIGURE 3.1. Electronic absorbance spectra of OleT$_{JE}$ WT (top left), A366P (top right), N242A (bottom left), and Q354A (bottom right) variants. The blue spectra represents as purified protein and the red spectra represents H_2O_2 treated protein. All spectra show the aromatic absorbance peak (280 nm) where protein concentration is determined using the Beer-Lambert law and extinction coefficient ε_{280} = 69,455 mM^{-1} cm^{-1}. The spectra also show the split Soret region of the as purified spectra and the H_2O_2 treated Soret region where heme concentrations were determined at high- or low-spin, respectively. The Beer-Lambert law was employed here as well using ε_{417} = 117 mM^{-1} cm^{-1} for low-spin species, and ε_{396} = 91 mM^{-1} cm^{-1} for high-spin species.

The electronic absorbance spectra of Q354A shows a noticeable difference in the ratio between the aromatic (280 nm) and Soret regions (396 and 417 nm). By comparison, the WT protein and variants N242A and A366P exhibit a near 1:1 ratio between aromatic and Soret region peaks, suggesting full heme occupancy for each monomer. The 1:1 ratio between the aromatic and Soret region peaks is well supported in the literature, as all published OleTJE electronic absorbance spectra consistently exhibit this ratio (Matthews, S et al., 2017; Belcher, J et al., 2014). This cannot be said for Q354A as the large difference in ratio suggests issues with heme loading when over-expressing. Figure 3.2 focuses in on the Soret region to better represent its features, notably the split between 396 nm (high spin) and 417 nm (low spin). When compared to WT the Q354A variant expresses more of a high-spin characteristic but still maintains some of the low-spin characteristic.

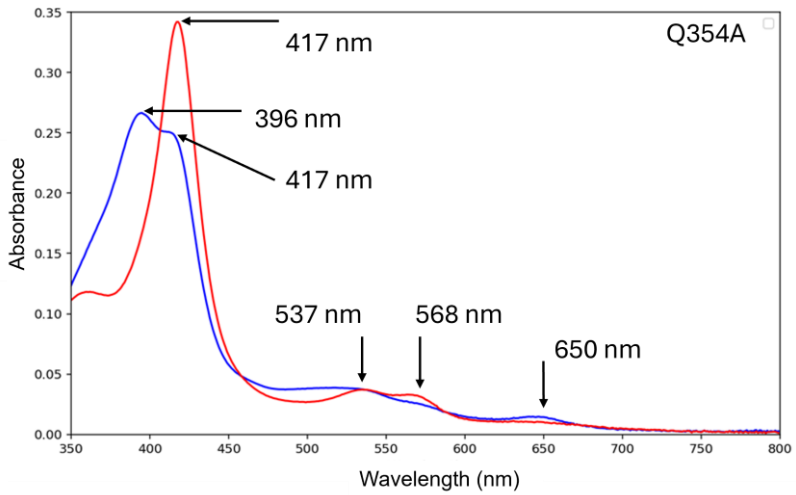

FIGURE 3.2. Electronic absorbance spectra of Q354A, drawing attention to the Soret and Q-band regions by removal of the aromatic peak. The Blue spectra represents as purified protein and the red spectra represents H_2O_2 treated protein.

Upon reduction of Fe(III) to Fe(II) with dithionite in a CO-saturated solution, whether starting with as-purified (Fig. 3.3) or H_2O_2-treated (Fig. 3.4) $OleT_{JE}$, the absorption spectra indicate the formation of an Fe(II)–CO heme complex. In both cases, the WT spectra is marginally more P450 dominant compared to P420, characterised by a Soret maximum at ~450 nm, with a lower-intensity P420 band appearing at ~420 nm, whereas proximal mutants favour the P450,

increasing the thiolate contribution, whereas the N242A P420 dominates (thiol) This not only

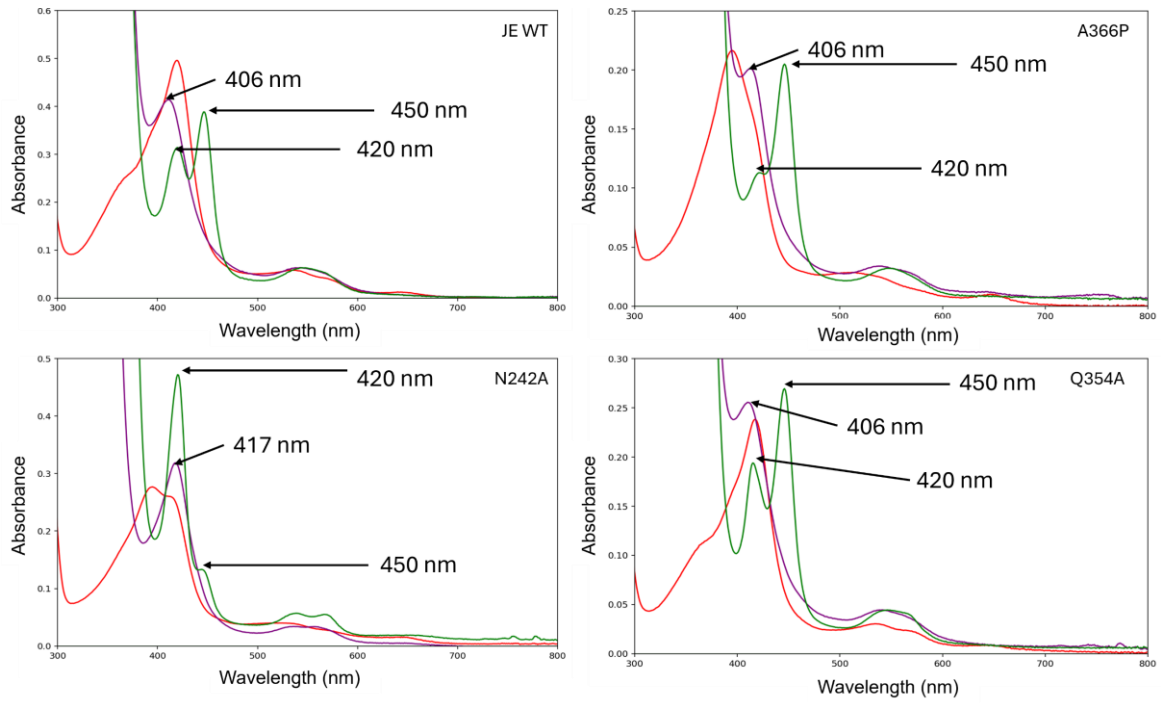

FIGURE 3.3. Electronic absorbance spectra of CO bound heme. As purified (red) WT $OleT_{JE}$ (top left), A366P (top right), N242A (bottom left), and Q354A (bottom right) after the addition of sodium dithionite (λmax 406 nm (purple)) and addition of CO (420 and 450 nm peaks (green) at pH 7.5.

confirms that CO binds effectively to the reduced Fe(II) heme regardless of substrate presence, but also confirms that both axial and proximal variants express favourability to either of the cysteine thiol/thiolate states. The predominance of the P450 feature suggests that the proximal cysteine ligand is in the thiolate (deprotonated) form under the measured pH (7.5), unlike the P420 form, which corresponds to a protonated thiol-ligated heme. This interpretation aligns with established spectroscopic assessments in cytochrome P450 literature, where the 450 nm CO-bound band is attributed to the thiolate-ligated, active P450 species, while the 420 nm band marks the protonated, inactive P420 form (Gable, J.A et al., 2022).

In the as-purified $OleT_{JE}$ variants (Fig. 3.3), differences in the rations between the split Soret region after formation of the Fe(II)-CO complex (420 and 450 nm) appear. The P450 character

within the WT (Fig 3.3 top left) is more prominent when compared to the P420 suggesting that the axial cysteine ligand has more of a deprotonated thiolate character.

By comparison, both A366P and Q354A express higher absorbance at 450 nm and lower absorbance at 420 nm regions when compared to the WT. This change suggests the proximal Cys ligand in these variants coordinates the heme with more of a thiolate character when compared to WT. When compared with each other, the 420 nm characteristic within A366P is more diminished than seen in Q354A suggesting a greater presence of the deprotonated thiolate character. Together these findings suggest that the proximal variants, comparatively, have affected the protonation of the axial cysteine (thiol or thiolate) as a consequence of removing hydrogen bonding capacity. The N242A variant expresses the opposite, having a markedly higher absorbance at 420 nm and a significantly reduced absorbance at 450 nm that the WT, suggesting a higher presence of heme Cys thiol character. The same variant characteristics observed for the as-purified Fe(II)-CO complex (red spectra in Figure 3.4) are observed in the H_2O_2 treated Fe(II)-CO complex (Fig. 3.4), although upon dithionite addition, transition from 417 nm to 406 nm appears not to occur. Regardless, the Fe(II)-CO complex still forms after the addition of CO (Fig. 3.4).

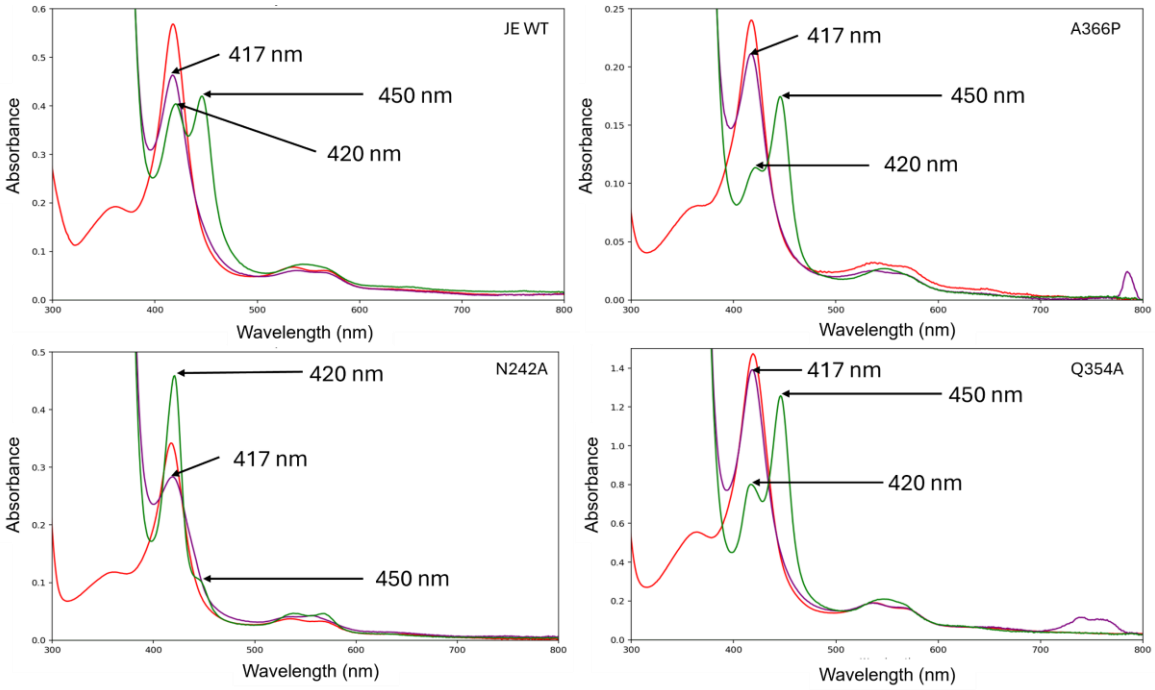

FIGURE 3.4. Electronic absorbance spectra of CO bound heme after H_2O_2 treatment (red). WT $OleT_{JE}$ (top left), A366P (top right), N242A (bottom left), and Q354A (bottom right) after the addition of sodium dithionite (λmax 417 nm (purple)) and addition of CO (420 and 450 nm peaks (green)).

Titration of fatty acid substrates to $OleT_{JE}$ WT and variants

Beginning with H_2O_2-treated WT $OleT_{JE}$ and variants, substrate-dependent changes in the low-spin Fe(III) heme Soret and Q-band regions were observed upon titrations with icosanoic acid (C20:0), stearic acid (C18:0), or lauric acid (C12:0) (Fig. 3.5, 3.6, 3.7, respectively). These fatty acids were selected based on previous studies demonstrating their ability to bind to $OleT_{JE}$ (Belcher, J et al., 2014; Matthews, S et al., 2017). With increasing concentrations of the longer saturated alkyl chain substrates, C20:0 and C18:0, the spectra exhibited a pronounced split Soret feature together with the appearance of a band at 650 nm, consistent with the spectral signature observed for the as-purified protein (Fig. 3.1) and characteristic of a transition from a low- to high-spin Fe(III) heme state (Fig. 3.5, 3.7). In contrast, titrations with the shorter saturated alkyl chain C12:0 fatty acid produced only subtle spectral changes, with evidence for

minimal accumulation of the high-spin species (Fig. 3.8). Upon reaching spectral saturation, defined as the point at which further substrate addition produced no additional changes, a 5- to 10-fold molar excess of H_2O_2 was introduced. In all cases, this treatment resulted in the reappearance of the low-spin Fe(III) spectrum (as shown in Fig. 3.1), suggesting that the bound fatty acids were subsequently turned over.

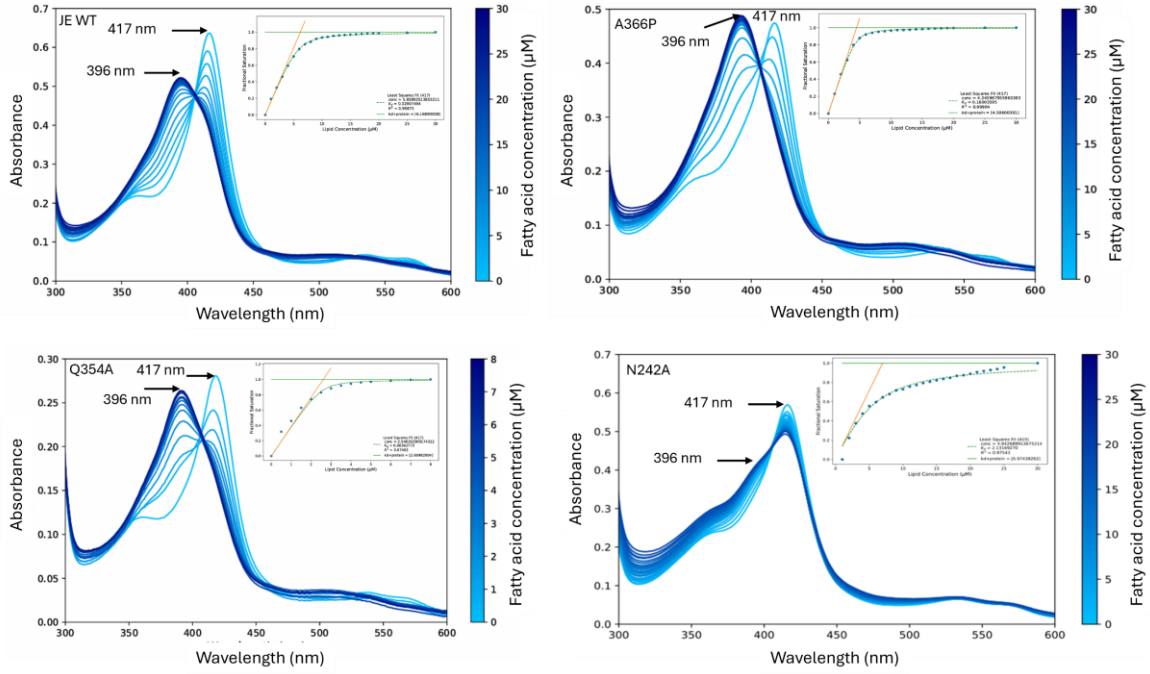

FIGURE 3.5. Fatty acid binding Titrations. WT $OleT_{JE}$ (top left) and variants A366P (top right), Q354A (bottom left), and N242A (bottom right) using C20:0 fatty acid dissolved in 70% ethanol and 30% Triton X100 detergent. Insets show the respective fractional saturation binding isotherms with fits and stoichiometry of binding indicated.

To quantify substrate binding, difference absorbance values ($A_{396} - A_{419}$) were plotted as a function of substrate concentration. Fractional saturation curves were generated from these data (inset, Fig. 3.5–3.8), and binding isotherms were fitted to yield dissociation constants (K_d), which are summarised in Table 3.1. Furthermore, the fitted binding isotherms meet with the stoichiometry of a monomeric species (1:1) as when substrate concentration meets protein concentration, the fits begin to plateau at the point of intersect where $K_d = \infty$ (orange) and fractional saturation is 1 (green).

For the N242A variant, it was determined that the use of Triton X-100 interfered with the binding measurements of C20:0 (Fig. 3.6 (top)). As a result, C20:0 was instead dissolved in 100% ethanol; however, upon addition to the 1 mL protein solution in the cuvette, the fatty acid aggregated. This aggregation effectively halved the bioavailable concentration of C20:0, producing an apparent 2:1 stoichiometry rather than the expected 1:1 binding stoichiometry. To better reflect the true binding interaction, the fatty acid concentration was manually halved during data analysis. Under these conditions, the resulting fractional saturation curve more closely resembled the expected 1:1 binding profile, as indicated by the rightward shift of the isotherm relative to the WT curve shown in Figure 3.6 (bottom).

To rule out the possibility of experimental error, fresh fatty acid stocks were prepared prior to each titration. Initially, the concentration correction was applied computationally to the acquired dataset; subsequent titrations were then performed experimentally using half the original substrate concentration. Despite this adjustment, the same challenges in producing a clear 1:1 stoichiometry remained. Further investigation revealed that the use of 100% ethanol as a solvent was a major contributing factor. Specifically, when 1 μL of the C20:0 ethanol stock was added to 1 mL of protein solution, the ethanol concentration dropped to only 0.1%. Due to the extreme hydrophobicity of C20:0, this rapid dilution promoted the formation of insoluble fatty acid aggregates, reducing effective substrate availability. Attempts to overcome this by preparing stock solutions in more dilute ethanol–water mixtures were unsuccessful, as C20:0 aggregated during stock preparation and could not be redissolved.

Given these limitations, the binding kinetics reported here represent the most practical description of the system achievable under the experimental conditions.

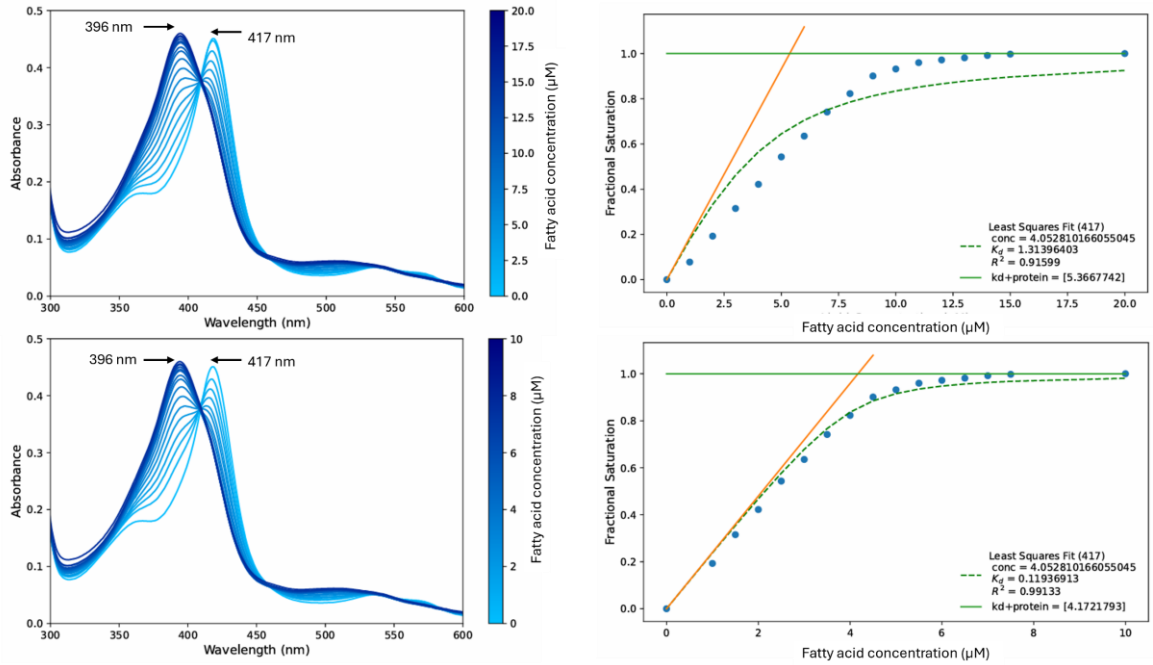

FIGURE 3.6. Titrations of the N242A variant with C20:0 dissolved in 100% ethanol. Spectral changes and the resulting binding isotherms expressing 2:1 binding stoichiometry (top) and 1:1 binding stoichiometry (bottom) are reported.

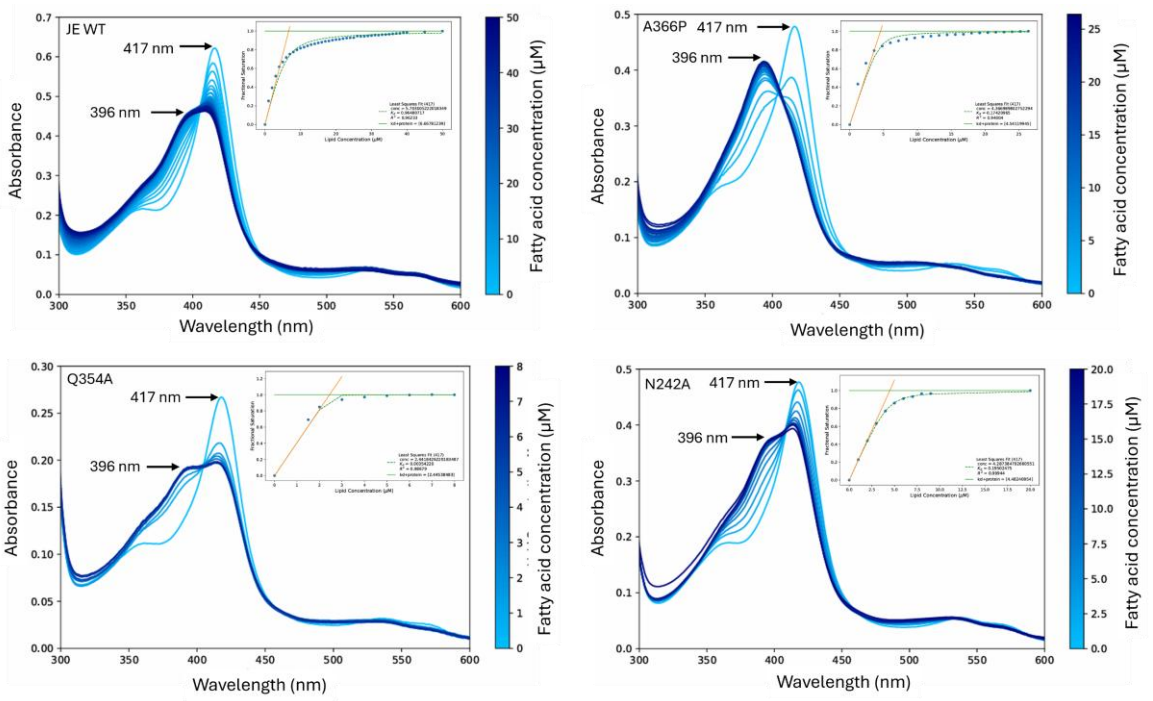

FIGURE 3.7. Titrations with C18:0. WT $OleT_{JE}$ (top left) and variants A366P (top right), Q354A (bottom left), and N242A (bottom right). The C18:0 fatty acid was dissolved in 70% ethanol and 30% Triton X100 detergent but in 100% ethanol for N242A.

The N242A titration with C12:0 appeared to show negligible spectroscopic changes range in the 396 nm region and only a reduction in the 417 nm region (Fig. 3.9). Upon fractional saturation analysis, a K_d value could be produced which was consistent with a binding even despite little spectroscopic change in the typical high-spin 396 nm range.

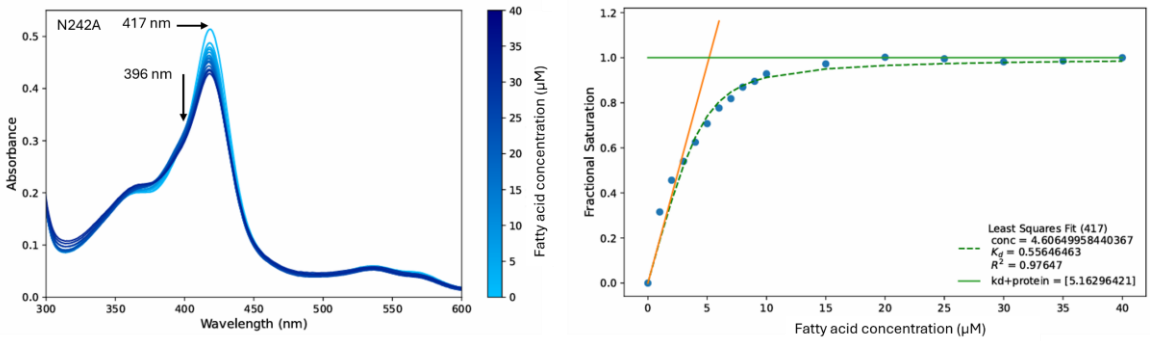

FIGURE 3.9. Electronic absorbance titration of N242A with C12:0 dissolved in 100% ethanol.

The apparent K_d values suggest altered affinities for long and short saturated alkyl-chain fatty acids between WT and variant proteins (Table 3.1). Further discussion points on these values are explored in the Discussion section of this chapter.

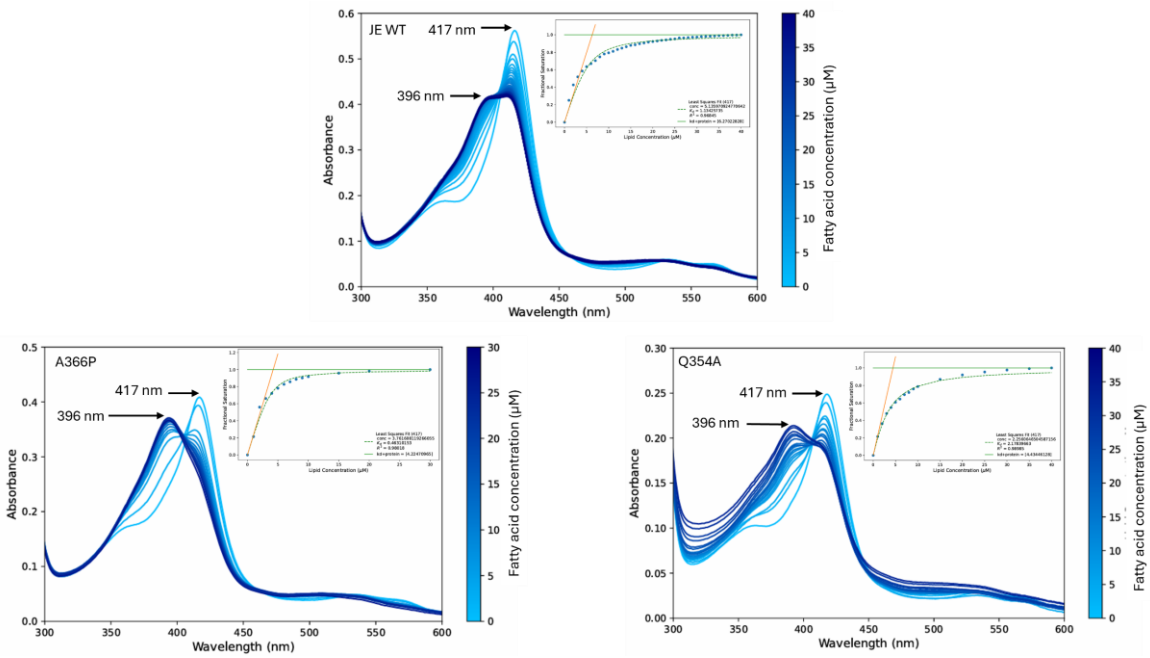

FIGURE 3.8. Titrations with C12:0 fatty acid. WT $OleT_{JE}$ (top) and variants A366P (bottom left), Q354A (bottom right). The C12:0 fatty acid was dissolved in 100% ethanol.

TABLE 3.1. Apparent K_d values from fitted binding isotherms. Table includes apparent K_d values for WT $OleT_{JE}$ and respective variants for their respective fatty acids, C20:0, C18:0, and C12:0. To note, the K_d provided for the N242A titration using C20:0 was derived by computational alteration (see Fig. 3.6). The K_d was derived from the Morrison equation for tight binding ligands using data from titrations of fatty acids at 18 °C and a pH 7.5.

OleT variant	*K_d (μM) for C20:0*	*K_d (μM) for C18:0*	*K_d(μM) for C12:0*
JE WT	0.33 ± 0.014	0.96 ± 0.084	1.13 ± 0.086
A366P	0.16 ± 0.0083	0.17 ± 0.063	0.46 ± 0.067
Q354A	0.064 ± 0.024	0.004 ± 0.014	2.18 ± 0.11
N242A	0.12 ± 0.021	0.2 ± 0.009	0.56 ± 0.081

Stopped-flow reaction kinetics of as-purified WT $OleT_{JE}$ and variants with H_2O_2

While titrations provided the overall binding affinity of $OleT_{JE}$ for its substrate, they do not reveal how quickly the reaction of a complex between $OleT_{JE}$ and H_2O_2 progressed through intermediate states. To capture these dynamic steps, we next turned to stopped-flow spectroscopy. By rapidly mixing $OleT_{JE}$ with H_2O_2 and monitoring spectral changes over milliseconds, we could resolve the individual kinetic phases of the reaction with the bound fatty acid. This approach not only allowed us to extract second-order rate constants for the initial binding step but also to define the subsequent transitions within a sequential A→B→C mechanism.

Stopped-flow absorption kinetics were measured by mixing H_2O_2 with as-purified WT and variant $OleT_{JE}$ proteins. This produced rapid spectral transitions (Fig. 3.10–3.13) consistent with the electronic absorbance spectral changes upon addition of a molar excess of H_2O_2 (Fig.

3.1). Global analysis following mixing with H_2O_2 identified two kinetic phases, with an intermediate displaying wavelength features consistent with a Compound II (Fe(IV)–OH) species. The primary feature observed was a red-shifted Soret maximum at 426 nm with reduced absorbance relative to the Fe(III) heme maximum at 417 nm (Munro, A.W. et al., 2018) (Fig. 3.10–3.13). Within the component spectra, **A** represents the initial spectra, **B** represents Compound II and **C** represents the return to protein resting state.

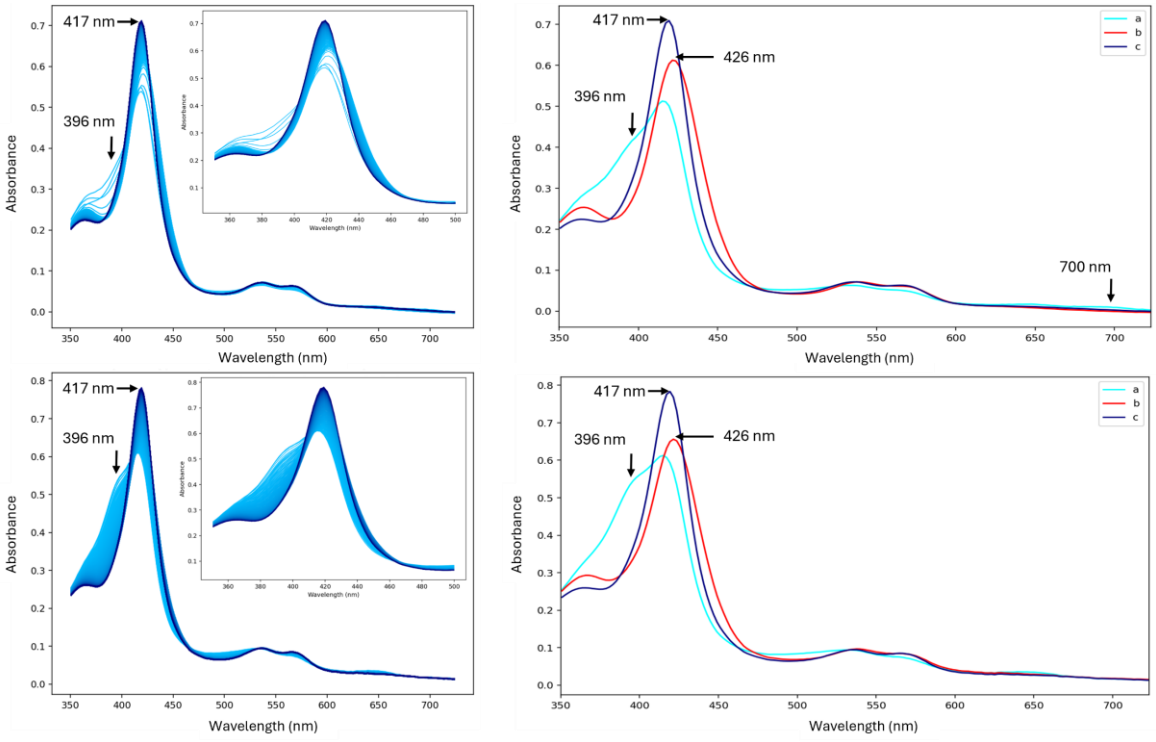

FIGURE 3.10. Stopped-flow spectra and component analysis of as-purified WT OleTJE mixed with H_2O_2. Spectral changes were monitored over 0.4 s with 400 time points following mixing of as-purified protein (5 µM) with either high (1 mM; 200-fold excess (top)) or low (31.25 µM; 6.25-fold excess (bottom)) H_2O_2 concentrations. Both concentrations show a complete transition from the high-spin (fatty acid-bound) to low-spin (resting) Fe(III) state, with the slower transition at low H_2O_2 allowing clearer resolution of the fast phase, as seen by the higher absorbance at 396 nm within the split Soret region of the component spectra. Insets highlight the Soret region to illustrate these changes. Component spectra obtained by single value decomposition revealed sequential conversion of the fatty acid-bound state (a) to Compound II (b, λ_{max} 426 nm), and finally to the resting state (c). At high peroxide concentration (1 mM), weak absorbance at 700 nm was also observed in component (a), consistent with the presence and decay of a Compound I species.

Following stopped-flow experiments with the WT protein, the same experiments were conducted using the variants A366P, N242A and Q354A, and are illustrated in Figures 3.11-3.13.

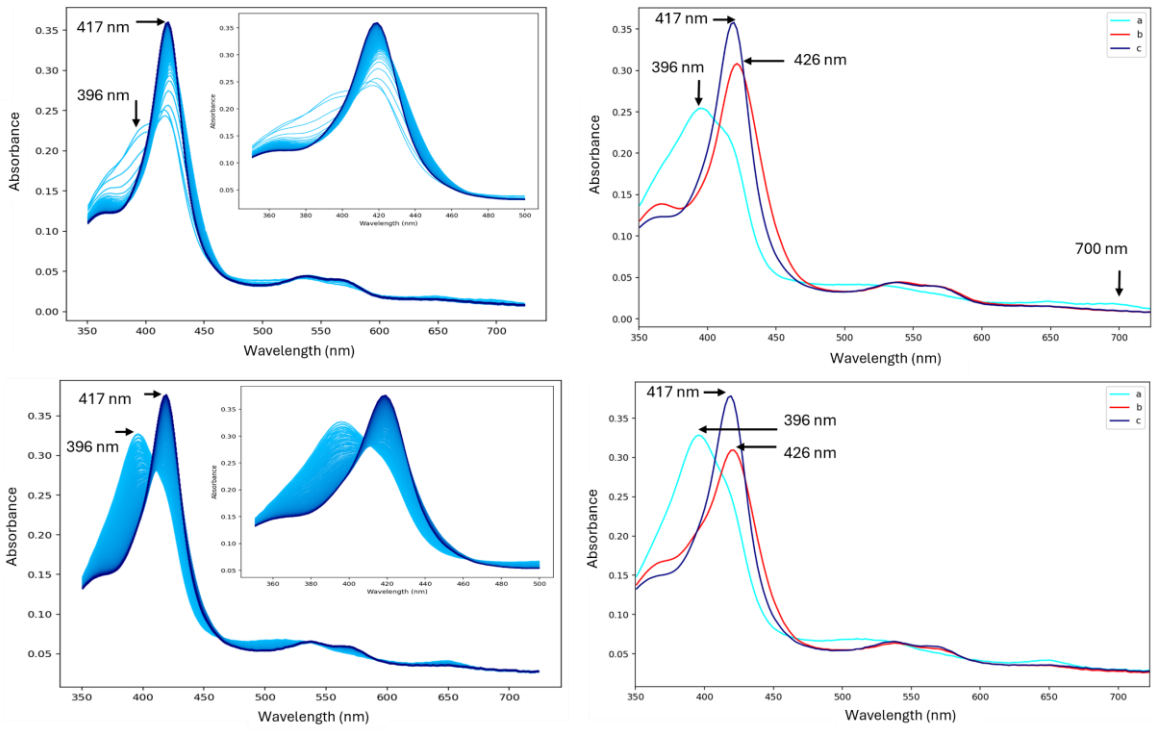

FIGURE 3.11. Stopped-flow of A366P when mixed with 1 mM H_2O_2 (top left), and when mixed with 16 µM H_2O_2 (bottom left), and their respective component spectra. Spectral changes show the transition from as-purified high-spin to low-spin resting state of the protein upon addition of H_2O_2. Spectra were recorded over 0.4 s with 400 time points. High H_2O_2 concentration (200-fold molar excess; 1 mM H_2O_2, 5 µM protein) showing rapid conversion with limited resolution of intermediates. Spectral deconvolution by SVD highlights transitions from the fatty acid-bound state (396 nm) to compound II (426 nm) and the final resting state (417 nm). A minor feature at 700 nm indicates compound I formation, made visible due to the high H_2O_2 excess. Lower H_2O_2 concentration (3.2-fold molar excess; 16 µM H_2O_2, 5 µM protein) slows the reaction, enabling clearer visualisation of intermediate species, particularly the fatty acid-bound state (396 nm). Spectral deconvolution by SVD highlights distinct contributions from the fatty acid-bound high-spin species (396 nm), compound II (426 nm), and resting low-spin state (417 nm).

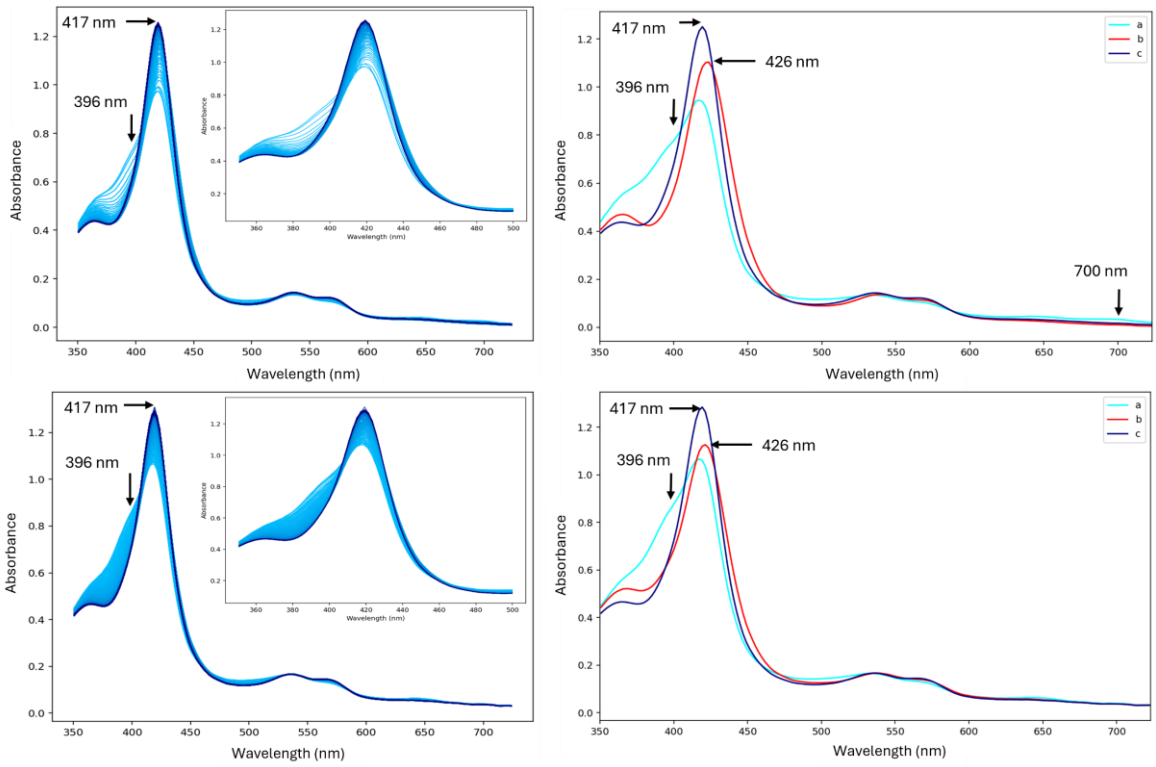

FIGURE 3.12. Stopped-flow of the as-purified N242A variant when mixed with 1 mM H_2O_2 (top left), when mixed with 62.5 µM H_2O_2 (bottom left), and their respective component spectra. Spectral changes show the transition from fatty acid-bound high-spin to low-spin resting state of the protein upon addition of H_2O_2. Spectra were recorded over 0.4 s with 400 time points. High H_2O_2 concentration (200-fold molar excess; 1 mM H_2O_2, 5 µM protein) showing rapid conversion with limited resolution of intermediates. Spectral deconvolution by SVD highlights transitions from the fatty acid-bound state (396 nm) to compound II (426 nm) and the final resting state (417 nm). The 700 nm feature indicates compound I formation, made visible due to the high peroxide excess. Lower peroxide concentration (12.5-fold molar excess; 62.5 µM H_2O_2, 5 µM protein) slows the reaction, enabling clearer visualisation of intermediate species, particularly the fatty acid-bound state (396 nm). Spectral deconvolution by single value decomposition highlights distinct contributions from the fatty acid-bound high-spin species (396 nm), compound II (426 nm), and resting low-spin state (417 nm).

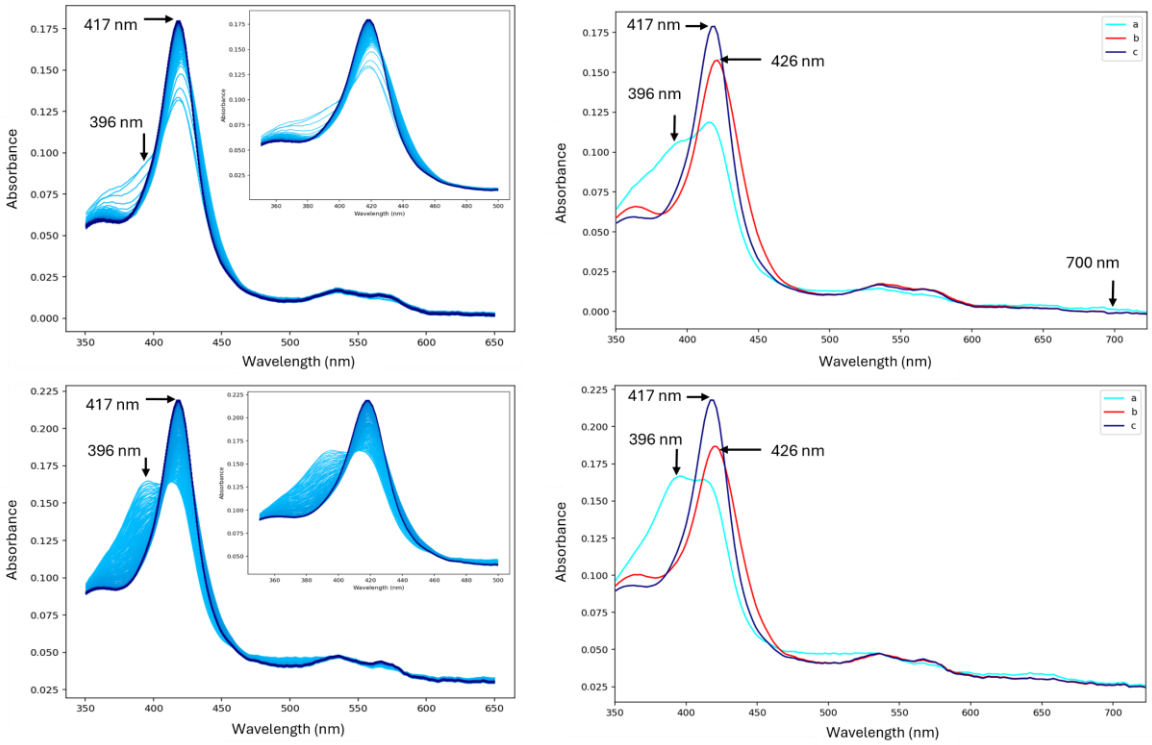

FIGURE 3.13. Stopped-flow of the as-purified Q354A variant when mixed with 1 mM H_2O_2 (top left), when mixed with 16 µM H_2O_2 (bottom left), and their respective component spectra. Spectral changes show the transition from fatty acid-bound high-spin to low-spin resting state of the protein upon addition of H_2O_2. Spectra were recorded over 0.4 s with 400 time points. High H_2O_2 concentration (200-fold molar excess; 1 mM H_2O_2, 5 µM protein) showing rapid conversion with limited resolution of intermediates. Spectral deconvolution by SVD highlights transitions from the fatty acid-bound state (396 nm) to compound II (426 nm) and the final resting state (417 nm). A minor feature at 700 nm indicates compound I formation, made visible due to the high H_2O_2 excess. Lower H_2O_2 concentration (3.2-fold molar excess; 16 µM H_2O_2, 5 µM protein) slows the reaction, enabling clearer visualisation of intermediate species, particularly the fatty acid-bound state (396 nm). Spectral deconvolution by SVD highlights distinct contributions from the fatty acid-bound high-spin species (396 nm), compound II (426 nm), and resting low-spin state (417 nm).

Analysis of the fast (A→B) and slow (B→C) phases detected from the stopped-flow experiments yielded rate constants k_1 and k_2, respectively. The rate constants for the fast phase (k_1) were plotted against H_2O_2 concentration to probe the kinetic relationship between k_1 and [H_2O_2]. Examination of Figures 3.10–3.13 shows a spectral transformation from Fe(III) directly to Compound II, with no clear evidence for the accumulation of Compound I. This indicates that, although Compound I is formed, its conversion to Compound II is rapid and occurs on a timescale faster than can be resolved spectroscopically. The reaction pathway can therefore be described as:

$$Fe(III) + H_2O_2 \xrightarrow{k_1} Cpd\ I \xrightarrow{k_2} Cpd\ II$$

Scheme 3.1. $OleT_{JE}$ heme Fe(III) to Compound II

Under the experimental conditions, where H_2O_2 is present in excess, the fast phase (k_1) represents the observed rate constant (k_{obs}) for the formation of Compound II. As Compound I does not accumulate, k_1 reflects the second-order reaction between Fe(III) and H_2O_2 under pseudo-first-order conditions, such that $k_1 = k_{obs} \approx k[H_2O_2]$ at low peroxide concentrations.

The dependence of k_1 on [H_2O_2] (Figure 3.14) shows an initial linear relationship, consistent with this pseudo-first-order behaviour, followed by curvature at higher concentrations. This deviation from linearity reflects an approach to a limiting rate, governed by the rapid conversion of Compound I to Compound II. At elevated H_2O_2 concentrations, the reaction becomes sufficiently fast that a significant proportion occurs within the stopped-flow dead time, contributing to the observed curvature.

Accordingly, only the initial linear region at low [H_2O_2], where the reaction remains within the measurable time window of the instrument, was used for linear regression analysis. The slope of this region provides the second-order rate constant for the reaction between Fe(III) and H_2O_2, with the values obtained summarised in Table 3.2. The slower phase (k_2) corresponds to the subsequent decay of Compound II back to the ferric resting state.

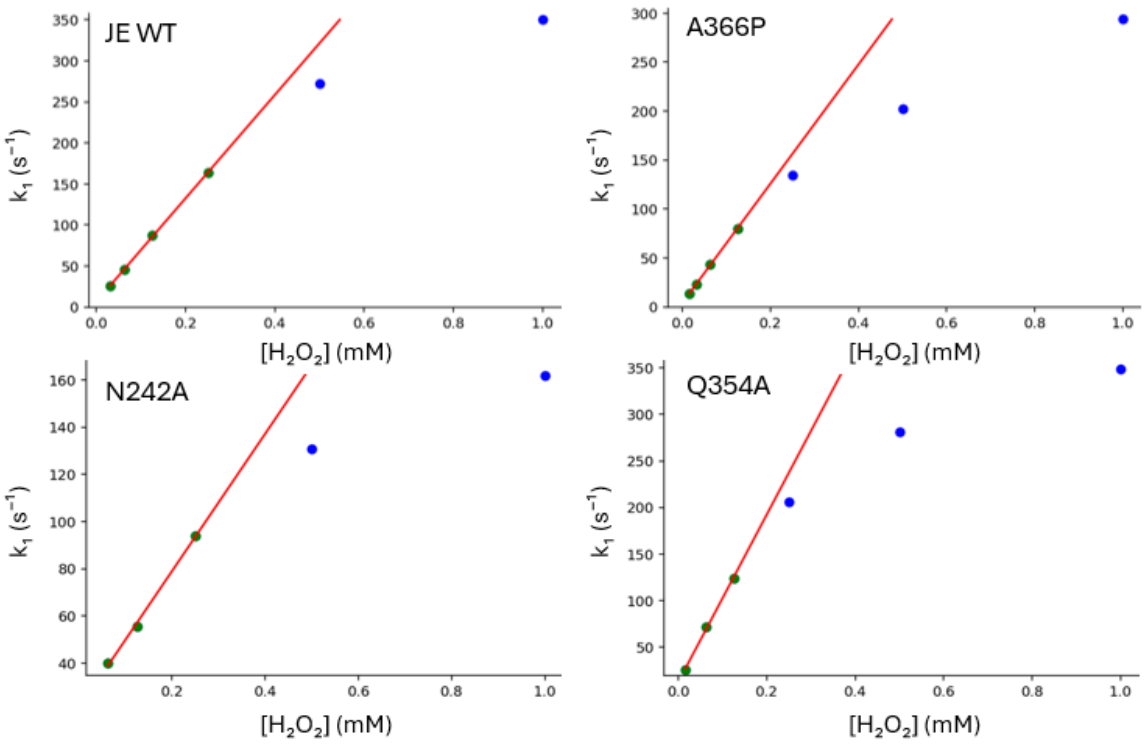

FIGURE 3.14. Single exponential fits through the linear relationship between low H_2O_2 concentration k_1 values from WT and respective variants. The blue and green datapoints represent the high and low concentration k_1 values obtained from global analysis of stopped flow spectra, respectively (Fig. 3.10-3.13). The red fit represents the linear relationship between low concentration k_1 values, with the gradient of the line being the second-order rate constant of the respective proteins.

TABLE 3.2. Second-order rate constants obtained from the linear relationship of low concentration k_1 points for $OleT_{JE}$ wild-type and variants. The second-order rate constants were excised using global analysis of spectral changes upon mixing protein with H_2O_2 in a stopped flow spectrophotometer at 10 °C and pH 7.5.

OleT variant	*Second-order rate constant (M^{-1} s^{-1})*
JE WT	$6.29 \times 10^5 \pm 7.24$
A366P	$6.09 \times 10^5 \pm 8.47$
N242A	$2.91 \times 10^5 \pm 13.38$
Q354A	$8.97 \times 10^5 \pm 40.6$

Analysis of the stopped-flow kinetics revealed that the fast phase (k_1) corresponds to the bimolecular reaction between the Fe(III) resting state of $OleT_{JE}$ and H_2O_2, yielding Compound I. The k_1 values indicate initial H_2O_2 additions are largely unaffected by A366P, significantly reduced in N242A, and moderately enhanced in Q354A. Collectively, the data demonstrate that while the Fe(III) to Compound II conversion proceeds via a kinetically competent Compound I intermediate, the efficiency of the initiating Fe(III)–H_2O_2 interaction is sensitive to specific active-site mutations.

Compound I decay to Compound II

At low H_2O_2 concentrations, no evidence for Compound I could be detected during the stopped-flow measurements, with the spectral transition appearing to proceed directly from Fe(III) to Compound II. Under conditions of 200-fold excess H_2O_2, however, a weak and broad absorbance feature at ~700 nm emerged during the fast phase, consistent with the transient

formation of Compound I and its subsequent decay to Compound II. At these high H_2O_2 concentrations, the enzyme sample is effectively saturated, allowing maximal visualisation of the Compound I decay process (Fig. 3.18). Global spectral fitting under these conditions also revealed Compound I–like contributions within the initial phases of the reaction (Fig. 3.10–3.13). Complementary high time-resolution measurements using a photomultiplier tube (PMT) further confirmed these transient features, thereby supporting the assignment of the fast phase (k_1) to the sequential conversion of Fe(III) + H_2O_2 → Compound I → Compound II (Fig. 3.18). At low H_2O_2 concentrations, Compound I is too short-lived to be detected, and the observed spectral change therefore reflects only the Fe(III) to Compound II transition. In contrast, the slow phase (k_2) corresponds to the subsequent decay of Compound II back to ferric heme. Since the fast phase involves an intermediate step, the reaction is analysed under pseudo-first-order conditions, with the derived second-order rate constants reporting on the initial Fe(III)–H_2O_2 interaction that gives rise to Compound I and its rapid decay to Compound II.

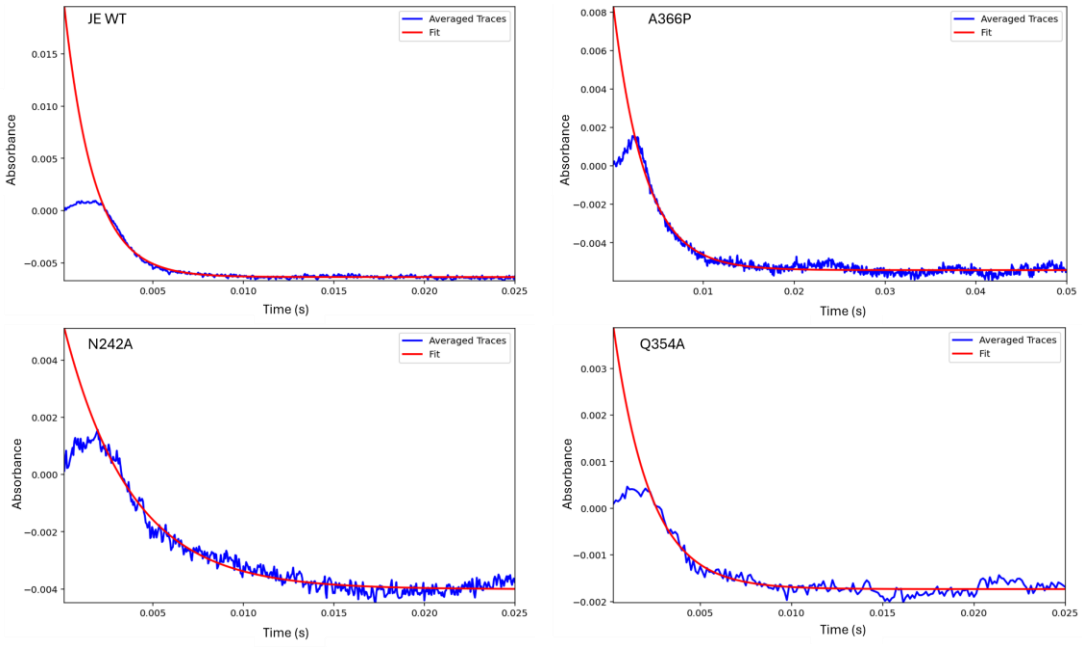

FIGURE 3.18. Averages time courses at 700 nm for WT OleT$_{JE}$ and variants. The traces for WT OleT$_{JE}$ (top left), A366P (top right), N242A (bottom left), and Q354A (bottom right) were obtained after mixing the protein with 1 mM of H_2O_2 at 10 °C and pH 7.5. The averaged traces are in blue with a single exponential fit applied in red. This fit is extrapolated back due to the dead time of ~ 2 ms at the beginning of the experiment.

The corresponding Compound I decay rate constants determined from these experiments are summarised in Table 3.3.

TABLE 3.3 Compound I decay rate constants at 700 nm for $OleT_{JE}$ wild-type and variants. The decay rate constants were excised from spectral changes upon mixing protein with H_2O_2 in a stopped flow spectrophotometer at 10 °C and pH 7.5.

OleT variant	*Compound I decay rates (s^{-1})*
JE WT	616 ± 7.4
A366P	287 ±2.9
N242A	271 ±5.2
Q354A	498 ±20

The measured Compound I decay rates highlight distinct effects of the $OleT_{JE}$ variants on the stability of this reactive intermediate. The WT $OleT_{JE}$ displayed the fastest decay rate (616 ± 7.4 s^{-1}), indicating rapid conversion of Compound I to Compound II. Both A366P (287 ± 2.9 s^{-1}) and N242A (271 ± 5.2 s^{-1}) exhibited markedly slower decay rates, suggesting that these substitutions stabilise Compound I and slow its progression to Compound II. In contrast, Q354A (498 ± 20 s^{-1}) retained a relatively high decay rate, only moderately reduced compared to wild type. Together, these data demonstrate that mutations at positions 242 and 366 significantly alter the population of Compound I, whereas the Q354A variant has a more modest impact on the decay kinetics.

For the reaction of Compound II to ferric resting state (B→C) the rates have no dependence on hydrogen peroxide concentration. With this in mind, all rates recorded were averaged and compared to the decay of Compound I, to represent the difference between them.

TABLE 3.4 Compound II to ferric rates compared to Compound I decay rates from Table 3.3. All Compound II to ferric rates were measured under the same conditions as the k_1 rates of 10 °C and pH 7.5. For the difference between rates, the values represent how many times faster Compound I decays, compared to Compound II.

OleT variant	*Compound I decay rates (s^{-1})*	*Compound II decay rates (s^{-1})*	*Difference between rates*
JE WT	616 ± 7.4	12.5	~49
A366P	287 ± 2.9	8.26	~35
N242A	271 ± 5.2	30.2	~9
Q354A	498 ± 20	9.3	~54

As evident by of how many times greater the decay of Compound I is compared to Compound II (Table 3.4), it can be suggested that this is the slow phase of the reaction. Although no dependence on hydrogen peroxide is observed, dependence on Compound I formation is evident. This helps to rationalise the differences observed between WT and variants, as for variants that employ a reduced rate of Compound I decay also employ a reduced rate of Compound II to ferric decay as Compound II formation is dependent on formation of Compound I.

Temperature dependence and van't Hoff plot for WT OleT$_{JE}$

In addition to stopped-flow and titration experiments performed on the WT and its variants, spin state equilibrium (K_{spin}) and its temperature dependence can be examined using Van't Hoff plots. Due to project time constraints, these experiments were carried out only with WT OleT$_{JE}$. However, the resulting data establish a reference framework and provide a basis for future comparative studies with the variants.

Electronic absorbance was measured over a high to low temperature range using a stopped-flow spectrophotometer to observe changes in the high- and low-spin equilibrium within the WT protein (Fig. 3.19). Both spectra in Figure 3.19 show that at 20°C both high and low spin are in equilibrium and that the equilibrium is reversible upon return to a high temperature. The spectra on the left shows that as temperature decreases from 20°C to 7°C, the equilibrium shifts toward the low-spin state, meaning that the low-spin state is enthalpically stabilised relative to the high-spin state, while the high-spin state is entropically favoured at higher temperature.

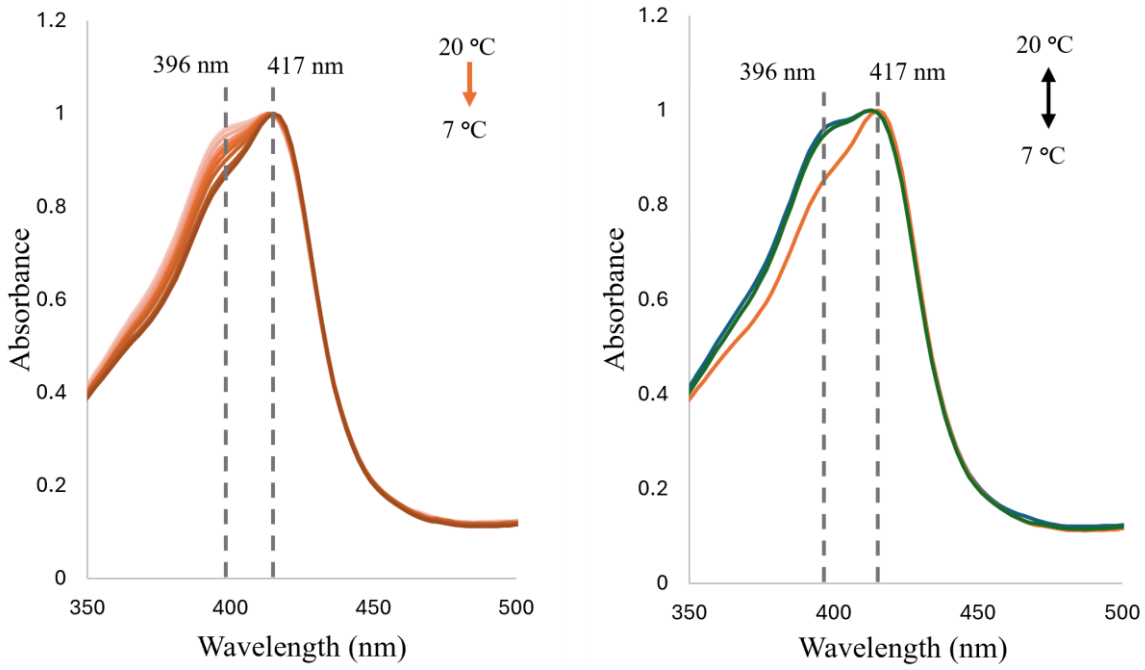

FIGURE 3.19. UV/Vis absorbance of peroxide treated OleT$_{JE}$ measured at decreasing temperatures over time (left) and the same UV/Vis spectra used to illustrate that the effect on high and low spin states by temperature is reversible. The left most spectra was obtained by measuring absorbance changes in the Soret region as a function of temperature, between 20 – 7 °C (light orange to dark orange). The grey dotted lines indicate absorbance peaks of interest, being 396 nm which corresponds to the high spin state, and 417 nm which corresponds to the low spin state. To show that the equilibrium is reversible, the right most spectra was obtained by returning to 20 °C (green) after reaching the lowest temperature, 7 °C (orange).

The van't Hoff analysis was performed by plotting lnK against 1/T (Fig. 3.20). The data showed a linear relationship, consistent with the van't Hoff equation. From the slope ($-\Delta H/R$) and intercept ($\Delta S/R$) of the fitted line, values of $\Delta H = 7.7$ kJ·mol^{-1} and $\Delta S = 28.0$ J·mol^{-1}·K^{-1} were obtained. These thermodynamic parameters indicate that the high-spin state is enthalpically disfavoured but entropically favoured. At 293K, the derived Gibbs free energy ($\Delta G = -0.46$ kJ·mol^{-1}) corresponds to an equilibrium constant of $K = 1.21$, indicating that both spin states are populated (55% HS, 45% LS; Table 3.4). This shows that the equilibrium lies slightly toward the entropy-favoured HS state, with the population distribution estimated as ~55% HS and ~45% LS. The small magnitude of ΔG demonstrates that the two states are nearly isoenergetic at room temperature, resulting in appreciable coexistence of both spin states.

These results are consistent with the expected thermodynamic behaviour of spin-crossover complexes: the HS state is enthalpically disfavoured (ΔH > 0) but entropically favoured (ΔS > 0), and its population increases with temperature above T½ (Linares, J et al., 2012)

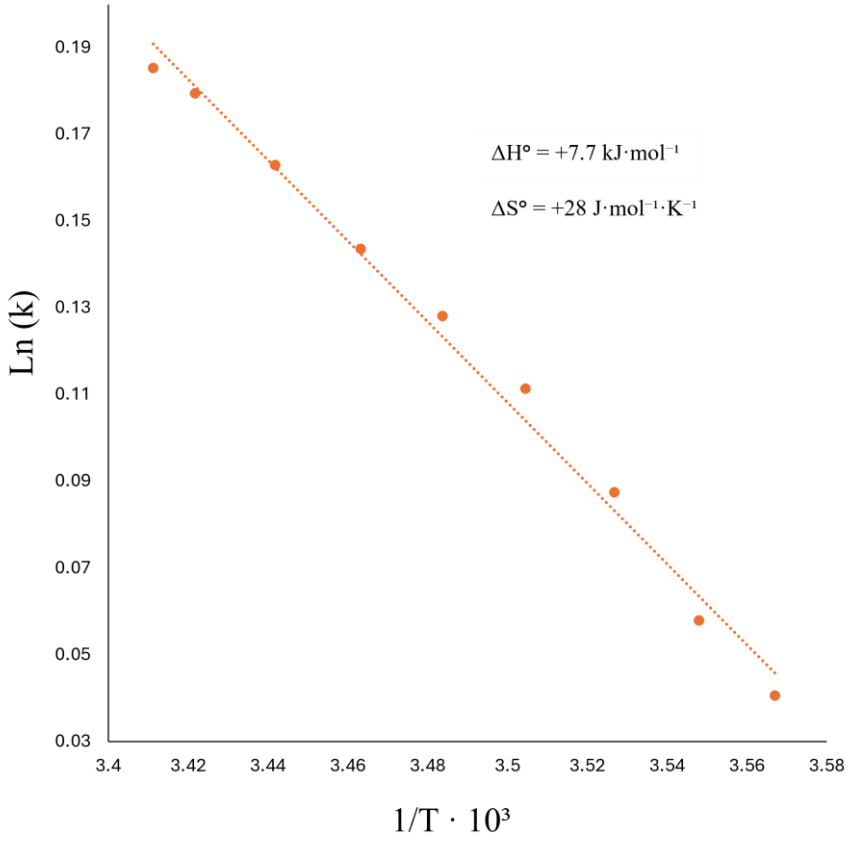

FIGURE 3.20. van 't Hoff plot of the spin-state equilibrium in OleT$_{JE}$. The natural logarithm of the equilibrium constant, lnK=ln([HS]/[LS]), is plotted against the reciprocal of temperature (1/T). Data points (red circles) were obtained from absorbance measurements at 396 nm (HS) and 417 nm (LS). The solid red

The positive ΔH° indicates that the high-spin state is enthalpically disfavoured, while the positive ΔS° shows it is entropically favoured, consistent with a shift toward the low-spin state at lower temperatures and toward the high-spin state at higher temperatures.

Using the determined ΔH° and ΔS° values determined by the van't Hoff plot gradient, ΔG (Gibbs free energy) and K_{spin} can be determined using the previously mentioned equations (experimental). These values are expressed in Table 3.5.

TABLE 3.5. Thermodynamic values calculated from the temperature dependence of $OleT_{JE}$. The thermodynamic parameters were excised using a stopped flow spectrophotometer at a temperature range of 20 – 7 °C and at pH 7.5.

OleT variant	ΔH°	ΔS°	ΔG	K_{spin}
JE WT	+7.7 kJ·mol^{-1}	+28 J·mol^{-1}·K^{-1}	–0.46 kJ·mol^{-1}	1.21

A van't Hoff analysis of the OleT variant revealed a linear lnK vs. 1/T relationship, consistent with the van't Hoff equation. From the slope and intercept, thermodynamic parameters were obtained: $\Delta H^\circ = +7.7$ kJ·mol^{-1} and $\Delta S^\circ = +28$ J·mol^{-1}·K^{-1}. At 293 K, the calculated Gibbs free energy is $\Delta G = –0.46$ kJ·mol^{-1}, corresponding to an equilibrium constant of K = 1.21. This yields a population distribution of approximately 55% HS and 45% LS, showing that both spin states coexist near room temperature. The small magnitude of ΔG demonstrates that the HS and LS states are nearly at equilibrium, consistent with the characteristic behaviour of spin-crossover complexes, where the HS population increases with temperature above T½. This description aligns well with the thermodynamics of SCO systems, where a modest ΔG leads to both HS and LS populations near the crossover temperature (Linares, J et al., 2012).

3.4 Discussion

Electronic absorbance spectroscopy

The UV/Vis spectra of each fatty acid co-purified variant of $OleT_{JE}$ shows distinct differences between them. When comparing the A366P variant to WT, A366P favours the high-spin state relative to WT. The same observation is made in a previously published PhD thesis regarding the A369P variant of $OleT_{SA}$ (Amaya, J.A., 2018). The same can be said for Q354A although, as seen from the spectra, the ratio of absorbance from the Soret region (396 nm and 417 nm) and aromatic absorbance region (280 nm) shows a distinct reduction when compared to WT and other variants. $OleT_{JE}$ is a monomeric species, so heme and protein concentration should be 1:1. This distinct difference is most likely a result of the mutation, as glutamine is able to form side chain and backbone hydrogen bonds with surrounding residues (such as Cys365) on the proximal side of the heme prosthetic group due to glutamines polarity. Alanine however removes this ability to form side chain hydrogen bonds with surrounding residues due to the lack of a polar side chain. This distinct difference between the aromatic and Soret absorbance regions for Q354A could be a result of the loss of hydrogen bonds causing destabilisation of the heme prosthetic group, lowering occupancy; altering heme orientation causing the heme to be misaligned, affecting function, or could affect insertion kinetics of the heme during expression thus potentially increasing the time required for guiding heme into the pocket.

On inspection of N242A, the high-spin heme character is of similar molar extinction as the WT, indicating no higher preference for the high-spin state as seen in the A366P and Q354A variants. Furthermore, after the addition of 5-10 molar excess of H_2O_2, each protein turns over the co-purified lipid and returns to resting state with a λ_{max} of 417 nm. This shows that regardless of the variants employed for each protein, they remain catalytically active.

On the topic of the Fe(II)-CO spectra, both A366P and Q354A express higher absorbance at 450 nm and lower absorbance at 420 nm regions when compared to the WT. This change

suggests the proximal Cys ligand that coordinates the heme has more of a thiolate character when compared to WT. A similar behaviour is observed for mutant A369P in $OleT_{SA}$, although the ratio of the split 420-450 nm Soret region in A369P favours even more so that of the 450 nm thiolate character than compared to A366P of $OleT_{JE}$ (Amaya, J.A., 2018). When compared with one-another, the 420 nm characteristic within A366P is more diminished than seen in Q354A suggesting a greater presence of the deprotonated thiolate character. Together these findings suggest that the proximal variants, comparatively, have affected the protonation of the axial cysteine (thiol or thiolate) as a consequence of removing hydrogen bonding capacity. The N242A variant expresses the opposite, having a markedly higher absorbance at 420 nm and a significantly reduced absorbance at 450 nm than the WT, suggesting a higher presence of heme Cys thiol character. The same variant characteristics observed for the as-purified Fe(II)-CO complex are observed in the H_2O_2 treated Fe(II)-CO complex (Fig. 3.4), although upon dithionite addition, transition from 417 nm to 406 nm appears not to occur. Regardless, the Fe(II)-CO complex still forms after the addition of CO (Fig. 3.4).

Fatty acid titrations

For titrations of C20:0, C18:0 and C12:0, there are distinct differences between variants and WT. WT expressed a dissociation constant (K_d) of 0.33 μM, 0.96 μM and 1.13 μM, respectively. These K_d values suggest that the protein binds more tightly to longer saturated alkyl chain fatty acids, with the highest affinity for C20:0 (K_d = 0.33 μM) and progressively lower affinities for C18:0 (0.96 μM) and C12:0 (1.13 μM). This trend indicates a preference of the WT protein for longer acyl chains, likely reflecting optimal interactions within the binding pocket that accommodate longer hydrophobic chains more effectively.

A366P expresses K_d values of 0.16 μM, 0.17 μM, and 0.46 μM for fatty acids C20:0, C18:0 and C12:0, respectively. Compared to WT, the A366P variant exhibits tighter binding to all

tested fatty acids and a reduced preference for longer chains, indicating that this mutation enhances overall affinity while flattening the chain-length specificity profile. These changes in binding affinity may result from the proline causing a loss of backbone hydrogen bonding to the axially coordinated cysteine thiolate, potentially altering the electronic environment, redox potential, σ-electron donation from the thiolate, or even O–O bond activation. In a previous study (Yoshioka, S et al., 2002) the mutation Q360P was studied in a P450cam to investigate the role of hydrogen bond networks surrounding the heme-thiolate centre. The study raises areas of interest, in particular, prolines inability to form backbone hydrogen bonds. Alanine contains a backbone amide hydrogen (NH) which can participate in hydrogen bonds. Proline on the other hand is a cyclic amino acid with its side chain bonded back to the nitrogen of the backbone amide. This forms a secondary amine (NH), meaning proline is unable to form backbone hydrogen bonds due to the lack of the backbone amide hydrogen (NH). Proline also introduces rigidity which can have downstream structural effects. The study states that Q360P removes side chain hydrogen bonds and electrostatic interactions between Q360 and surrounding residues such as the axial Cys357 sulphur atom. A366P may remove similar backbone or side-chain hydrogen bonds to the axial Cys ligand, altering the local electrostatic environment with potential downstream mechanistic effects such as the observed K_d values for respective substrates. Furthermore, electrochemical experiments supported that Q360P increased electron donation to the axial thiolate due to negative shifts in the redox potential by 70 mV. This suggests that A366P should increase σ-electron donation from the thiolate and demonstrate that removal of hydrogen bonding around the axial cysteine (via Pro mutation) alters the redox potential which could be relevant to Compound I lifetime and reactivity. Furthermore, the Q360P study suggests that π-electron donation, not the σ-electron donation, of the thiolate ligand promotes O-O bond activation. This suggests that while increased σ-

donation (as caused by proline) may not directly promote oxygen activation, it could potentially modify the electronic landscape of the heme in a meaningful way (Yoshioka, S et al., 2002)

Q354A expresses K_d values of 0.064 μM, 0.004 μM, and 2.18 μM for C20:0, C18:0, and C12:0, respectively. Compared to WT, this variant shows dramatically tighter binding for longer saturated alkyl chain fatty acids (C20:0 and C18:0) but weaker binding to the shorter chain (C12:0). Because the mutation is on the proximal side of the heme, these changes are likely due to altered properties of the cysteine thiolate ligand, such as its electron density, σ-donation, or redox potential, which in turn modulate binding affinity for longer-chain fatty acids. The aforementioned study (Yoshioka, S et al., 2002) can be applicable for this mutation as well due to alanine's removal of the side chain hydrogen bond from the glutamine to the Cys365.

N242A gives K_d values of 0.12 μM, 0.2 μM, and 0.56 μM for C20:0, C18:0, and C12:0, respectively. This mutation is located on the distal side of the heme, and the WT Asn forms a hydrogen bond with Arg245, which is important for substrate interaction. As reported in Chapter 4, the N242A mutation disrupts this hydrogen bond, leading to an alternate conformation of Arg245, leading it to 'swing' out of its usual conformation to aid with substrate positioning. This conformational shift likely reduces the precision of substrate coordination, which is reflected in the moderately altered K_d values across fatty acid chain lengths, with slightly reduced binding affinity compared to WT.

Together, the K_d measurements highlight how specific mutations on the proximal or distal sides of the heme can modulate binding affinity, chain-length specificity, and substrate coordination through distinct structural mechanisms, whether by altering thiolate properties, hydrogen-bonding networks, or local backbone rigidity. Having established these effects on binding, we next turned to stopped-flow experiments to investigate how these mutations influence the kinetics of catalytic turnover and stability of reactive intermediates.

To note, the titration experiments monitor the shift between low-spin (417 nm) and high-spin (396 nm) heme states as fatty acids bind. The observed differences in K_d values and saturation behaviour across variants could therefore also reflect alterations in the low-/high-spin equilibrium rather than binding affinity alone. For example, mutations on the proximal side (Q354A, A366P) may modulate the electronic properties of the cysteine thiolate, influencing the stability of the high-spin state, while the distal-side mutation (N242A) may affect spin equilibrium indirectly through perturbation of the Arg245 hydrogen-bonding network. While UV/Vis provides indirect evidence for such spin-state changes, definitive confirmation would require EPR spectroscopy to quantify spin populations and assess whether the mutations bias the equilibrium toward high- or low-spin states.

Stopped-flow kinetics

Stopped-flow spectroscopy provided mechanistic insight into how $OleT_{JE}$ variants influence peroxide-driven catalysis. In WT, rapid mixing with H_2O_2 revealed the expected sequential transition from the fatty acid bound, high-spin Fe(III) state (396 nm), through Compound I and Compound II intermediates (~700 nm and 426 nm, respectively), before relaxing into the low spin resting state (417 nm). The extracted second-order rate constant ($k_1 = 6.29 \times 10^5$ M^{-1} s^{-1}) and Compound I decay rate (616 s^{-1}) confirm the enzyme's ability to efficiently activate peroxide and progress through the catalytic cycle under the conditions tested.

The A366P variant displayed kinetics similar to WT, but with a markedly slower Compound I decay rate (287 s^{-1}). Despite only a minor reduction in the second-order rate constant ($k_1 = 6.09 \times 10^5$ M^{-1} s^{-1}), the extended lifetime of Compound I suggests stabilisation of the ferryl-oxo species. It can be said, with confidence, that the removal of the hydrogen bond interaction between A366 and Cys365 via the introduction of proline has extended the lifetime of Compound I. As shown in Figures 3.3 and 3.4, this hydrogen bond removal affects the ability

of the thiolate to be protonated, and the absence of this protonation further stabilises the ferryl-oxo intermediate, prolonging its lifetime.

In contrast, Q354A exhibited a higher second-order rate constant (k_1 = 8.97 × 10^5 M^{-1} s^{-1}), indicating faster H_2O_2 binding than WT. Its Compound I decay rate (498 s^{-1}), however, remained slower than WT, suggesting a significant modulation of the catalytic cycle. This can be attributed to the removal of the hydrogen bond between Q354 and Cys365, which subtly alters the electron donation from the thiolate to the heme iron, as seen in Figures 3.3 and 3.4. As a result, the high-valent Compound I intermediate is modestly stabilised, prolonging its lifetime relative to WT. This behaviour underscores the critical role of the proximal glutamine in fine-tuning thiolate protonation and balancing the rates of intermediate formation and decay during catalysis.

The N242A variant, located on the distal side of the heme, showed the most pronounced perturbations, with both the second-order rate constant (2.91 × 10^5 M^{-1} s^{-1}) and Compound I decay rate (271 s^{-1}) reduced relative to WT. These effects can be rationalised by disruption of the Asn242–Arg245 hydrogen bond, influencing substrate binding and turnover. The loss of this interaction likely destabilises substrate positioning and reduces the efficiency of both H_2O_2 binding and subsequent intermediate turnover, consistent with the altered binding affinity observed in equilibrium titrations.

Overall, these results reveal distinct mechanistic consequences of proximal versus distal mutations. Proximal-side variants (A366P, Q354A) predominantly affect the electronic properties of the cysteine thiolate, thereby modulating rates of H_2O_2 binding and high-valent intermediate stabilisation. By contrast, the distal-side mutation N242A disrupts the hydrogen-bonding network required for efficient substrate alignment, diminishing catalytic efficiency. Together, these findings underscore the delicate relationship between heme electronic

structure, hydrogen bonding, and substrate positioning in controlling the kinetics of $OleT_{JE}$ catalysis.

Van't Hoff plot

The extracted thermodynamic parameters ($\Delta H° = +7.7$ kJ·mol^{-1}, $\Delta S° = +28$ J·mol^{-1}·K^{-1}) are consistent with a spin crossover equilibrium in which the low-spin state is enthalpically stabilised, while the high-spin state is entropically favoured. Consequently, as temperature decreases, the equilibrium shifts toward the low-spin state, in agreement with Le Châtelier's principle. It can be concluded that this experiment gives a viable framework for future work in this area to further elucidate the spin state equilibrium within each variant, and how they could have altered it.

3.5 Conclusion

This chapter has examined the insights gained from the spectroscopic, kinetic, and thermodynamic characterisation of WT $OleT_{JE}$ and the targeted variants developed in this study. Each variant provided evidence that its respective residues influenced the heme environment, as reflected in changes to K_d values, second-order rate constants, and Compound I to Compound II decay rates. It can be said, with confidence, that the lifetime of Compound I has been affected by these mutations either by directly affecting interactions with the axial cysteine thiolate (A366P and Q354A) or indirectly by altering H_2O_2 binding efficiency (N242A). While further investigation is warranted, these results lay the groundwork for macromolecular crystallography studies to more precisely elucidate the structural effects of the targeted variants on $OleT_{JE}$.

Chapter 4

X-ray Crystallography studies

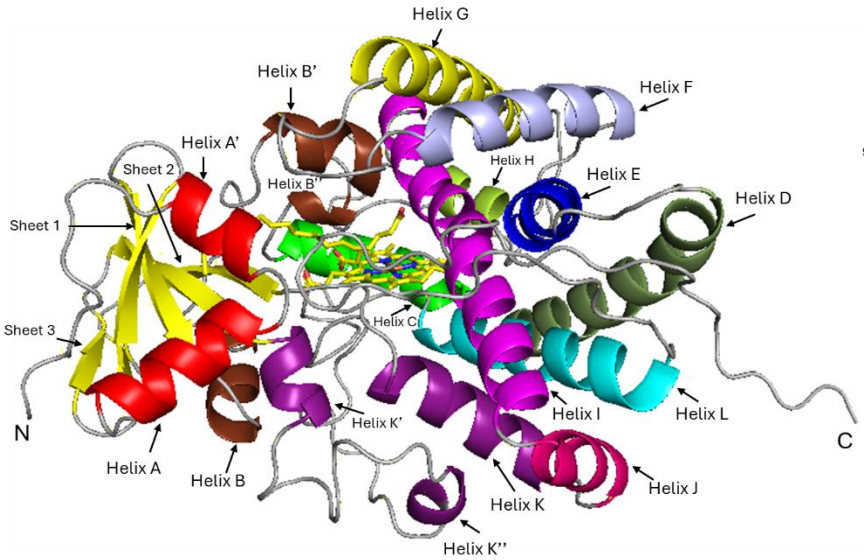

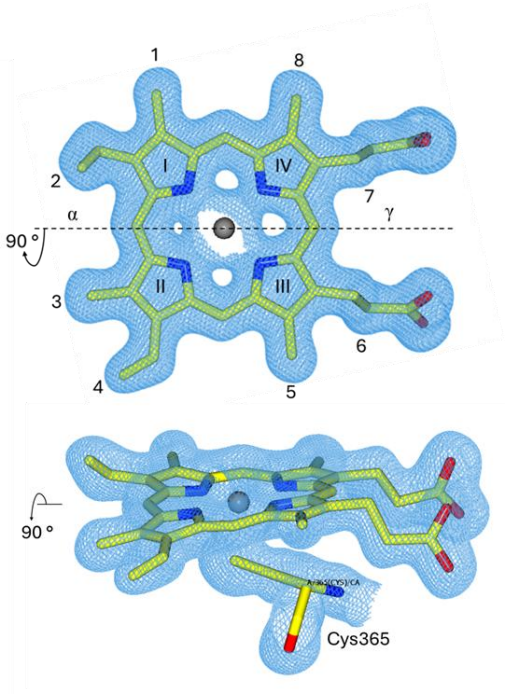

4.1 Introduction

In the preceding chapters, the spectroscopic, thermodynamic, and kinetic characteristics of the $OleT_{JE}$ wild-type (WT) and variants have been investigated. These studies provided a comprehensive insight into how individual substitutions influenced protein function, offering clues regarding potential alterations to the catalytic mechanism and overall stability and heme uptake of the protein. While such data yield important insights, structural changes remain unknown. A direct assessment at the atomic level was therefore necessary to establish how site-directed mutagenesis correlates with alterations to protein architecture and influence of fatty acid binding modes.

X-ray crystallography remains one of the most powerful techniques for visualising protein structures at atomic resolution. By enabling the determination of atomic coordinates, crystallography allows for structural comparisons between WT and variants, highlighting conformational shifts, altered interactions, or local rearrangements that may account for observed differences in biochemical behaviour. The application of this method to $OleT_{JE}$ is warranted, as the catalytic activity is thought to arise from functionally significant structural features within its active site and surrounding regions, as discussed in Chapter 1.

This chapter will describe in detail the methodologies used to produce crystals of the $OleT_{JE}$ variants, alongside the procedures followed for diffraction data collection at Diamond Light Source (DLS). The subsequent stages of data processing and refinement will also be outlined. Finally, the resulting structures will be compared with that of the published X-ray structure of WT $OleT_{JE}$ (Belcher, J et al., 2014; PDB: 4L40), allowing any variant-associated changes to be visualised and corroborated in the context of the biochemical findings presented earlier.

4L40 PDB file analysis

To briefly recapture the analysis on the 4L40 structure in Chapter 1, hydrogen bond interactions between key residues and the selected residues which were changed in this study are shown in Figure 4.1.

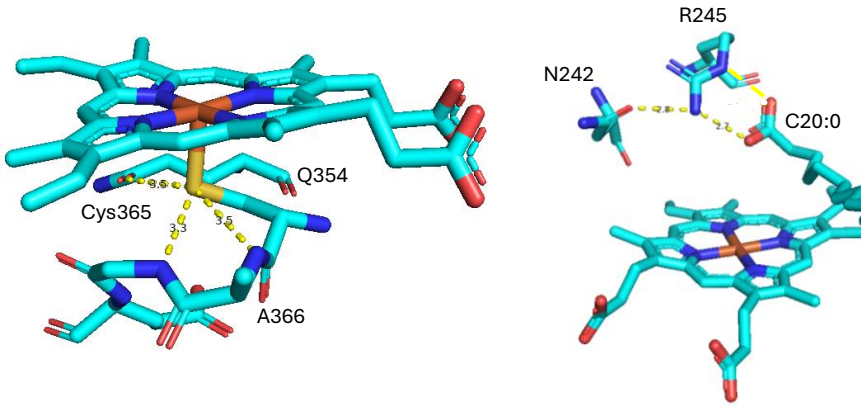

FIGURE 4.1. Proximal (left) and axial (right) hydrogen bond interactions between respective residues found in wild-type OleT$_{JE}$ (PDB 4L40). Possible interactions are represented by yellow dashed lines.

On the distal side of the heme, the side chain O atom of residue N242 was identified to participate in a N–H···O hydrogen bond with residue R245 side chain secondary amide. R245's side chain N_H and N_e forms hydrogen bonds with the carboxyl O groups of the bound fatty acid substrate in order to position it close to the heme iron centre for hydrogen atom abstraction from the Cβ position, ultimately leading to alkene product formation (Grant, J et al., 2015). Breaking this interaction was hypothesised to have mechanistic and catalytic consequences, which has been proven through the analysis reported in Chapter 3.

In parallel, residues A366 and Q354, found on the proximal heme side, have been identified to contribute backbone amide hydrogen bond interactions with the sulphur of the axially coordinated cysteine thiolate residue (Fig. 4.1). Given the coordinating Cys residues importance in maintaining the heme iron centres spin state, disrupting these polar interactions at the aforementioned positions could have meaningful consequences, as highlighted from results in Chapter 3.

4.2 Experimental Procedure

Screening for crystallisation conditions

Crystallographic screening was performed using an ARI Crystal Gryphon Protein Crystallisation Pipettor (Art Robbins Instruments) and set up in MRC 96-well 2-drop crystallisation plates (Molecular Dimensions). Initial trials employed a range of commercially available crystallisation screens, including JCSG-plus, Morpheus, Structure Screen 1 and 2, and PACT premier (all from Molecular Dimensions). As purified fatty acid bound protein samples were tested at two concentrations (20 mg/mL and 40 mg/mL), and drops were set up using condition-to-protein ratios of 1:1 and 2:1 with volumes of 0.2 and 0.4 µL. Crystallisation plates were incubated 18°C and regularly inspected using an optical microscope to identify potential crystallisation hits. Promising conditions were subsequently optimised through alterations such as changes to condition concentrations, pH, and protein-to-condition ratios. Optimisation strategies included both batch crystallisation and the hanging-drop vapour-diffusion method, to improve crystal quality and size for diffraction. Conditions with the most success included: 2.2 M ammonium sulfate, 0.1 M HEPES, pH 6.5, 2:1 (protein-to-condition); 1.8 M ammonium sulfate, 0.1 M tris, pH 7.5, 2:1 (protein-to-condition); 20% ethanol, 0.1 M tris, pH 8.5, 2:1 (protein-to-condition), for WT, and the N242A and A366P variants, respectively.

Harvesting crystals and preparing for cryogenic measurements

Once suitable crystals were obtained, they were harvested using 0.3–0.5 mm loops and transferred into cryoprotectant solutions prior to cryogenic freezing. Crystals were then mounted into DLS pucks and rapidly cryo-cooled by direct immersion in liquid nitrogen. A range of cryoprotectants were evaluated, as the choice of cryoprotectant can strongly influence diffraction quality. The conditions tested included 1.7 M sodium malonate, varying concentrations of ethylene glycol (20%, 25%, and 50%), sucrose (40% and 50%), and glycerol

(25% and 50%). Optimal cryoprotectant conditions were empirically identified during X-ray diffraction screening. Furthermore, as fatty acid bound protein was used for crystallography screening, some harvested crystals underwent soaking with H_2O_2 alongside cryoprotectant immersion for the possibility of excising conformational differences between catalytic states. Between 1 mM and 5 mM H_2O_2 (Merck) and cryoprotectant solutions were used for these soaking experiments. Selected crystals were immersed in the solutions for varying times before submerging into liquid nitrogen. DLS pucks were dry shipped in a liquid nitrogen cooled dewar before beamline scheduling.

I24 beamline operation

Diffraction experiments were carried out remotely on the I24 beamline at DLS. The X-ray beam was set to a size of 7 × 7 μm, with an energy of 20,000 eV and a flux of approximately 9.4 × 10^9 photons/s. For initial diffraction screening, data was collected with a detector resolution cut-off of 1.7 Å, using 30 images acquired with an exposure time of 0.5 s per image, an Ω oscillation of 0.5°, and 100% beam transmission. Following the identification of crystals with suitable diffraction quality, full data collection was performed using a detector resolution cut-off of 1.5 Å, with 1,800 images recorded under conditions of 0.1° Ω oscillation, 0.02 s exposure per image, and 25% beam transmission. Diffraction datasets were processed automatically through the ISPyB pipeline at DLS, which generated outputs from several processing routes, including xia2.dials and xia2.multiplex (Gildea, R.J. et al., 2022). Scaled and unmerged data from both pipelines were subsequently exported from ISPyB and used for structure determination and refinement within the CCP4i2 software (Potterton, L et al., 2018).

CCP4i2 workflow

Scaled and unmerged reflection files were imported into AIMLESS (Evans, P.R. et al., 2013) for data reduction. Indexing and integration were performed in the previously determined space

group P 6_122. Data quality statistics were assessed, including resolution range, completeness, and CC½. For the WT dataset, the structure was solved by molecular replacement using MOLREP (Lebedev, A.A. et al., 2008), with PDB entry 4L40 from study (Belcher, J. et al., 2014) as the search model. The solution was refined and subsequently used as the starting model for all variant datasets generated in this project. Following molecular replacement, refinement was carried out using REFMAC5 (Kovalevskiy, O. et al., 2018), alongside manual model building in Coot (Emsly, P. *The Coot User Manual*). Model validation was continuously monitored by examining R-work, R-free, and bond/angle RMSDs. Refinement proceeded until final models achieved values consistent with high-quality structures.

4.3 Results

From crystallography screening, crystals were obtained for the as purified N242A and A366P variants. In the interest of Q354A, attempts to screen for a condition were inherently flawed due to the variant's nature of precipitating out of solution. With this in mind, attempts to attain a structure for as purified N242A and A366P were the focus for this side of the project.

The protein samples used for crystallography were found, through spectroscopic analysis (described in detail in Chapter 3), to contain a fatty acid after purification. Consequently, the crystals inherently contained the fatty acid, without the need for additional soaking or co-crystallisation steps.

The N242A crystals grew in 1.8 M ammonium sulphate, 0.1 M Tris/HCl, pH 7.5 in v/v ratios of 1:1, 1:2 and 2:1 using a 40 mg/mL protein concentration (Fig. 4.2). The crystals were grown over a week at 18 °C with the hanging-drop method yielding plate-shaped large crystals of good quality for X-ray diffraction as seen in Figure 4.2 The dimensions of these crystals were 158.05 µm x 328.75 µm.

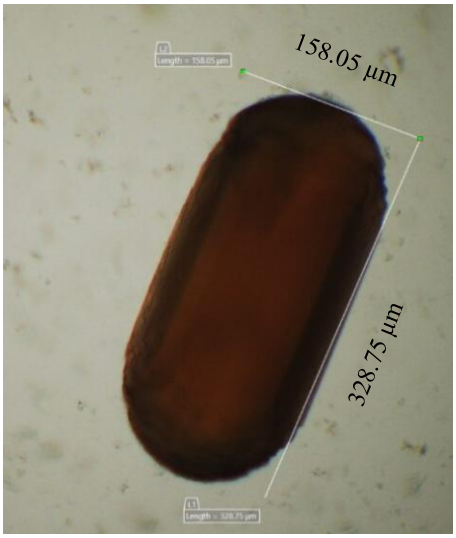

FIGURE 4.2. Hanging-drop vapour-diffusion crystallisation of N242A and dimensions of one of the N242A crystals. Crystals grew in 1.8 M ammonium sulphate, 0.1 M Tris/HCl, pH 7.5 in v/v ratios of 1:1, 1:2 and 2:1 using a 40 mg/mL protein concentration at 18 °C over a week.

In contrast to the N242A variant, the A366P variant crystallised under conditions containing ethanol and 2-propanol rather than ammonium sulphate. Initial microcrystals were observed in MRC 96-well screening plates (Fig. 4.3, left). The batch condition, that yielded macrocrystals used for synchrotron X-ray diffraction, was 20% ethanol, 0.1 M Tris/HCl, pH 8, at a v/v ratio of 2:1. The crystals were grown at 18 °C, producing plates over a week, as seen in Figure 4.3 (right). The dimensions of the macrocrystals were seen to be 42.4 µm x 173.33 µm.

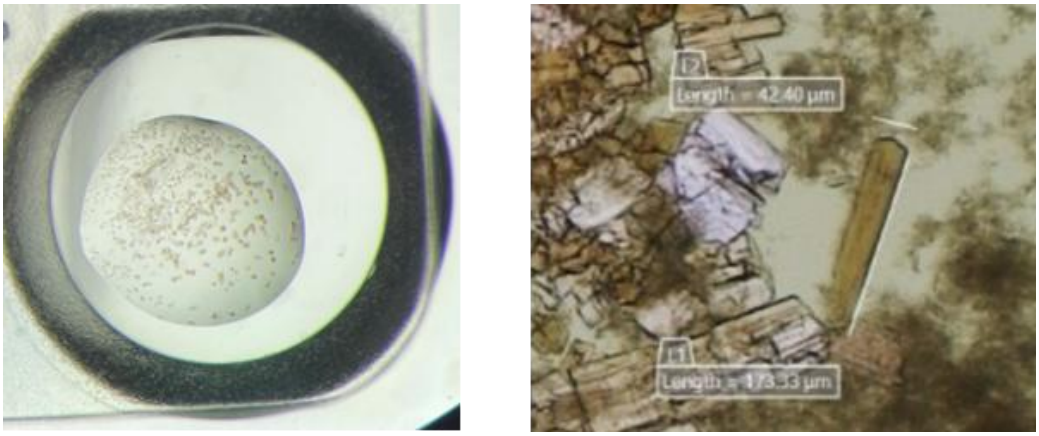

FIGURE 4.3. A366P microcrystals in an ethanol condition from an MRC 96-well 2-drop crystallisation plate (left) and macrocrystals from an A366P batch condition with dimensions (right). Crystals were grown in 20% ethanol, 0.1 M Tris/HCl, pH 8, at a v/v ratio of 2:1 at 18 °C over a week.

Table 4.1: Crystallographic processing and refinement statistics for as purified $OleT_{JE}$ and variants. Values in parenthesis are for the highest resolution shell.

	N242A	***N242A soak***	***A366P***
Crystal condition	1.8 M ammonium sulphate, 0.1 M Tris, pH 7.5, 2:1	1.8 M ammonium sulphate, 0.1 M Tris, pH 7.5, 2:1	20% ethanol, 0.1 M Tris, pH 8, 2:1
Space group	$P6_122$	$P6_122$	$P6_122$
Unit cell (Å)	a = 76.982, b = 76.982, c = 371.738, α = 90.0, β = 90.0, γ = 120.0	a = 77.078, b = 77.078, c = 373.242, α = 90.0, β = 90.0, γ = 120.0	a = 78.358, b = 78.358, c = 374.271, α = 90.0, β = 90.0, γ = 120.0
Resolution (Å)	66.67-1.68 (1.71-1.68)	58.82-1.93 (1.98-1.93)	67.86-1.87 (1.91-1.87)
Unique reflections	75997 (3810)	50965 (3301)	57662 (3606)
Multiplicity	13.6-20.4	19.6-20.3	26.7-37.1
Completeness (%)	99.9 (100.0)	99.9 (98.9)	99.8 (99.7)
Mn(I/sd)	18.2 (0.9)	18.8 (1.4)	22.2 (1.3)
R_{merge}	0.206 (3.781)	0.195 (2.544)	0.991 (1.746)
Wilson B-factor ($Å^2$)	23.46 (7.23)	31 (8.36)	18.4 (8.3)
$CC_{1/2}$	0.99 (0.47)	0.996 (0.48)	0.997 (0.976)
Reflections used in refinement	75810 (3839)	50810 (2456)	51471 (2569)
R_{work}	0.219	0.254	0.51
R_{free}	0.246	0.297	0.541
RMSD bond lengths (Å)	0.0085	0.0087	0.0073
RMSD bond angles (°)	1.9	1.982	1.809

X-ray crystallography of the N242A variant

Data collection and refinement statistics are reported in Table 4. 1. A single protein molecule was found in the crystallographic asymmetric unit and the structure was determined and refined to 1.68 Å (Table 4.1). The overall fold of the N242A variant can be seen in Figure 4.4. The crystal structure adopts the canonical cytochrome P450 fold, which is predominantly α-helical, consisting of ~12 conserved helices (A–L) surrounding the heme prosthetic group. In addition to these helices, N242A also contains several short β-sheets that stabilise the core structure. The central features of the fold include the long I-helix traversing the active site and the L-helix cysteine loop, which coordinates the heme iron via the axial cysteine ligand (Bharadwaj, V. et al., 2018).

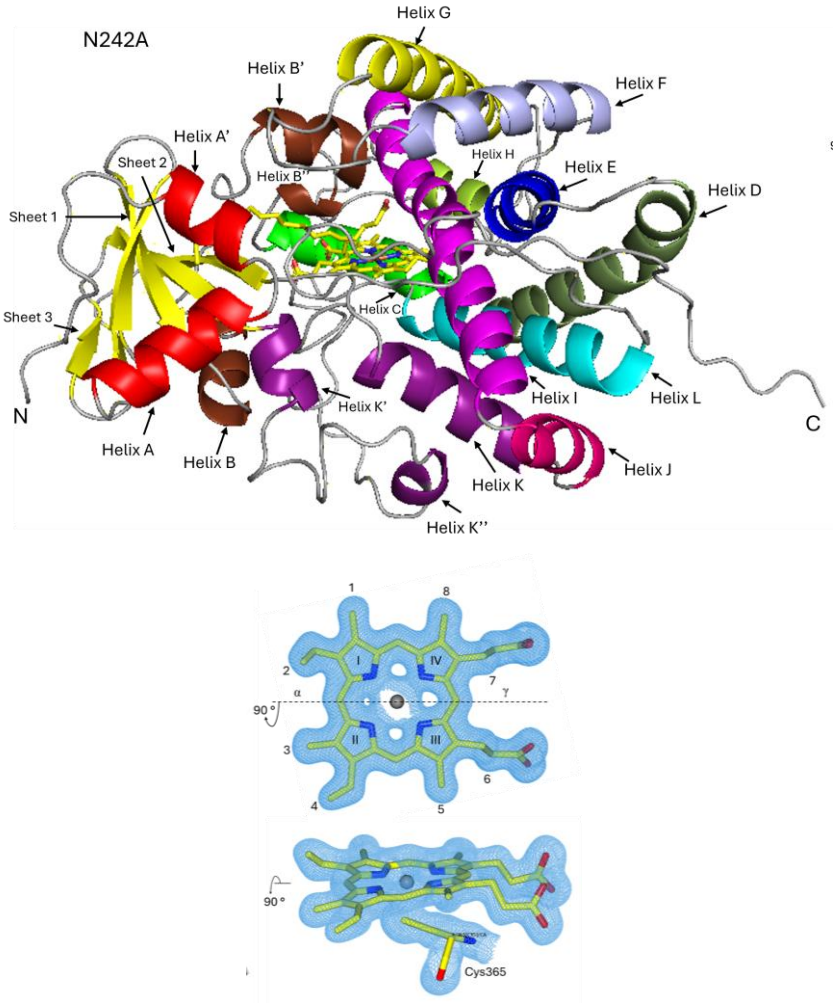

FIGURE 4.4. Cartoon crystal structure of N242A modelled with C20:0. The structure has a resolution of 1.68 Å, R-work of 0.22 and R-free of 0.25. Helices A to L, sheets 1 to 3, and both the N- and C-terminals of the N242A fold are coloured and/or labelled within the figure. The heme prosthetic group (yellow) can be seen at the centre of the full crystal structure and the corresponding $2F_o$-F_c density (blue mesh), contoured to 1σ is shown (bottom). Rotation of the heme on the C_α-C_γ axis by 90 ° better represents the axial cysteine ligand coordination.

The N242A crystal structure was superimposed with the wild-type $OleT_{JE}$ structure (PDB:4L40) to identify any changes in secondary structure (Fig 4.5). The major secondary structure difference found between both structures was within the 155-181 residue range. This area contains a flexible loop and α-helix region which had lower electron density due to the presence of flexible residues (Fig 4.6.).

FIGURE 4.5. Superimposed structures of N242A lipid bound with the 4L40 structure. Minor secondary-structure differences are observed between monomers, specifically within the flexible loop and α-helix region between residues 155 and 181.

The flexible region found between helices F and G is known as the F/G loop. Significant deviations are observed in the F/G loop region and are illustrated in Figure 4.6. This segment forms part of the fatty acid binding pocket, specifically the portion that accommodates the fatty acid alkyl tail. In $OleT_{JE}$, residue Leu177 within the F/G loop blocks the narrow solvent access channel that remains open in both P450BSβ and the related P450SPα (Belcher, J. et al., 2014).

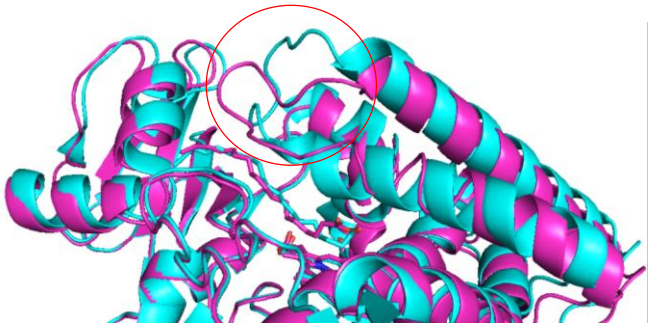

FIGURE 4.6. F/G loop region difference between N242A and 4L40 structures. The F/G loop difference between both superimposed structures is circled in red.

Examination of the N242A $2F_o$-F_c electron density map revealed that the crystal structure carried the desired mutation (Fig 4.7). Furthermore, the $2F_o$-F_c was consistent with the presence of a fatty acid chain and the presence of 2 water molecules on the distal face of the heme (Fig 4.7). The presence of 2 water molecules on the distal side of the heme contrasts with the established catalytic pathway of $OleT_{JE}$ and other P450 enzymes. Typically, substrate binding displaces the weakly bound water molecule from the hexa-coordinated heme centre, driving the system into a high-spin state necessary for Compound I formation and catalysis. The observation of water density above the heme in the fatty acid bound state suggests that contrary to canonical P450 and peroxygenase mechanisms, the heme centre may remain hexa-coordinated in its high-spin form. One possible interpretation is that substrate binding does not fully displace the water but instead weakens its interaction with the heme, resulting in an aqua high-spin species rather than the expected penta-coordinated high-spin intermediate (Conner, K.P. et al., 2014).

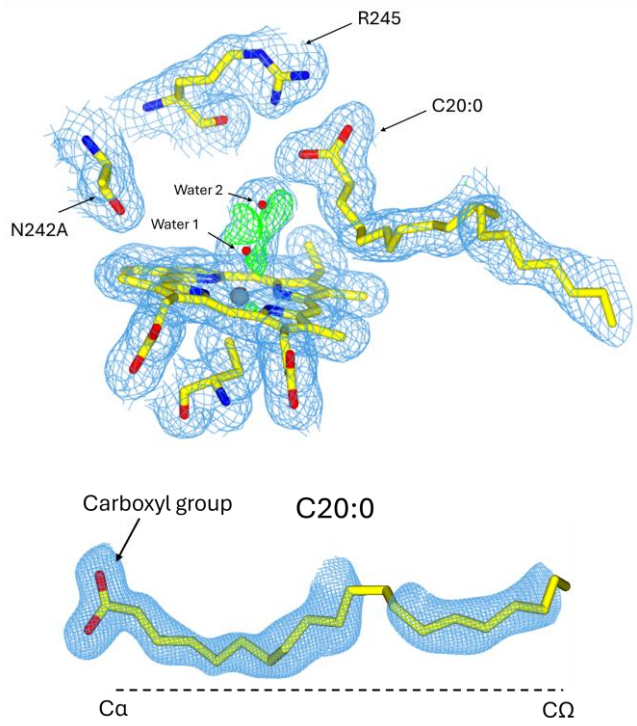

FIGURE 4.7. F_o-F_c and $2F_o$-F_c electron density maps that correspond to the N242A mutation site, R245 conformational change, and position of heme coordinating waters (top), and the fatty acid electron density (bottom).

After superimposing the N242A and 4L40 PBD crystal structures, examination of active site residues revealed that R245, R252, Y405, and F79, as well as the position of the fatty acid substrate had adopted different conformations to what is seen from the published 4L40

structure in Figure 4.1 (Fig 4.8). The slight conformation shift of R252 and F79, and the 'swung out' Y405 residue can be considered a result of these residues flexible nature. On the other hand, the conformational shift of R245 and the fatty acid substrate can be considered a result of the mutation and are better represented in Figure 4.9.

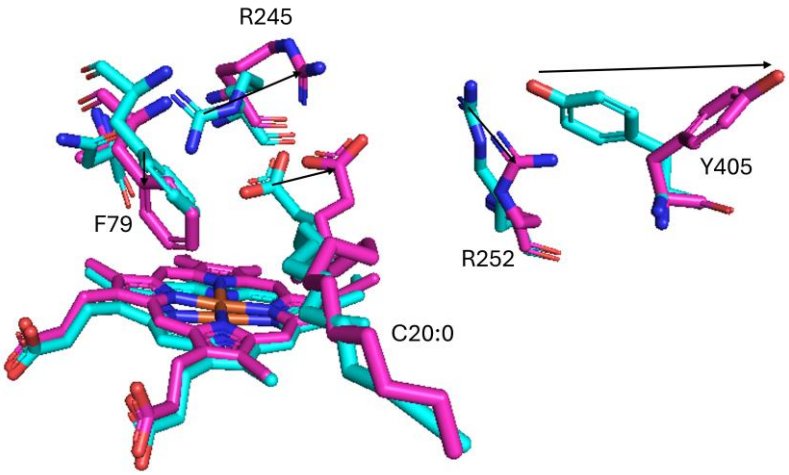

FIGURE 4.8. Active site residue differences between the N242A structure (purple) and the 4L40 structure (blue). Conformational changes are indicated by black arrows.

Moreover, the hydrogen bond interactions between the R245 side chain and the carboxyl head of the fatty acid appear to be maintained within the N242A crystal structure. These interactions are illustrated in Figure 4.9.

Both Figures 4.8 and 4.9 highlight the importance of the N242 residue. Removal of the hydrogen bond between R245 and N242 causes R245, together with the fatty acid substrate, to "swing out" of its usual position. This displacement occurs because R245 remains hydrogen-bonded to the fatty acid substrate, effectively pulling it along as it shifts. This alteration can provide rationale for the altered spectroscopic, kinetic and thermodynamic values compared to WT seen in Chapter 3.

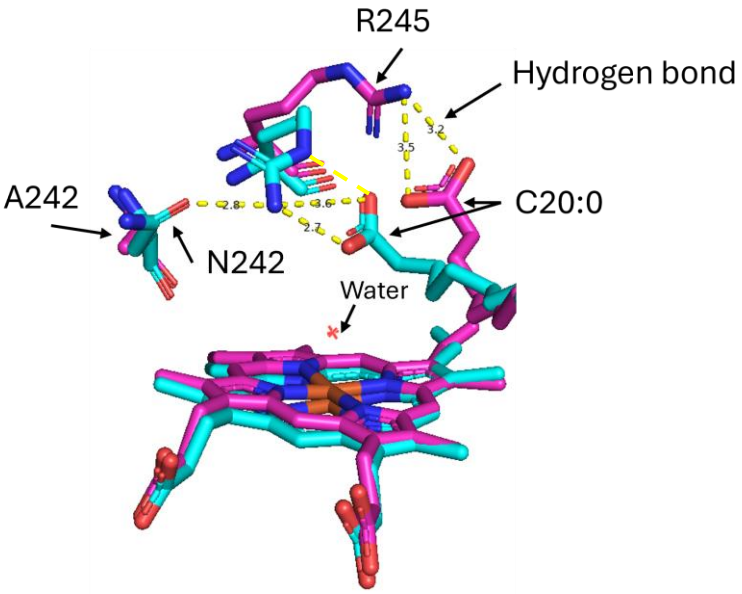

FIGURE 4.9. Conformational difference of R245 and fatty acid substrate between N242A (purple) and 4L40 (blue). The yellow dashed lines indicate hydrogen bonds and their lengths in Angstroms. For the 4L40 structure (blue), bonds between R245, the fatty acid, and N242 are of lengths 2.7, 3.6, and 2.8 Å. For the N242A structure (purple) the bonds between R245 and the fatty acid are of lengths 3.5 and 3.2 Å.

Alongside the N242A structure, a H_2O_2-soaked crystal was measured for diffraction to observe any conformational changes that occur upon addition of H_2O_2 (Fig 4.10.). Both the crystal condition and resolution of the resolved crystal structure used in Figure 4.12 can be found in Table 1. As seen in figure 4.12, no changes occur. This could be due to the soaking time of H_2O_2 not being optimal as, seen in Chapter 3, peroxide binding still occurs for this variant, as evidenced form the detection of Compound II in the stopped-flow data. Further work exploring soaking times is required.

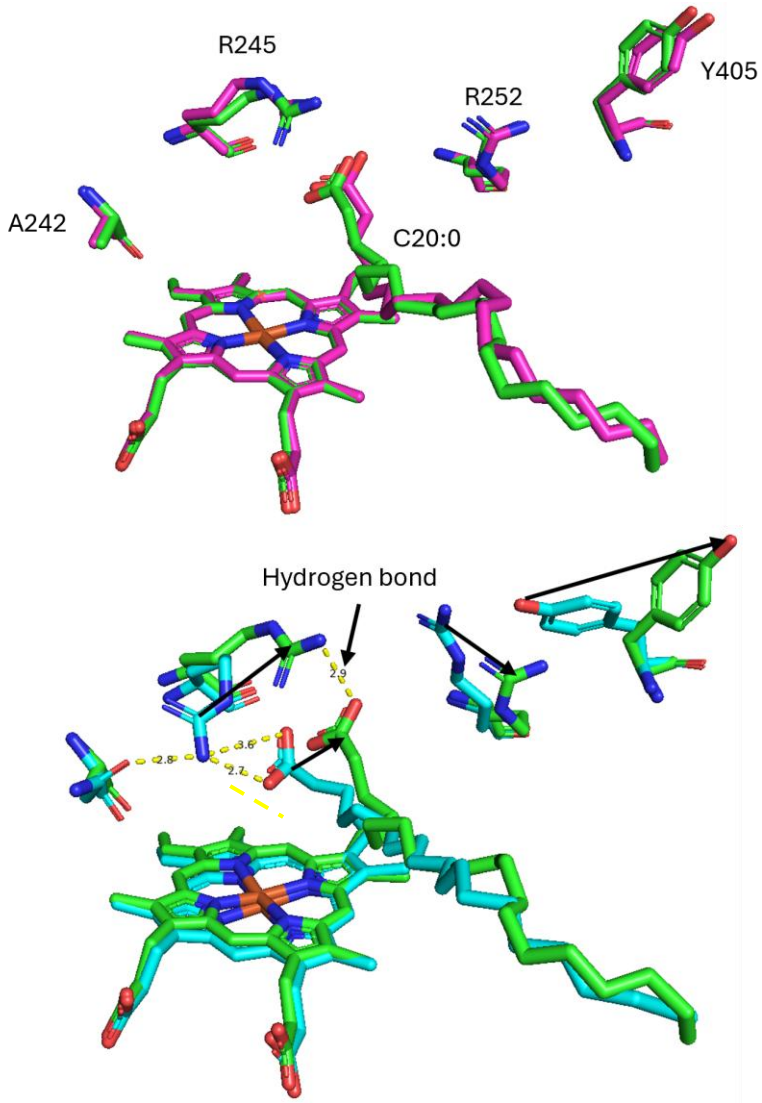

FIGURE 4.10. Hydrogen peroxide-soaked N242A structure (green) superimposed with the N242A crystal structure (top) and the 4L40 structure (blue (bottom)). The top superimposed active site shows no conformational difference between both N242A crystal structures whereas, the bottom superimposed structures show the same differences between the N242A structure and 4L40 structure seen in Figure 4.10. A single hydrogen bond interaction between R245 and C20:0 of 2.9 Å length in the N242A soak crystal structure is represented by the yellow dashed line.

X-ray crystallography of the A366P variant

X-ray diffraction experiments on the A366P variant macrocrystals encountered several complications. The crystals generally exhibited poor diffraction, and in some cases failed to diffract altogether. Although one dataset of reasonable resolution using the crystallography condition seen in Table 4.1. Issues with the statistical quality arose during data processing (Table 4.1) including poor R-work and R-free values, as well as pipelines suggesting both crystal twinning and anisotropy. Although the model employed fitted well in the molecular replacement generated electron density map, the statistical quality for the resolution of the dataset remained poor after refinement, showing no sign of improvement. Due to this, any conformational changes observed in the proceeding figures can only be taken as suggestions and not definitive. Furthermore, no suggestive conformational changes from a H_2O_2 soak were obtainable due to no diffraction from crystals.

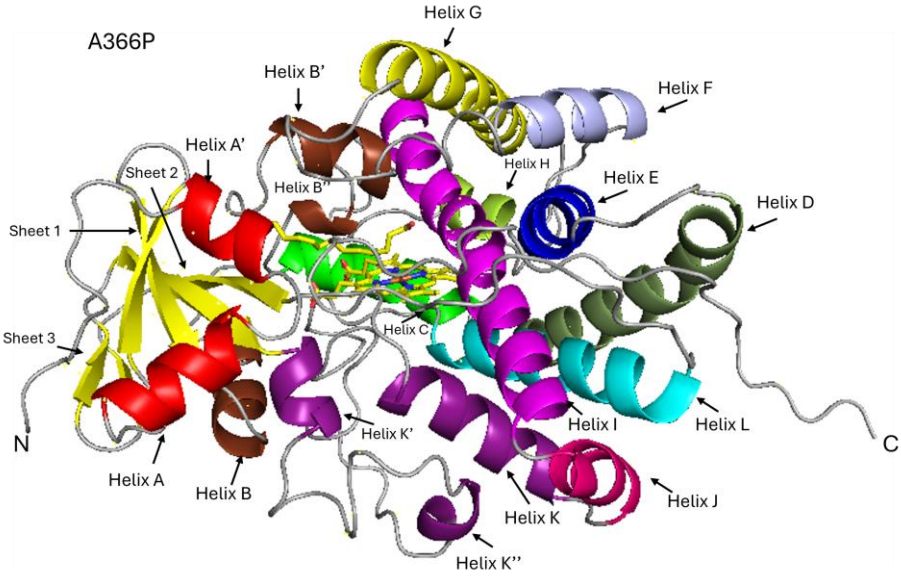

FIGURE 4.11. Cartoon crystal structure of A366P. The structure has a resolution of 1.87 Å, R-work of 0.5 and R-free of 0.54. Helices A to L, sheets 1 to 3, and both the N- and C-terminals of the A366P fold are coloured and/or labelled within the figure.

As with the N242A structure, the A366P crystal structure (Fig 4.11) adopts the canonical cytochrome P450 fold, which is predominantly α-helical, consisting of ~12 conserved helices (A–L) surrounding the heme prosthetic group. In addition to these helices, N242A also contains several short β-sheets that stabilise the core structure. The central features of the fold include

the long I-helix traversing the active site and the L-helix cysteine loop, which coordinates the heme iron via the axial cysteine ligand (Bharadwaj, V. et al., 2018).

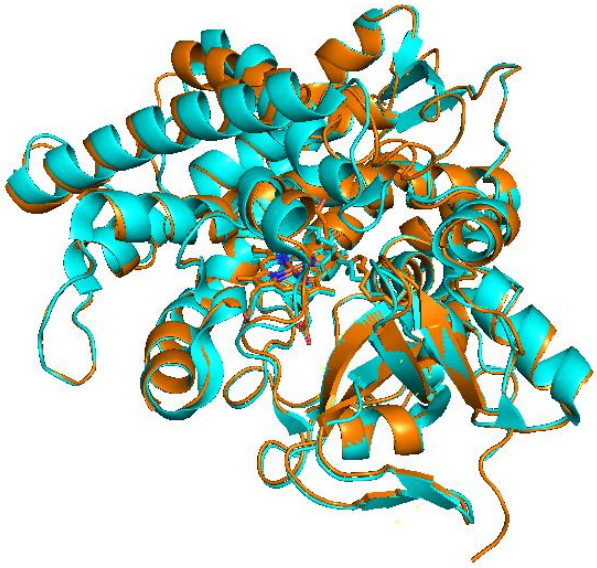

FIGURE 4.12. Superimposed structures of A366P fatty acid bound and the 4L40 PDB file. As in the previously shown superimpositions, the same only minor secondary-structure differences are observed between monomers. Specifically, the flexible loop between helices F and G.

As with the N242A structure (Fig 4.6), the flexible region of A366P found between helices F and G known as the F/G loop shows similar significant deviations between structures. The difference between A366P and the WT structure is not represented here as the difference is similar to what is seen between N242A and WT.

Examination of the A366P $2F_o$-F_c electron density map revealed that the crystal structure carried the desired mutation (Fig 4.13). Furthermore, the $2F_o$-F_c was consistent with the presence of a fatty acid chain and the presence of a water molecule above the heme (Fig 4.14). The same conclusion made from Figure 4.7 regarding the presence of water alongside a fatty acid can be corroborated here. Furthermore, the presence of proline has been proven spectroscopically in Chapter 3. The mutation was designed to remove a hydrogen bond interaction to the cysteine. From the Fe(II)-CO spectra in Chapter 3, a greater thiolate character is observed.

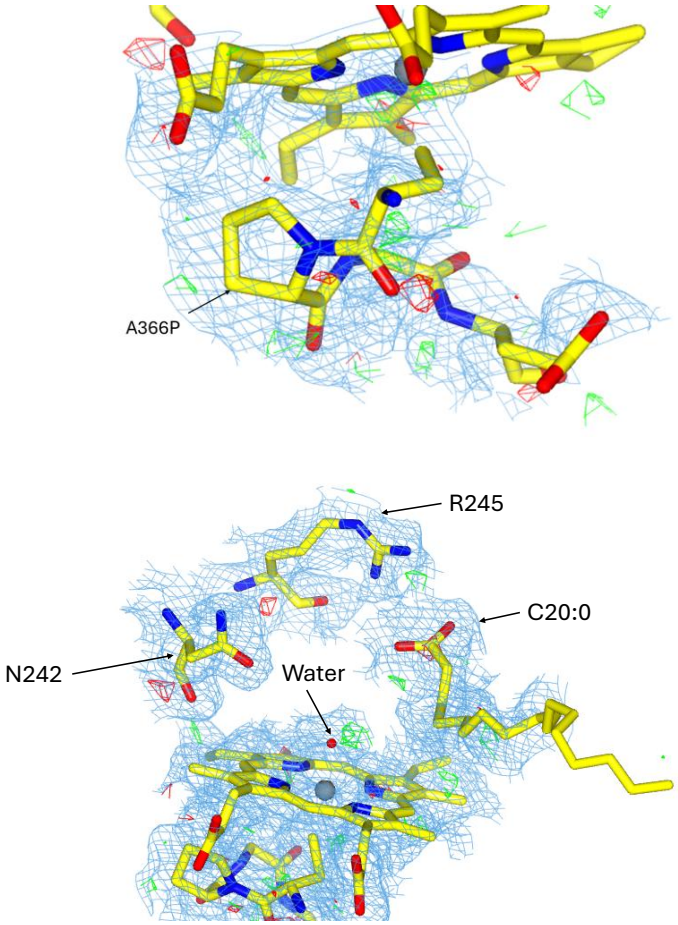

FIGURE 4.13. F_o-F_c and $2F_o$-F_c electron density of the proximal side (top) and axial side (bottom) of the A366P crystal structure. The proximal side electron density (top) illustrates the electron density that corresponds to the presence of P366. The Axial side electron density (bottom) represents the presence of an axial water molecule that coordinates to the heme, as well as the position of the fatty acid coordinating residues R245 and N242.

Figure 4.13 also shows the $2F_o$-F_c electron density on the axial side of the A366P heme. An apparent difference when compared to WT is the reorientation of residue N242 and 'swinging out' of R245, similar to what is seen for the N242A structure. This electron density in Figure 4.13 can suggest that the proline substitution introduces backbone rigidity (due to φ angle restriction when compared to alanine) resulting in backbone shifts as far down as to position N242.

After superimposing the A366P and 4L40 PBD crystal structures, examination of active site residues revealed that R245, R252, and Y405, as well as the position of the fatty acid substrate had adopted different conformations to what is seen from the published 4L40 structure in Figure 4.1 (Fig 4.14).

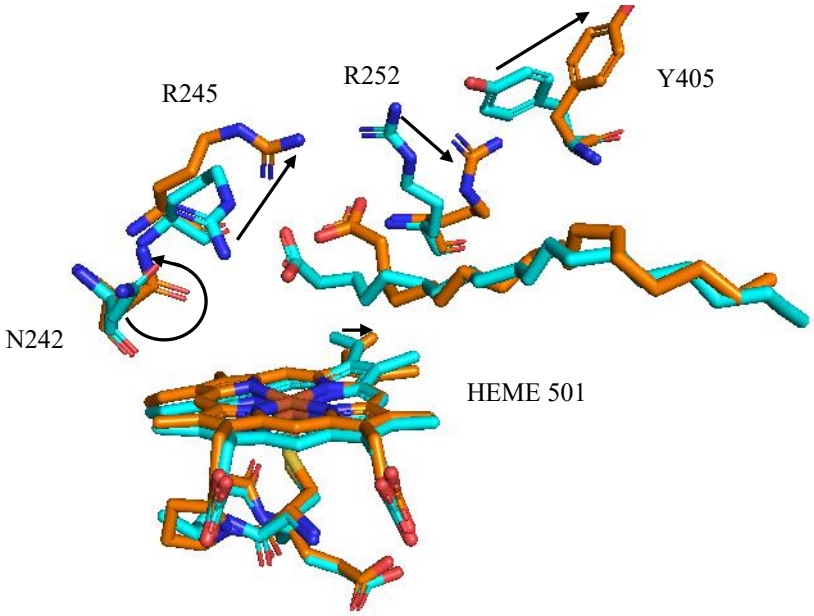

FIGURE 4.14. FIGURE 4.10. Active site residue differences between the A366P structure (orange) and the 4L40 structure (blue). Conformational changes are indicated by black arrows.

Figure 4.14 again illustrates the distal side of the A366P heme. An apparent difference when compared to WT is the reorientation of residue N242 and 'swinging out' of R245, similar to what is seen for the N242A structure.

4.4 Discussion

To aid comparison with the published $OleT_{JE}$ WT structure co-crystallized with C20:0 fatty acid (PDB: 4L40), we modelled C20:0 into the $2F_o$-F_c density of each dataset in this study. Although GC-MS analysis of our variants did not successfully identify the co-purified fatty acid, and despite the fact that C20:0 is not typically produced by *E. coli*, the C20:0 model fitted well into the observed density and therefore served as a consistent reference ligand across all structures.

The X-ray crystallographic analysis of $OleT_{JE}$ variants has provided atomic-level insights into how specific substitutions perturb the enzyme's active-site architecture and conformational dynamics. These results build directly on the spectroscopic, thermodynamic, and kinetic characterisation presented in Chapter 3, enabling a more complete understanding of the structure-function relationship.

It should be noted that in cytochrome P450 enzymes, proton delivery to the heme-bound oxygen species is typically mediated by a conserved acid–alcohol pair located on the I-helix (e.g. Asp/Thr in P450cam), which facilitates formation of the reactive Compound I intermediate. In engineered systems, mutation of this motif—most notably the T252E substitution—has been widely used to introduce a glutamate residue that can act as a proton donor and promote hydrogen peroxide-dependent "peroxygenase" activity. This modification is thought to alter the proton relay network and stabilize peroxide-derived intermediates, thereby favouring the peroxide shunt pathway over the canonical monooxygenase cycle (Podgorski, M.N., et al., 2023)

However, naturally occurring P450 peroxygenases such as $OleT_{JE}$ do not necessarily follow this paradigm. $OleT_{JE}$ catalyses oxidative decarboxylation of fatty acids using H_2O_2 without requiring the canonical engineered glutamate residue (Belcher *et al.*, 2014). Instead, its

peroxygenase activity is associated with alternative active-site features, most notably the conserved arginine (Arg245) that anchors the substrate and is proposed to participate in acid–base chemistry during addition of hydrogen peroxide (Belcher *et al.*, 2014). These observations suggest that while introduction of a glutamate residue can promote peroxygenase activity in engineered P450s, it is not a universal requirement.

N242A

For the N242A variant, the refined structure revealed that the loss of the hydrogen bond between N242 and R245 results in a significant conformational shift of R245 and the fatty acid substrate. Rather than stabilising the productive geometry seen in the WT enzyme, the substrate and surrounding residues (including R245, R252, and Y405) adopt altered conformations. This helps to rationalise the differed spectroscopic, kinetic and thermodynamic values compared to the WT, obtained in the previous chapter. The residue conformation shifts coincide with the position of the fatty acid and, therefore affecting its ability to fully occupy the active site (seen from titrations), slow the decay of catalytically important transient intermediates, and affecting H_2O_2 binding (stopped-flow). Furthermore, the presence of a water molecule above the heme centre in the substrate-bound structure is particularly striking, as it suggests incomplete displacement of the water ligand during substrate binding. Such a state is inconsistent with the canonical P450 mechanism and may indicate a unique water high-spin intermediate (Matthews, S. et al 2017).

A366P

The A366P variant posed more challenges, as diffraction data were of poor statistical quality, as seen by the F_o-F_c and 2 F_o-F_c density maps. Nevertheless, the preliminary model suggests that proline substitution at position 366 disrupts proximal-side chain hydrogen bonding with the cysteine ligand. As a result, the Fe(II)-CO spectra of A366P, shown in Figures 3.3 and 3.4

in the previous chapter, indicates a higher molar extinction at 450 nm compared to the WT. This distinct difference suggests that the axial cysteine thiolate character is more pronounced in the A366P variant, consistent with the loss of a stabilising hydrogen bond and corroborated by the substitution of alanine for proline within the A366P structure. This evidence is supported by a previously published study on the A369P mutation in $OleT_{SA}$ (Amaya, J.A., 2018) which indicated the same higher molar extinction of the deprotonated thiolate character as well as a tendency to exist predominantly in the high spin state.

The proposed conformational perturbations of A366P appear to mirror, at least partially, those seen in N242A, due to the N242 residue being reoriented. Although these observations cannot be considered definitive due to dataset limitations, they nonetheless provide a plausible explanation for the high spin spectroscopic differences observed in the as purified N242A variant but not in A366P variant as seen in Chapter 3 and in the $OleT_{SA}$ A369P variant (Amaya, J.A., 2018). Compared to N242A, A366P exhibited lower K_d values, a stronger tendency toward the high-spin state, and fewer complications with fatty acid substrates seen in Chapter 3.

4.5 Conclusion

This chapter highlights the value of X-ray crystallography in clarifying how specific substitutions perturb $OleT_{JE}$ structure and function. For the N242A variant, the structure provided direct evidence that loss of the N242–R245 hydrogen bond displaces R245 and the fatty acid substrate, helping to provide rationale for the observed changes in Chapter 3 when compared to WT. The unusual persistence of a water molecule above the heme centre further suggests that substrate binding does not fully displace the aqua ligand, raising the possibility of an unconventional aqua high-spin intermediate.

For the A366P variant, although diffraction data were of lower quality, the structural model together with spectroscopic data indicates that substitution of alanine for proline disrupts proximal-side hydrogen bonding to the cysteine thiolate. This disruption enhances thiolate character of the axial cysteine, consistent with the stronger Fe(II)-CO absorption at 450 nm observed in Chapter 3. These findings suggest that A366P alters the balance of thiol–thiolate interactions in the heme centre and directly alters the spin state equilibrium, favouring the high-spin state. This Chapter helps to offer a structural rationale for its spectroscopic differences.

Chapter 5

Conclusions and Outlook

Throughout this thesis, a comprehensive investigation of experimental data has been conducted to elucidate the observed functional differences between WT $OleT_{JE}$ and the variants A366P, Q354A, and N242A. Detailed fatty acid binding titrations revealed variant-specific alterations in substrate affinity, as evidenced by shifts in dissociation constants. Stopped-flow UV/Vis spectrophotometry further demonstrated a pronounced reduction in the Compound I decay rate in select variants, suggesting enhanced stabilisation of this highly reactive intermediate. High-resolution macromolecular crystallography provided critical structural insights, revealing modifications to the active site architecture that likely underpin the observed changes in both substrate binding and kinetics.

These findings collectively highlight the relationship between protein structure and function and underscore the capacity of rational protein engineering to modulate enzymatic activity. Nevertheless, while these studies provide initial evidence, further experiments are warranted to fully characterise the mechanistic consequences of these mutations. Future investigations will leverage electron paramagnetic resonance (EPR) spectroscopy to probe alterations in the heme iron spin state equilibrium, offering a more nuanced understanding of how these mutations influence the electronic environment of the active site. Complementary gas chromatography–mass spectrometry (GC-MS) analyses will be employed to confirm product formation and quantify residual fatty acids post-purification, providing a direct link between structural modifications and catalytic outcomes.

Looking forward, these insights not only enhance our understanding of $OleT_{JE}$ catalysis but also provide a framework for the rational design of tailored biocatalysts. By stabilising reactive

intermediates and fine-tuning substrate specificity, engineered variants of $OleT_{JE}$ may serve as powerful tools for sustainable biotechnological applications, including selective hydrocarbon production and fatty acid derivatisation. In a broader context, this work exemplifies how integrating structural, kinetic, and mechanistic studies can inform targeted enzyme optimisation, bridging the gap between fundamental biochemical research and applied biocatalysis. Ultimately, this thesis establishes a foundation for future studies aimed at exploiting the full catalytic potential of P450 enzymes through precise and rational protein engineering strategies.

Appendix

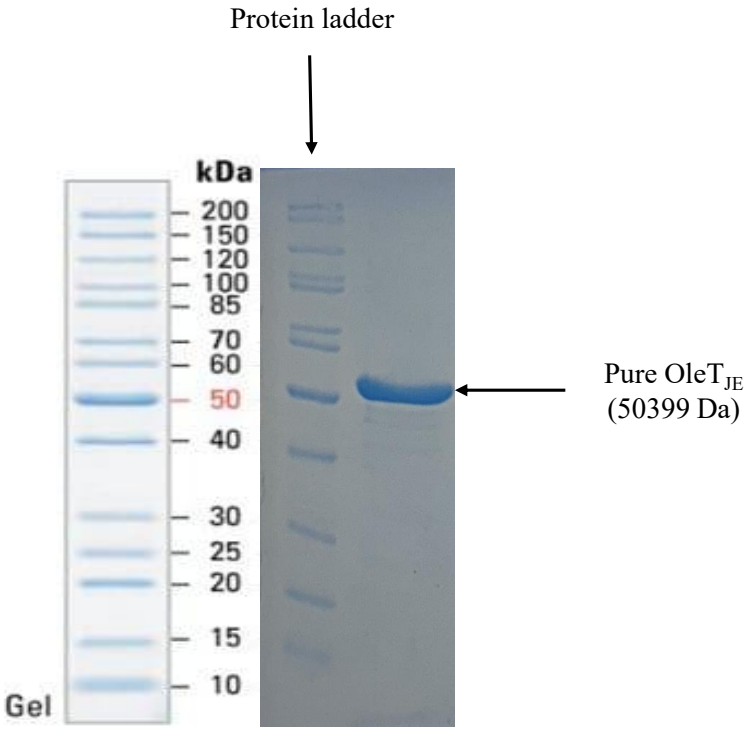

Figure 1. SDS-PAGE analysis of S200 purified OleT$_{JE}$

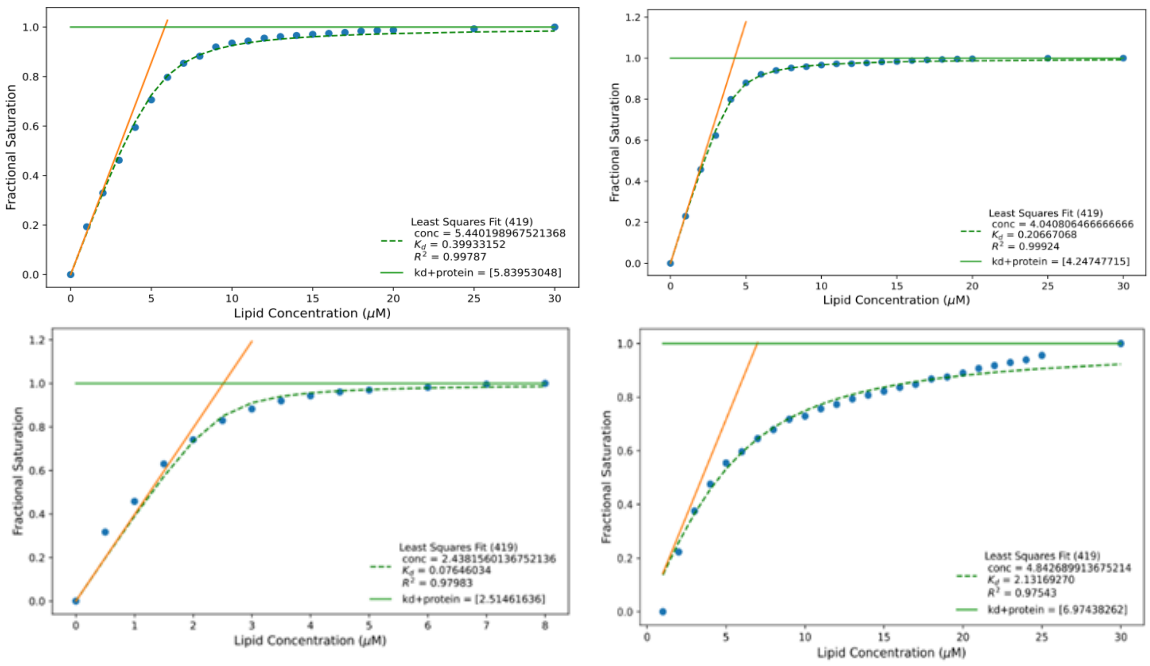

FIGURE 2. C20:0 Fatty acid fractional saturation binding isotherms with fits and stoichiometry of binding indicated. WT OleT$_{JE}$ (top left) and variants A366P (top right), Q354A (bottom left), and N242A (bottom right) using C20:0 fatty acid dissolved in 70% ethanol and 30% Triton X100 detergent.

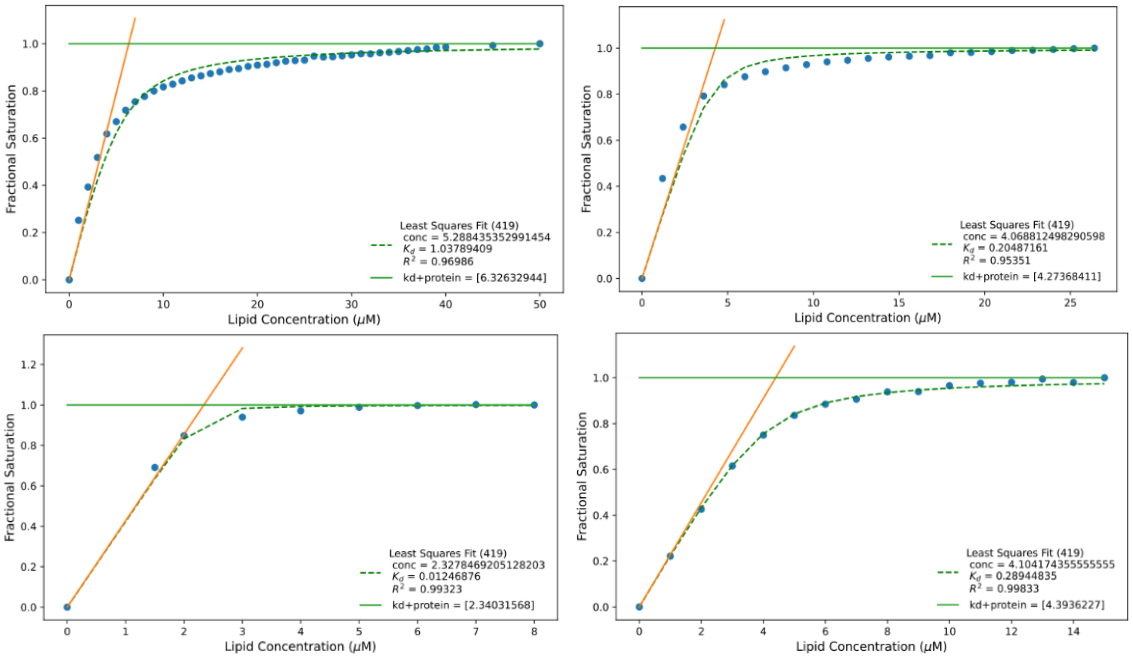

FIGURE 3. C18:0 Fatty acid fractional saturation binding isotherms with fits and stoichiometry of binding indicated. WT $OleT_{JE}$ (top left) and variants A366P (top right), Q354A (bottom left), and N242A (bottom right). The C18:0 fatty acid was dissolved in 70% ethanol and 30% Triton X100 detergent but in 100% ethanol for N242A.

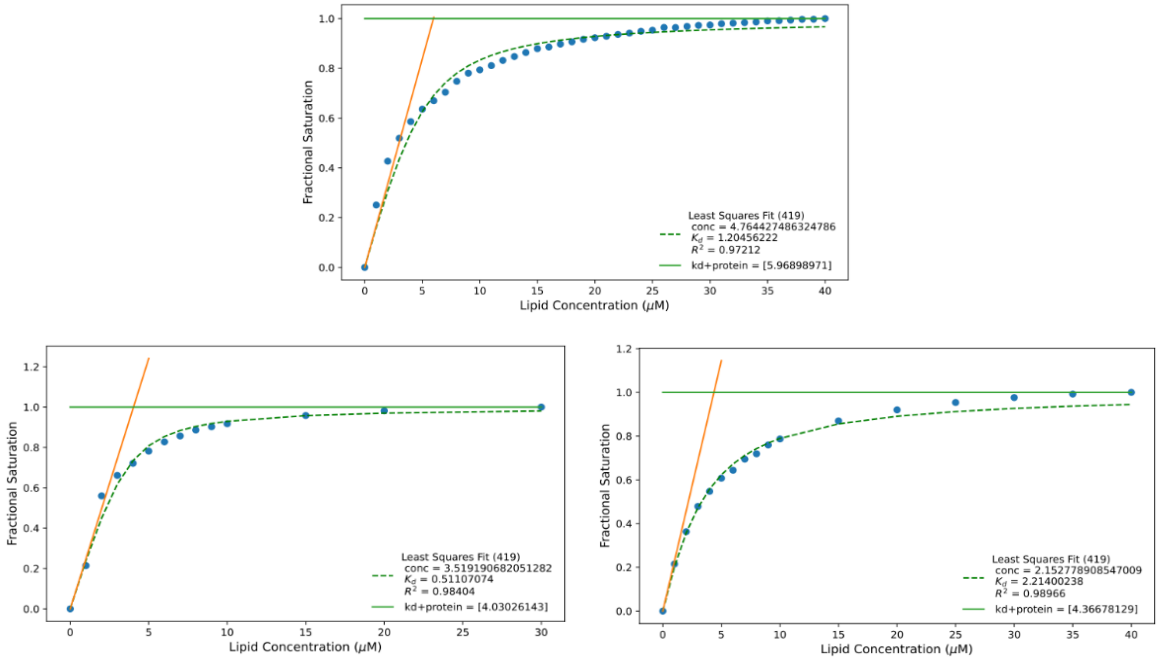

FIGURE 4. C12:0 Fatty acid fractional saturation binding isotherms with fits and stoichiometry of binding indicated. WT $OleT_{JE}$ (top) and variants A366P (bottom left), Q354A (bottom right). The C12:0 fatty acid was dissolved in 100% ethanol.

References

- Manikandan, P. and Nagini, S., 2018. Cytochrome P450 structure, function, and clinical significance: a review. *Current drug targets*, *19*(1), pp.38-54.
- Cupp-Vickery, J.R. and Poulos, T.L., 1997. Structure of cytochrome P450eryF: substrate, inhibitors, and model compounds bound in the active site. *Steroids*, *62*(1), pp.112-116.
- Ghosh, D., Griswold, J., Erman, M. and Pangborn, W., 2009. Structural basis for androgen specificity and oestrogen synthesis in human aromatase. *Nature*, *457*(7226), pp.219-223.
- McDonnell, A.M. and Dang, C.H., 2013. Basic review of the cytochrome p450 system. *Journal of the advanced practitioner in oncology*, *4*(4), p.263.
- Gibson, G.G. and Skett, P., 2013. Introduction to drug metabolism. Springer.
- Munro, A.W., Girvan, H.M. and McLean, K.J., 2007. Cytochrome P450–redox partner fusion enzymes. *Biochimica et Biophysica Acta (BBA)-General Subjects*, *1770*(3), pp.345-359.
- Denisov, I.G., Makris, T.M., Sligar, S.G. and Schlichting, I., 2005. Structure and chemistry of cytochrome P450. *Chemical reviews*, *105*(6), pp.2253-2278.
- Guengerich, F.P. and Munro, A.W., 2013. Unusual cytochrome P450 enzymes and reactions. *Journal of Biological Chemistry*, *288*(24), pp.17065-17073.
- Belcher, J., McLean, K.J., Matthews, S., Woodward, L.S., Fisher, K., Rigby, S.E., Nelson, D.R., Potts, D., Baynham, M.T., Parker, D.A. and Leys, D., 2014. Structure and biochemical properties of the alkene producing cytochrome P450 OleTJE (CYP152L1) from the Jeotgalicoccus sp. 8456 bacterium. *Journal of Biological Chemistry*, *289*(10), pp.6535-6550
- Sligar, S.G., 2010. Glimpsing the critical intermediate in cytochrome P450 oxidations. *Science*, *330*(6006), pp.924-925.
- Rittle, J. and Green, M.T., 2010. Cytochrome P450 compound I: capture, characterization, and CH bond activation kinetics. *Science*, *330*(6006), pp.933-937.
- Wang, M., Roberts, D.L., Paschke, R., Shea, T.M., Masters, B.S.S. and Kim, J.J.P., 1997. Three-dimensional structure of NADPH–cytochrome P450 reductase: prototype for FMN-and FAD-containing enzymes. *Proceedings of the National Academy of Sciences*, *94*(16), pp.8411-8416.
- Lee, D.S., Yamada, A., Sugimoto, H., Matsunaga, I., Ogura, H., Ichihara, K., Adachi, S.I., Park, S.Y. and Shiro, Y., 2003. Substrate recognition and molecular mechanism of fatty acid hydroxylation by

cytochrome P450 from Bacillus subtilis: crystallographic, spectroscopic, and mutational studies. *Journal of Biological Chemistry*, *278*(11), pp.9761-9767.

- Munro, A.W., McLean, K.J., Grant, J.L. and Makris, T.M., 2018. Structure and function of the cytochrome P450 peroxygenase enzymes. *Biochemical Society Transactions*, *46*(1), pp.183-196.
- Amaya, J.A., Rutland, C.D., Leschinsky, N. and Makris, T.M., 2018. A distal loop controls product release and chemo-and regioselectivity in cytochrome P450 decarboxylases. *Biochemistry*, *57*(3), pp.344-353.
- Matthews, S., Tee, K.L., Rattray, N.J., McLean, K.J., Leys, D., Parker, D.A., Blankley, R.T. and Munro, A.W., 2017. Production of alkenes and novel secondary products by P450 Ole TJE using novel H2O2-generating fusion protein systems. *FEBS letters*, *591*(5), pp.737-750.
- Rude, M.A., Baron, T.S., Brubaker, S., Alibhai, M., Del Cardayre, S.B. and Schirmer, A., 2011. Terminal olefin (1-alkene) biosynthesis by a novel P450 fatty acid decarboxylase from Jeotgalicoccus species. *Applied and environmental microbiology*, *77*(5), pp.1718-1727.
- Jiang, Y., Peng, W., Li, Z., You, C., Zhao, Y., Tang, D., Wang, B. and Li, S., 2021. Unexpected reactions of α, β-unsaturated fatty acids provide insight into the mechanisms of CYP152 peroxygenases. *Angewandte Chemie International Edition*, *60*(46), pp.24694-24701.
- Wang, W. and Lu, X., 2013. Microbial synthesis of alka (e) nes. *Frontiers in bioengineering and biotechnology*, *1*, p.10.
- Taylor, T.A. and Unakal, C.G., 2017. Staphylococcus aureus infection.
- Jiang, Y., Li, Z., Wang, C., Zhou, Y.J., Xu, H. and Li, S., 2019. Biochemical characterization of three new α-olefin-producing P450 fatty acid decarboxylases with a halophilic property. *Biotechnology for biofuels*, *12*, pp.1-14.
- Fang, B., Xu, H., Liu, Y., Qi, F., Zhang, W., Chen, H., Wang, C., Wang, Y., Yang, W. and Li, S., 2017. Mutagenesis and redox partners analysis of the P450 fatty acid decarboxylase OleTJE. *Scientific Reports*, *7*(1), p.44258.
- Amaya, J.A., 2018. *Mechanisms of Decarboxylation in the CYP152 Family of Cytochrome P450s* (Doctoral dissertation, University of South Carolina)
- Arachidic acid, National Center for Biotechnology Information. PubChem Compound Database. Available at: https://pubchem.ncbi.nlm.nih.gov/compound/Arachidic-Acid (Accessed: 26 March 2024).

- Dumon-Seignovert, L., Cariot, G. and Vuillard, L., 2004. The toxicity of recombinant proteins in Escherichia coli: a comparison of overexpression in BL21 (DE3), C41 (DE3), and C43 (DE3). *Protein expression and purification*, *37*(1), pp.203-206.
- Grant, J.L., Hsieh, C.H. & Makris, T.M. 2015 'Decarboxylation of fatty acids to terminal alkenes by cytochrome P450 compound I', *Journal of the American Chemical Society*, 137(15), pp. 4940–4943.
- Green, M.T. 1998 'Role of the axial ligand in determining the spin state of resting cytochrome P450', *Journal of the American Chemical Society*, 120(41), pp. 10772–10773.
- Pochapsky, T.C. 2020 'A dynamic understanding of cytochrome P450 structure and function: Insights from NMR spectroscopy', *Nature Communications*, 11(1), p. 8215082.
- Suzuki, H., Inabe, K., Shirakawa, Y., Umezawa, N., Kato, N., Higuchi, T. 2017 'Role of thiolate ligand in spin state and redox switching in iron(III) complexes', *Inorganic Chemistry*, 56(2), pp. 1051–1059.
- Gable, J.A., Tripathi, S., Poulos, T.L. 2022 Structural insights on the conversion of cytochrome P450 to P420. *ACS Omega*, 7(15), pp. 13213–13222.
- Sun, Y., Zeng, W., Benabbas, A., Ye, X., Denisov, I.G., Sligar, S.G., Du, J., Dawson, J.H. and Champion, P.M., 2013. Investigations of heme ligation and ligand switching in cytochromes P450 and P420. *Biochemistry*, 52(34), pp. 5941–5951.
- Perera, R., Kincaid, J.R., and others, 2003. Neutral thiol as a proximal ligand to ferrous heme iron. *Proceedings of the National Academy of Sciences of the United States of America*, 100(26), pp. 14719–14724.
- Zhong, F., Zhang, Y., and others, 2014. Redox-dependent stability, protonation, and reactivity of cytochrome P450cam. *Proceedings of the National Academy of Sciences of the United States of America*, 111(3), pp. E306–E315.
- Lučić, M., Chaplin, A. K., Moreno-Chicano, T., Dworkowski, F. S. N., Wilson, M. T., Svistunenko, D. A., Hough, M. A. & Worrall, J. A. R. (2020) 'A subtle structural change in the distal haem pocket has a remarkable effect on tuning hydrogen peroxide reactivity in dye decolourising peroxidases from *Streptomyces lividans*', *Dalton Transactions*, 49, pp. 1620-1636. DOI: 10.1039/C9DT04583J.
- Xie, G., Arakawa, T., Timasheff, S. N., & Tsuruta, H. (1997) 'Mechanism of the stabilization of ribonuclease A by sorbitol', *Biophysical Chemistry*, 64(1–3), pp. 71-81. doi:10.1016/S0301-4622(97)83547-5.

- Matthews, S., Tee, K. L., Rattray, N. J., McLean, K. J., Leys, D., Parker, D. A., Blankley, R. T. & Munro, A. W. (2017) 'Production of alkenes and novel secondary products by P450 OleTJE using novel H_2O_2-generating fusion protein systems', *FEBS Letters*, 591(5), pp. 737-750. doi: 10.1002/1873-3468.12581.
- Hsieh, C.-H., Shanklin, J. & Stevens, R. C. (2017) 'The enigmatic P450 decarboxylase OleT is capable of both hydroxylation and decarboxylation of fatty acids', *Scientific Reports*, 7, 15598. doi: 10.1038/s41598-017-15874-5.
- Girvan, H. M., Poddar, H., McLean, K. J., Nelson, D. R., & Leys, D. (2018) 'Structural and catalytic properties of the peroxygenase CYP152 family', *Journal of Biological Chemistry*, 293(46), pp. 17600-17614. doi:10.1074/jbc.ra119.011630.
- Linares, J., Orellana, G., Clérac, R., Galán-Mascarós, J. R. & Roubeau, O. (2012) 'Pressure and temperature spin-crossover sensors with molecular and nanoscale materials: a review', *Sensors and Actuators A: Physical*, 188, pp. 10-28. doi:10.1016/j.sna.2012.04.018.
- Yoshioka, S., Tosha, T., Takahashi, S., Ishimori, K., Hori, H., & Morishima, I. (2002) 'Roles of the proximal hydrogen bonding network in cytochrome P450cam-catalyzed oxygenation', *Journal of the American Chemical Society*, 124(49), pp. 14571–14579. doi:10.1021/ja0265409.
- Gildea RJ, Beilsten-Edmands J, Axford D, Horrell S, Aller P, Sandy J, Sanchez-Weatherby J, Owen CD, Lukacik P, Strain-Damerell C, Owen RL, Walsh MA, Winter G. *xia2.multiplex: a multi-crystal data-analysis pipeline*. *Acta Crystallographica Section D Structural Biology*. 2022;78(Pt 6):752-769. doi:10.1107/S2059798322004399
- Potterton L, Agirre J, Ballard C, Cowtan K, Dodson E, Evans PR, Jenkins H, Keegan R, Krissinel E, Stevenson K, et al. *CCP4i2: the new graphical user interface to the CCP4 programme suite.* Journal of Applied Crystallography. 2018;51:1511-1518. doi:10.1107/S1600576718005115.
- Evans PR, Murshudov GN. *How good are my data and what is the resolution?* Acta Crystallographica Section D Biological Crystallography. 2013;69(Pt 7):1204-14. https://doi.org/10.1107/S0907444913000061 PMID:23793146 PMCID:PMC3689523.
- Lebedev AA, Vagin AA, Murshudov GN. *Model preparation in MOLREP and examples of model improvement using X-ray data.* Acta Crystallographica Section D: Biological Crystallography. 2008;64(Pt 1):33-39. doi:10.1107/S0907444907049839. PMCID: PMC2394799

- Leys D, Belcher J, McLean KJ, Matthews S, Woodward LS, Fisher K, Rigby SE, Nelson DR, Potts D, Baynham MT, Parker DA, Munro AW. 2013. *Structure of the P450 OleT with a C20 fatty acid substrate bound*. PDB entry 4L40. DOI: 10.2210/pdb4L40/pdb.
- Kovalevskiy, O., Nicholls, R.A., Long, F., Carlon, A., Fischberg, M., Schulz, E., Richardson, J.S., Richardson, D.C. & Murshudov, G.N. **2018.** *Overview of refinement procedures within REFMAC5*. *Acta Crystallographica Section D Biological Crystallography.* **74**(Part 1):100-110. DOI:10.1107/S2059798317016034.
- Emsley, P. **(Year unknown).** *The Coot User Manual.* MRC Laboratory of Molecular Biology. [PDF]
- Bharadwaj, V. S., Kim, S., Guarnieri, M. T. & Crowley, M. F. **2018.** *Different Behaviors of a Substrate in P450 Decarboxylase and Hydroxylase Reveal Reactivity-Enabling Actors*. *Scientific Reports*, 8, Article number: 12826. doi:10.1038/s41598-018-31237-4
- Conner, K.P., Schimpf, A.M., Cruce, A.A., McLean, K.J., Munro, A.W., Frank, D.J., Krzyaniak, M.D., Ortiz de Montellano, P., Bowman, M.K. and Atkins, W.M., 2014. Strength of axial water ligation in substrate-free cytochrome P450s is isoform dependent. *Biochemistry*, 53(9), pp.1428–1434.
- Groves, J.T., Haushalter, R.C., Nakamura, M., Nemo, T.E. & Evans, B.J., 1981. High-valent iron-porphyrin complexes related to peroxidase and cytochrome P-450. Journal of the American Chemical Society, 103(10), pp.2884–2886.
- Pan, Z. et al., 2006–2009. Kinetic studies of reactions of iron(IV)-oxo porphyrin radical cations with organic reductants. Journal of the American Chemical Society (and related works).
- Newcomb, M. et al., 2006. Cytochrome P450 Compound I: Capture, characterization and C–H bond activation kinetics. Journal of the American Chemical Society.
- Garcia-Bosch, I., Sharma, S. K. & Karlin, K. D., 2013. A selective stepwise heme oxygenase model system: an iron(IV)-oxo porphyrin π-cation radical leads to a verdoheme-type compound via an isoporphyrin intermediate. Journal of the American Chemical Society, 135(44), pp.16248-16251.
- Jung, C., de Vries, S. & Schünemann, V., 2011. Spectroscopic characterization of cytochrome P450 compound I. Archives of Biochemistry and Biophysics, 507(1), pp.44-55
- Hohenberger, J., Ray, K. & Meyer, K., 2012. The biology and chemistry of high-valent iron–oxo and iron–nitride complexes. Nature Communications, 3, 720.

- Grant, J. L., Mitchell, M. E. & Makris, T. M., 2016. Catalytic strategy for carbon–carbon bond scission by the cytochrome P450 OleT. *Proceedings of the National Academy of Sciences of the United States of America*, 113(36), pp.10049-10054.
- Larionov, S.V., 2008. Spin Transition in Iron(III) and Iron(II) Complexes. Russian Journal of Coordination Chemistry, 34(4), pp.237-250. DOI: 10.1134/S1070328408040015.
- Bethe, H., 1929. Termaufspaltung in Kristallen. *Annalen der Physik*, 395(1), pp.133-208.
- Podgorski, M.N., Lee, J.H.Z., Harbort, J.S., Nguyen, G.T.H., Doherty, D.Z., Donald, W.A., Harmer, J.R., Bruning, J.B. and Bell, S.G. (2023) 'Characterisation of the heme aqua-ligand coordination environment in an engineered peroxygenase cytochrome P450 variant', *Trends in Biotechnology*.